Summer 8-31-2011

The effects of periodic and non-periodic inputs on the dynamics of a medial entorhinal cortex layer II stellate cell model

Dongwook Kim
New Jersey Institute of Technology

ABSTRACT

THE EFFECTS OF PERIODIC AND NON-PERIODIC INPUTS ON THE DYNAMICS OF A MEDIAL ENTORHINAL CORTEX LAYER II STELLATE CELL MODEL

by
Dongwook Kim

Various neuron types exhibit sub-threshold and firing frequency resonance in which the sub-threshold membrane potential or firing frequency responses to periodic inputs peak at a preferred frequency (or frequencies). Previous experimental work has shown that medial entorhinal cortex layer II stellate cells (SCs) exhibit sub-threshold and firing frequency resonance in the theta frequency band (4 - 10 Hz). In this thesis we seek to understand the biophysical and dynamic mechanism underlying these phenomena and how they are related. We studied the effects of sinusoidal current and synaptic conductance inputs at various frequencies, with and without noise, on the supra-threshold dynamics of a SC model. For current inputs, our results show that while the SC model exhibits a single frequency preference peak (in the theta frequency band) for low sinusoidal input levels, it exhibits three preferred frequency peaks for larger input levels. These additional peaks occur at frequencies that are roughly a multiple of the "theta" one. For synaptic conductance inputs, we observe an additional peak in the signal gain which occurs at a much higher frequency (in the high gamma frequency band). These findings depart from the linear prediction. The corresponding linearized model does not exhibit three preferred frequency peaks for current inputs and a much higher frequency for conductance inputs under the same conditions (such as parameters, noise, amplitude of inputs and maximal synaptic conductance) in the nonlinear model.

Previous experimental work has shown high-frequency Poisson-distributed trains of combined excitatory and inhibitory conductance- and current-based synaptic inputs reduce amplitude of subthreshold oscillations of SCs. The second goal of this thesis is to investigate the mechanism underlying these phenomena in the context of the model. More specially, we studied the effects of both conductance- and current-based synaptic inputs at various maximal conductance values on a SC model. Our numerical simulations show that conductance-based synaptic inputs reduce the amplitude of SC's subthreshold oscillations for low enough value of the maximal synaptic conductance value but amplify these oscillations at a higher range. These results are in contrast to the experimental results.

THE EFFECTS OF PERIODIC AND NON-PERIODIC INPUTS ON THE DYNAMICS OF A MEDIAL ENTORHINAL CORTEX LAYER II STELLATE CELL MODEL

by
Dongwook Kim

A Dissertation
Submitted to the Faculty of
New Jersey Institute of Technology
in Partial Fulfillment of the Requirements for the Degree of
Doctor of Philosophy in Mathematical Sciences

Department of Mathematical Sciences

June 2011

APPROVAL PAGE

THE EFFECTS OF PERIODIC AND NON-PERIODIC INPUTS ON THE DYNAMICS OF A MEDIAL ENTORHINAL CORTEX LAYER II STELLATE CELL MODEL

Dongwook Kim

Horacio G. Rotstein, Dissertation Advisor — Date
Assistant Professor, Department of Mathematical Sciences, NJIT

Farzan Nadim, Committee Member — Date
Professor, Department of Mathematical Sciences, NJIT

Jorge Golowasch, Committee Member — Date
Associate Professor, Department of Mathematical Sciences, NJIT

Victor V. Matveev, Committee Member — Date
Associate Professor, Department of Mathematical Sciences, NJIT

Vijayalakshmi Santhakumar, Committee Member — Date
Assistant Professor, Department of Neurology and Neuroscience, UMDNJ

BIOGRAPHICAL SKETCH

Author: Dongwook Kim

Degree: Doctor of Philosophy

Date: June 2011

Undergraduate and Graduate Education:

- Doctor of Philosophy in Mathematical Sciences,
  New Jersey Institute of Technology, Newark, NJ, 2011
- Master of Science in Mathematics,
  University of Georgia, Athens, GA, 2006
- Bachelor of Science in Mathematics,
  Chung-Ang University, Seoul, Korea, 2003

Major: Applied mathematics

Presentations and Publications:

Dongwook Kim, "Firing rate (super-threshold) frequency preferences in a persistent sodium / h-current medial entorhinal cortex layer II stellate cell model," *Applied Math Days*, Rensselaer Polytechnic Institute, April 8-9th, 2011.

Dongwook Kim, "The effect of current and conductance inputs on firing rate resonance in a stellate cell model," *The Dana Knox Student Research Showcase*, New Jersey Institute of Technology, April 6, 2011.

Dongwook Kim, "The effect of current and conductance inputs on firing rate resonance in a stellate cell model," *Rutgers Behavior and Neural Sciences Mini-symposium*, Rutgers University at Newark, November 8, 2010.

Dongwook Kim, "Dynamics of medial entorhinal cortex layer II stellate cells receiving periodic and non-periodic inputs," *NJIT Applied Mathematics Summer Seminar Series 10*, Department of Mathematical science, NJIT, June 15, 2010.

Dongwook Kim, "The effects of periodic and non-periodic inputs on the dynamics of a medial entorhinal cortex layer II stellate cell model," *NJIT FACM (Frontiers in applied and computational mathematics) 10* , Department of Mathematical science, NJIT, June 15, 2010.

Unlike chess and its different pieces and complicated rules, Go is played with black and white stones equal in value, seemingly making it compatible with the binary nature of computers. Since the aim of a move is to control the most territory, the optimal move yields the maximum amount of territory—a simple counting procedure and a chore computers excel at. Yet in spite of the efforts of the world's best programmers over the last 30 years, the level of computer Go remains about that of a human who has studied Go for a month.

Richard Bozulich

ACKNOWLEDGMENT

First of all, I would like to thank my advisor, Professor Horacio G. Rotstein, for his tremendous assistance with this dissertation. From beginning to end, he has been a steadfast source of information, ideas, support, and energy. I am deeply grateful for his guidance, patience, and encouragement during graduate program in NJIT and I will be forever grateful for his trust and support that this dissertation could be completed. I also would like to extend my gratitude to the other members of my committee for their encouragement and support throughout my years in graduate school as well as through the process of researching and writing this dissertation: Professor Farzan Nadim, Professor Jorge Golowasch, Professor Victor V. Matveev, and Professor Vijayalakshmi Santhakumar. Finally, I would like to thank my family for their support and encouragement: my parents and my parents in law. I would quite simply not have completed this project without the support and encouragement of my wife, Jinkyoung Lee.

TABLE OF CONTENTS

Chapter **Page**

TABLE OF CONTENTS
(Continued)

Chapter **Page**

TABLE OF CONTENTS
(Continued)

Chapter **Page**

TABLE OF CONTENTS
(Continued)

Chapter **Page**

LIST OF FIGURES

Figure **Page**

LIST OF FIGURES
(Continued)

Figure **Page**

LIST OF FIGURES
(Continued)

Figure **Page**

LIST OF FIGURES
(Continued)

Figure **Page**

LIST OF FIGURES
(Continued)

Figure **Page**

LIST OF FIGURES
(Continued)

Figure **Page**

LIST OF FIGURES
(Continued)

Figure **Page**

LIST OF FIGURES
(Continued)

Figure **Page**

CHAPTER 1

INTRODUCTION

Neural activity often oscillates at specific frequencies or frequency bands. Neural oscillations are ranged from very slow oscillations with periods of minutes to very fast oscillations with frequencies reaching 600 Hz [1]. Those oscillations are believed to be involved in processing of visual and spatial information at multiple time scales [2, 3, 4, 5]. Frequency bands can be detected by electroencephalography (EEG) recordings which are the recording of electrical activity produced by the firing of neurons within the brain. One of the most studied rhythms is the theta rhythm (4-12 Hz)[4]. Theta frequency oscillations have been observed in various area of brain including the entorhinal cortex and the hippocampus [4]. When a rat is engaged in active motor behavior such as walking or exploratory sniffing, and also during REM (dreaming) sleep [6, 7]. In addition, theta frequency oscillations are believed to be involved in spatial learning, memory and navigation [3, 4]. Other frequency bands are labeled the delta (1-4 Hz) (known as slow-wave sleep and characterizing the depth of sleep), beta (13-30 Hz) (normal waking consciousness) and gamma (30-70 Hz) frequency (closely associated with sensory processing and creating the unity of conscious perception)[2].

In this thesis we focus on theta rhythmic activity in the medial entorhinal cortex (MEC). The MEC is the interface between the neocortex and the hippocampus. Studies of cortical connectivity have shown that the superficial layers (II and III) of the MEC receive convergent inputs from various neocortices and these convergent information is delivered to the hippocampus via the perforant path [8, 9] which provides a connectional route from the entorhinal cortex to various areas on the

hippocampal formation, including the dentate gyrus, CA1, CA3, and the subiculum. Conversely, the hippocampus feeds back onto layer V of the MEC and this information flows back from the MEC to the neocortices.

Electrophysiological behavior of the MEC is characterized by the presence of robust rhythmic activity in the theta frequency band [10]. In layer II, it is generated primarily by so called stellate cells (SCs) which are the most abundant cell type and the main component of the perforant path. *In vitro* experiments and theoretical studies using biophysical (conductance-based) models [7, 11] have shown that SCs have the intrinsic and dynamic properties that endow them with the ability to display rhythmic activity in the theta frequency band which persist during synaptic transmission block, as originally demonstrated by [12]. More clearly, SCs display rhythmic subthreshold membrane potential oscillations in the theta frequency range and, when the membrane is set positive to threshold, SCs fire action potentials at the peak of the subthreshold oscillations, but not necessary at every subthreshold oscillation cycle [7]. These subthreshold oscillations have been shown to result from the interaction between a persistent sodium and a hyperpolarization-activated (h-) currents [7, 11]. With different levels of injected I_{app} current, SCs show subthreshold oscillations, action potentials and coexistence of subthreshold oscillations and action potentials. Because of these intrinsically rhythmic properties, SCs may play a role in the generation of theta oscillations in the hippocampus [6]. It has been suggested that theta oscillations create the appropriate temporal dynamics between presynaptic activity and post-synaptic excitability that favors synaptic plasticity [4]. And it has also been proposed that the MEC might contribute to its memory functions through synchronizing mechanisms [13] by which the activity patterns of multiple cortical inputs that converge on MEC neurons may be temporally coordinated for the production of a memory representation

[4, 14]. For these reasons, the investigation and the understanding of the mechanisms underlying processing information are of great importance [15].

Various neuron types exhibit sub-threshold and firing frequency resonance in which the sub-threshold membrane potential or firing frequency responses to periodic inputs peak at a preferred frequency (or frequencies). Previous experimental works have shown that medial entorhinal cortex layer II stellate cells(SCs) exhibit subthreshold and firing frequency resonance in the theta frequency band (4 - 12 Hz)[16, 17]. An important question for cell's resonance is whether and under what conditions the subthreshold resonant properties of a neuron are communicated to the supra-threshold regime and are reflected in the neuron's firing frequency properties. Analytically, these issues have been addressed by other authors [16, 18] using linear models. Here we investigate these questions in the context of the model (described in chapter 2 Model). We studied the effects of both sinusoidal current and conductance-based inputs in different input frequencies on the supra-threshold dynamics on a SC model. For current inputs, our results show that while the SC model exhibits a single frequency preference peak (in the theta band) for low sinusoidal input levels, it exhibits three preferred frequency peaks for larger input levels. These additional peaks occur at frequencies that are roughly a multiple of the "theta" one. For synaptic conductance inputs, we observe an additional peak in the signal gain which occurs at a much higher frequency (in the high gamma band). These findings depart from the linear prediction. The linear SC model exhibits a single frequency preference peak for low input level. However, this model cannot capture three preferred frequencies peaks for higher input level. We suggest that this linear model is not appropriate to reproduce non-linear properties of firing frequency preference on SC.

Previous experimental work has shown that medial entorhinal cortex (MEC) layer II stellate cells (SCs) exhibit subthreshold oscillations and resonance in the theta

frequency band [16, 17, 19]. These intrinsic properties of SCs play an important role in the activity of neural networks in the entorhinal cortex and hippocampus[4]. An interesting question is under what conditions subthreshold oscillations on SCs can be generated at the theta frequency band in the presence of *in vivo-like* synaptic inputs. In a recent study, Fernandez et al. [20] have shown that subthreshold oscillations in SCs are reduced under high-frequency Poisson-distributed trains of combined excitatory and inhibitory conductance-based synaptic inputs while these oscillations does not change under current-based synaptic inputs. In this thesis, we investigated the mechanism underlying these phenomena in the context of the model, described in chapter 2. More specifically, we studied the effects of both conductance- and current-based synaptic inputs at various maximal synaptic conductance values on a SC model. We found that conductance-based synaptic inputs reduce subthreshold oscillations for low enough value of the maximal synaptic conductance value but amplify these oscillations at a higher range. This is in contrast to the experimental results [20].

CHAPTER 2

MODEL

2.1 Biophysical models for stellate cell

We use a single-compartment biophysical (conductance-based) neuron model, introduced by [15], which is based on measurement from layer II stellate cell (SC) of the medial entorhinal cortex (MEC)[7, 21, 22]. This model has the standard action potential producing Hodgkin-Huxley sodium (I_{Na}), potassium (I_K) and leak current (I_L). And tow additional currents, a persistent current (I_p) and a hyperpolarization-activated, mixed cation current called the h-current (I_h) [7], that have been shown to be responsible for the generation of subthreshold oscillations [11]. This model has been used to explain the synchronization properties of strongly coupled excitatory SCs [15]. The current balance equation for single SCs is

$$C\frac{dV}{dt} = I_{app} - I_{Na} - I_K - I_L - I_h - I_p \tag{2.1}$$

where V is the membrane potential (mV), C is the membrane capacitance ($\mu F/cm^2$), I_{app} is the applied bias (DC) current ($\mu A/cm^2$), $I_{Na} = G_{Na}m^3h(V_s - E_{Na})$, $I_K = G_K n^4(V_s - E_K)$, $I_L = G_L(V_s - E_L)$, $I_h = G_h(0.65r_f + 0.36r_s)(V_s - E_h)$, and $I_p = G_p p(V_s - E_{Na})$. In equation(2.1), G_x and E_x ($x = Na, K, L, p, h$) are the maximal conductances (mS/cm^2) and reversal potential (mV) respectively, The units of time are $msec$. All the gating variables x ($x = m, h, n, p, r_f, r_s$) obey a first order differential equation of the following form:

$$\frac{dx}{dt} = \frac{x_\infty(V) - x}{\tau_x(V)} \tag{2.2}$$

where the activation and inactivation curves and voltage-dependent time scales are given respectively by

$$x_\infty = \frac{\alpha_x(V)}{\alpha_x(V) + \beta_x(V)} \quad and \quad \tau_x(V) = \frac{1}{\alpha_x(V) + \beta_x(V)} \tag{2.3}$$

Unless stated otherwise, we use the following parameter values: $E_{Na} = 55$, E_K = -90, E_L = -65, E_h = -20, $G_{Na} = 52$, $G_K = 11$, $G_L = 0.5$, $G_p = 0.5$, $G_h = 1.5$ and C = 1. The definition of α_x and β_x are given in Appendix. Graphs of $x_\infty(V)$ and $\tau_x(V)$ for the gating variables are presented in Figure 1. We use the following parameter values: $E_{Na} = 55$, E_K = -90, E_L = -65, E_h = -20, $G_{Na} = 52$, $G_K = 11$, $G_L = 0.5$, $G_p = 0.5$, $G_h = 1.5$, and $C = 1$.

2.1.1 Channel white noise in persistent sodium channel

Many modeling studies have introduced channel noise in order to obtain robust subthreshold oscillations (STOs) [21, 22, 23]. White et al [21] showed that the number of persistent Na^+ channels underlying STOs is relatively small, and argued that the stochastic behavior of these channels may contribute crucially to the cellular level responses. Fransen et al. [22] used a noisy model having I_p and a two component I_h. They concluded that, although noise is not required for the SC to display STOs, its presence increases their robustness [22]. We introduce channel white noise in the persistent sodium current (I_p)[11, 21]. More specifically, we added a following stochastic term ζ to the dynamic equation for p.

$$\frac{dp}{dt} = \frac{p_\infty - p + \zeta}{\tau_p} \tag{2.4}$$

Where ζ represents Gaussian noise with zero mean value and variance appropriate for equilibrium conditions at the current value of membrane potential. For a population

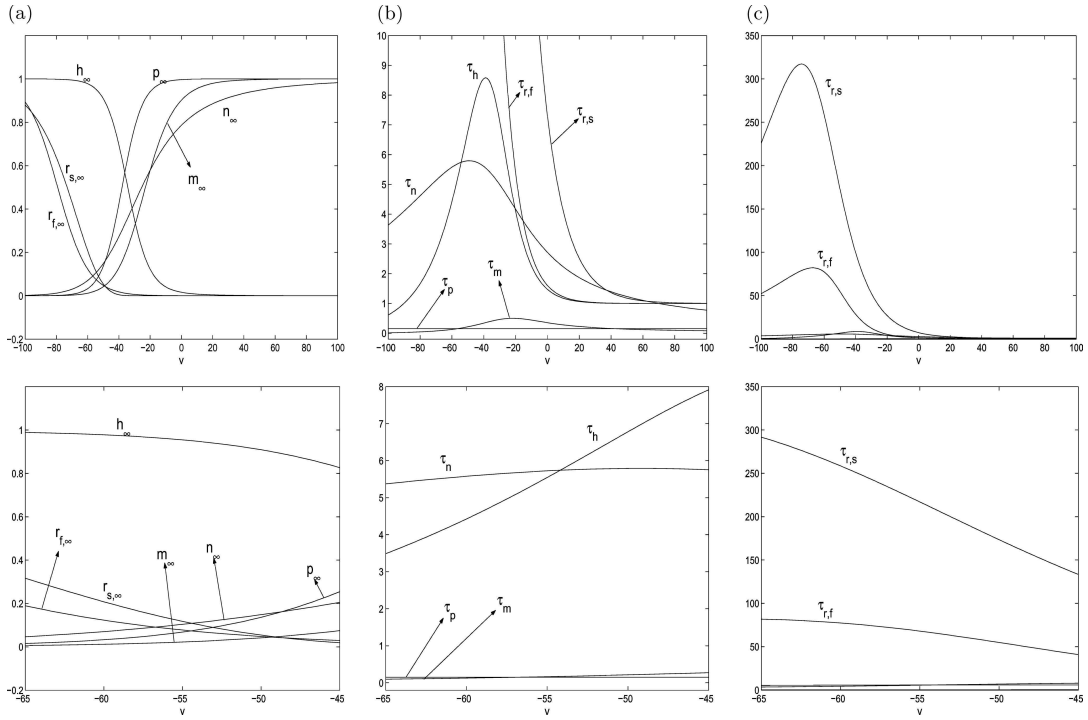

Figure 2.1 Ion channel dynamics for the full SC model. The gating variables are $x = m,\ n,\ h,\ p,\ r_f,\ r_s$. The bottom graphs are the magnification of the top graphs. (a) Activation and inactivation curves ($x_\infty(V)$) for the gating variables. (b) Voltage-dependent times scales ($\tau_x(V)$) for the gating variables. Both τ_{r_f} and τ_{r_s} evolve on time scales much slower than the other variables. This indicates that there exists a separation of time scales. (c) Voltage dependent time scales in a larger time interval. This figure is reproduced from [11]

of N channels and a time step dt, ζ can be implemented by adding the term

$$\zeta = \sqrt{\frac{-2dt(\alpha_p(1-p)+\beta_p p)ln(r_1)}{N}}cos(2\pi r_2)$$

to the gating equation at each time step [23, 24]. In this equation, r_1 and r_2 are pseudo-random numbers drawn from a uniform distribution over (0,1].

2.2 Biophysical reduced 3D NAS SC Model

Rotstein et al.[11] studied the mechanism of generation of subthreshold oscillations and the onset of spikes in the SC model (Eq. 1). Using dimensionality reduction methods they uncovered a three-dimensional model that captures the dynamics of the SC in the subthreshold voltage regime [11] where subthreshold oscillations are generated and the onset of spikes occur. This reduced model provides a good approximation to the full SC model in that regime. This reduced 3D model describes the evolution of the membrane potential V and the two h-current gating variables r_f and r_s (fast and slow respectively). Notably, I_{Na} and I_K were found to have a negligible effect on subthreshold dynamics and thus, were omitted from the reduced model [11]. The persistent sodium gating variable p evolves much faster than the remaining gating variables and the adiabatic approximation $p = p_\infty(V)$ was made. The resulting equations are

$$C\frac{dV}{dt} = I_{app} - G_p p_\infty(V)(V - E_{Na}) - I_L - I_h \tag{2.5}$$

$$\frac{dr_f}{dt} = \frac{r_{f,\infty}(V) - x}{\tau_{r,f}(V)} \tag{2.6}$$

$$\frac{dr_s}{dt} = \frac{r_{s,\infty}(V) - x}{\tau_{r,s}(V)} \tag{2.7}$$

where $I_{p,\infty}(V) = G_p p_\infty(V)(V - E_{Na})$. Equations (5)-(7) describe the dynamics of the SC in subthreshold regime, including both the generation of subthreshold oscillations and the onset of spikes [11], but they do not describe the spike dynamics which belong in a different regime (where I_{Na} and I_K are the main active currents). If spiking dynamics are not of interest but only the occurrence of spikes, the dynamics of a SC can be approximately described by Eqs. (5)-(7) supplemented with a zero width artificial spike (occurring on a short time scale and reaching a peak of about 60mV) and an appropriate threshold (V_{th}) and reset (V_{rst}) values. This reduced model was termed the Nonlinear Artificially Spiking SC (NAS-SC) model [11]. It is a class of model that includes the generalized integrate-and-fire (GIF) and resonate-and-fire models [25]. They choose V_{th} such that it lies close to the end of the subthreshold regime. Once the trajectory reaches the threshold value the voltage is reset to its initial, subthreshold value. Note that in contrast to other models, crossing V_{th} is not part of the mechanism of spike generation and only indicates spike occurrence [11]. The onset of spikes, however, is accurately described by Eqs. (5)-(7). The reset values $r_f = 0$ and $r_s = 0$ can be derived from the seven-dimensional SC model [11]. The reset value $V \approx$ -80 mV is an estimate from our numerical simulations. Thus the initial conditions in the subthreshold regime is (V, r_f, r_s) = (-80, 0, 0). They reset the trajectory to these values after each spike has occurred.

As in the 7D model, we added white Gaussian noise in the persistent sodium channel. In order to add noise in 3D model, we added the noise terms in p_∞ term in Eq. 14 by $p_\infty + \zeta$ where ζ is the Gaussian noise with mean value of zero and variance 1.

2.3 Linearized 3D NAS SC Model

Consider Eq. (5)-(7) with I_{app}=0 and call

$$F(V, r_f, r_s) = -\frac{1}{C}(I_L + I_{p,\infty}(V) + I_h) \tag{2.8}$$

$$G_f(V, r_f) = \frac{r_{f,\infty}(V) - r_f}{\tau_{r_f}} \tag{2.9}$$

$$G_s(V, r_s) = \frac{r_{s,\infty}(V) - r_s}{\tau_{r_s}} \tag{2.10}$$

Let the fixed point (V^*, r_f^*, r_s^*) satisfy $F(V^*, r_f^*, r_s^*) = 0$, $r_f^* = r_{f,\infty}(V^*)$ and $r_s^* = r_{s,\infty}(V^*)$ then the linearized 3D SC model around the fixed point (V^*, r_f^*, r_s^*) is given by

$$\frac{dV}{dt} = F_V^*(V - V^*) + F_{r_f}^*(r_f - r_f^*) + F_{r_s}^*(r_s - r_s^*) \tag{2.11}$$

$$\frac{dr_f}{dt} = G_{f,V}^*(V - V^*) + G_{f,r_f}^*(r_f - r_f^*) \tag{2.12}$$

$$\frac{dr_s}{dt} = G_{s,V}^*(V - V^*) + G_{s,r_s}^*(r_s - r_s^*) \tag{2.13}$$

The standard linearization we use here is different from the normalized linearization used in [18]

$$\frac{d}{dt} = -gv - g_f w_f - g_s w_s \tag{2.14}$$

$$\tau_f \frac{dw_f}{dt} = v - w_f \tag{2.15}$$

$$\tau_s \frac{dw_s}{dt} = v - w_s \tag{2.16}$$

where

$$w_f = \frac{r_f - r_f^*}{r'_{f,\infty}(V^*)}, \qquad w_s = \frac{r_s - r_s^*}{r'_{s,\infty}(V^*)} \tag{2.17}$$

and $\tau_f = \tau_{r_f}$, $\tau_s = \tau_{r_s}$, $g = -F_V^*$, $g_f = -F_{r_f}^*$, $r'_{f,\infty}(V^*) = G_h 0.65(V^* - E_h) r'_{f,\infty}(V^*)$ and $g_s = -F_{r'_{s,\infty}}^*(V^*) = G_h 0.35(V^* - E_h) r'_{s,\infty}(V^*)$.

CHAPTER 3

FIRING RATE FREQUENCY PREFERENCES IN A STELLATE CELL MODEL

Various neuron types exhibit sub-threshold and firing frequency resonance in which the sub-threshold membrane potential or firing frequency responses to periodic inputs peak at a preferred (resonant) frequency (or frequencies). Previous experimental work has shown that medial entorhinal cortex layer II stellate cells(SCs) exhibit subthreshold and firing frequency resonance in the theta frequency band (4 - 12 Hz)[16, 17]. An important question for cell's resonance is whether, and under what conditions, the subthreshold resonant properties of a neuron are communicated to the supra-threshold regime and therefore are reflected in the neuron's firing frequency properties. These issues have been addressed both analytically and numerically by other authors [16, 18] using linear models. Here we investigate these questions in the context of the model (see chapter 2 model). We studied the effects of both sinusoidal current and conductance-based inputs in terms of the input frequency, (with and without noise), on the supra-threshold dynamics. For current inputs, our results show that while the SC model exhibits a single frequency preference peak (in the theta band) for low sinusoidal input levels and this peak-frequency coincides with subthreshold resonance frequency, it exhibits three preferred frequency peaks for larger input levels. These additional peaks occur at frequencies that are roughly a multiple of the "theta" one. For synaptic conductance inputs, we observe an additional peak in the signal gain (firing rate divided by the amplitude of input current) which occurs at a much higher frequency (in the high gamma band). These findings depart from the linear prediction; i.e., from the behavior of the corresponding

linearized models. The linear SC model exhibits a single frequency preference peak for low input levels. However, this model cannot capture three preferred frequencies peaks for higher input level. We show that this linear model is not appropriate to reproduce non-linear properties of firing frequency preference on SC.

3.1 Background

3.1.1 Subthreshold oscillations

Neurons display rhythmic behavior such as subthreshold oscillations, action potential , and mixed mode oscillations (coexistence of subthreshold oscillations and action potentials). When membrane potential of neurons reaches from below a critical voltage threshold, they generate action potentials. Subthreshold oscillations were originally discovered in the mammalian inferior olive nucleus cells [26]. These oscillations are related to the intrinsic properties of neurons such as their passive properties and ionic currents. It has been observed that the medial entorhinal cortex layer II stellate cells (SCs) generated persistent rhythmic subthreshold voltage oscillations[14]. The mean frequency of these oscillations is 8.6 Hz (theta frequency band) and the mean amplitude of these oscillations is 2.6$\pm$0.5 mV. Subthreshold oscillations in SCs were not present at the resting potential or below and gradually developed, growing in amplitude and frequency when the cells were depolarized positive to -60 mV. This intrinsic oscillatory phenomenon is not Ca^{2+} dependent but depends on the activation of a persistent sodium conductance [12, 27]. Dickson et al. showed that the interaction between a hyperpolarized activated h current, I_h and persistent sodium current, I_p generates subthreshold oscillations in SCs [7]. Furthermore, Dickson et al proposed that I_h is necessary to generate subthreshold oscillations. It has been studied the dynamic structure underling subthreshold oscillations with the nonlinear artificial

spiking (NAS) model [11]: dynamic structure of the interaction between I_p and I_h explains subthreshold oscillations and mixed mode oscillations in SCs.

3.1.2 Subthreshold resonance

Different behavior and perceptual states of the brain are associated with different brain rhythms. These rhythms are characterized by the behavior of individual neurons, which determine the information processing in neural networks, controlled by both intrinsic properties and network. These intrinsic properties of cells stem from the interaction between passive membrane properties and active conductance of ionic channels. To what extent does this determine the characteristic frequency range of network rhythmic activity? It has been argued that individual neurons have frequency preferences which endow them with spontaneous membrane oscillations and allow them to respond best to inputs at fixed frequency, so-called subthreshold resonance [28]. Various neuron types exhibit subthreshold resonance [28, 29, 30, 31] in which the response of the induced oscillating voltage to sinusoidal inputs peaks at a preferred input frequency. For example, subthreshold resonance is observed in trigeminal root ganglion neurons [31], inferior olive neurons [30], thalamic neurons [29], hippocampal pyramidal neurons [32] and medial entorhinal cortex layer II stellate cell [16, 17]. Subthreshold resonance is generated by interaction between low pass filter (capacitance) and high pass filter properties (slow activated ionic current which oppose change in the membrane potential) [28]. There are analytical and experimental evidence that there is a strong relationships between subthreshold membrane oscillations and subthreshold resonance frequency [16, 17, 25, 28, 33].

3.1.3 How subthreshold resonance is generated

In order to generate subthreshold resonance, it is necessary to have two main components: (1) passive membrane property of cell and (2) slow activated ionic current(s) which oppose changes in membrane potential. The first component acts as low pass filter and the second one acts as high pass filter. There are two important criteria for ionic currents to act as high pass filter: (1) ionic currents must oppose changes in membrane oscillations and (2) activate slowly relative to the membrane time constant. i.e. the time constant of ionic current must be slower than membrane voltage time constant to make membrane voltage to damped oscillations which are the time-domain signature of resonance. There are two types of currents which control the shape of impedance (frequency and amplitude in the impedance curve): resonant and amplifying. Resonant currents determine the cell's frequency preference. Amplifying currents enhance impedance (resonance) without greatly changing the resonance frequency. Figure 3.1(a) shows how interaction between passive properties and ionic current (I_K : resonant current and I_{Nap} : amplifying current) generates cell resonance. As shown in a and b in Figure 3.1(a), I_K reduced the voltage changes. In other words, I_K attenuates low frequencies and acts as a high pass filtering in respond membrane potential to ZAP current. I_K is enough to generate resonance but with I_{Nap}, the output of voltage potential more responds to ZAP current at the certain frequency (Figure 3.1(a) c). Figure 3.1(b) indicates that both the passive property of cell and the resonant current separately contributes to generate resonance in the impedance. The dot line indicates the contribution of I_K and gray line shows the contribution of passive membrane property.

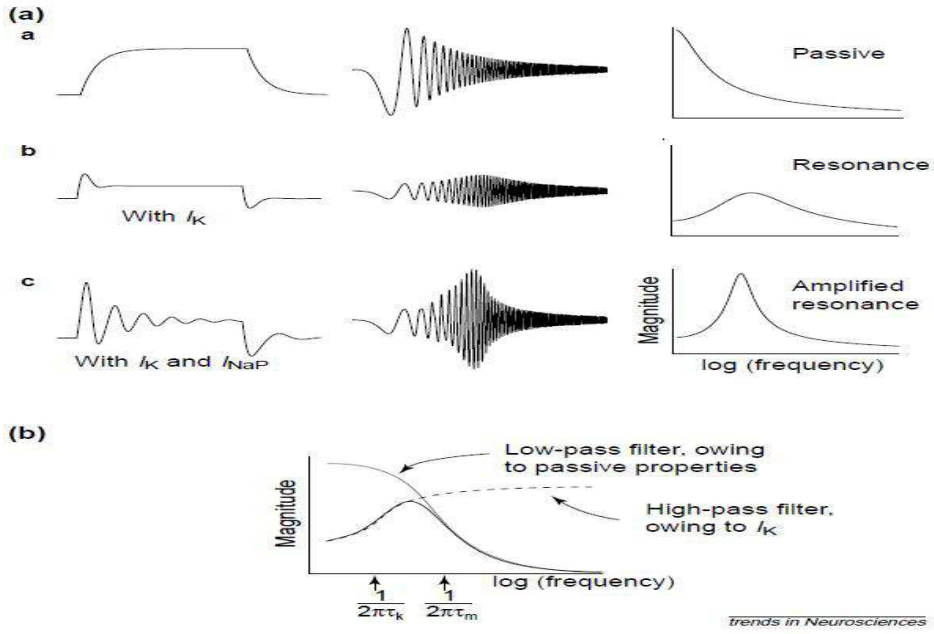

Figure 3.1 Resonance is created by an interplay between passive properties of cell and slow activated ionic current. The figure is reproduced from [28].

3.1.4 Previous studies about relationship between sub- and supra-threshold resonance

There is much research focused on subthreshold resonance [16, 17, 19, 26, 28, 31, 32, 33, 34, 35]. However, few studies have examined the effect of subthreshold resonance on the temporal properties of the firing rate. In Richardson et al [18], the link between subthreshold resonance and firing rate was examined in the framework of two conductance based models (linearized generalized integrate-and-fire model). They investigated the effect of synaptic noise inputs on firing frequency preferences and the relationship between sub- and supra-threshold resonance. When the synaptic noise is weak and firing regular, supra-threshold resonance frequency is the firing rate itself. When the synaptic noise is strong and firing irregular, supra-threshold resonance frequency is the strongest at the subthreshold resonance frequency. In this work, the

firing rate of the cell without synaptic inputs, called natural firing rate, is important. When the natural firing rate of cell is less than subthreshold resonance frequency, then supra-threshold resonance frequency is near subthreshold resonance frequency. However, when the natural firing rate is greater than subthreshold resonance frequency, then the strength of synaptic noise determines supra-threshold resonance frequency i.e. supra-threshold resonance frequency is near either subthreshold resonance frequency or firing rate itself depended on noise strength [18, 36]. Engel et al.[19] studied the relationship between subthreshold resonance and firing rate in entorhinal cortex layer II stellate cell [19]. They showed that subthreshold resonance shapes spike-train patterns: spike patterns in stellate cells exhibited two different timescales reflecting inter- and intra-cluster inters pike intervals and increasing the firing rate decreased the inter-cluster inter spike intervals but did not affect intra-cluster inter spike intervals.

3.2 Methods

Resonance properties have been studied by injecting sinusoidal currents with fixed frequencies [32, 37] or ZAP current whose frequency varies monotonically in time [28, 31, 34]. In our simulations, we used following time-dependent current and synaptic inputs

$$I_{in}(t) = A_{in} \sin(2\pi f t/1000) \tag{3.1}$$

$$I_{syn}(t) = G_{syn,in} \frac{1}{2}(1 + \sin(2\pi f t/1000))(V - E_{syn}) \tag{3.2}$$

where A_{in} $(\mu A/cm^2)$ and $G_{syn,in}$ (mS/cm^2) are a non-negative constant and the frequency f is measure in Hz. For simplicity, in some cases we express the frequency in terms of the variable ω

$$\omega = 2\pi f \tag{3.3}$$

3.2.1 Subthreshold resonance: Impedance and impedance-like function

A system receiving a time-dependent current input $I_{in}(t)$ or synaptic-like conductance input $I_{syn}(t)$ exhibits subthreshold resonance if there is a peak in the magnitude of the impedance function defined as the quotient between the Fourier transforms of the voltage response $V_{out}(t)$ and the current input:

$$Z(\omega) = \frac{F[V_{out}(t)](\omega)}{F[I_{in}(t)](\omega)} \tag{3.4}$$

where F denotes Fourier transform. In order to evaluate the cell's voltage response for SC model, we use the following definition of impedance

$$Z(f) = \frac{V_{max}(f) - V_{min}(f)}{2A_{in}} \tag{3.5}$$

where $V_{max}(f)$ and $V_{min}(f)$ are the maximum and minimum of the oscillatory voltage response $V_{out}(f)$ for each value of the frequency f.

3.2.2 Supra-threshold resonance: Firing rate and Signal gain

In order to find firing rate corresponding to each input frequency (f), we follow Richardson et al [18]. We calculated the inter spike intervals of voltage trace in respond to sinusoidal current inputs and averaged those values over 15 sec time duration. From now, we call the reciprocal form of averaged inter spike interval average firing rate. We have checked that instantaneous firing rate is "almost" same as average firing rate in the SC model. Therefore, in our simulations, the calculation of average firing rate ($r(f)$) was used. Since the response $r(f)$ is proportional to the strength of the sinusoidal input current, we used signal gain ($|A(f)|$) that measures the ability of a neuron to amplify a particular frequency [18, 38]

$$|A(f)| = r(f)/A_{in} \tag{3.6}$$

In the same way as in the case of subthreshold resonance, the existence and position of the peak in $|A(f)|$ within frequency domain will be the corresponding firing-rate measure of resonance, called supra-threshold resonance [18]. We calculated both $r(f)$ and $|A(f)|$ with four different time durations for the injected sinusoidal currents: $5s$, $10s$, $15s$ and $30s$. We found that the precision of the measurement improves with increasing the time duration of I_{in} but it saturates at about $15s$. Accordingly, the time durations was set to $15s$. The frequency (f) of I_{in} is ranged from 0 to 100 Hz with step size 0.25 Hz. The amplitude (A_{in}) was used from 0 to 0.5 with step size 0.01.

3.3 The effect of current-based inputs on firing rate in 7D full stellate cell model

3.3.1 The relationship between sub- and supra-threshold resonance with small amplitude of sinusoidal currents

It has been suggested that there is a strong relationship between subthreshold oscillations and subthreshold resonance in SCs, that is, the frequency of subthreshold oscillations coincides with subthreshold resonance frequency [16, 17]. Previous modeling studies investigated the relationship between sub- and supra-threshold resonance using linear models [18, 19] and suggested that the supra-threshold resonance frequency can be predicted by the corresponding subthreshold resonance frequency when the amplitude of sinusoidal input currents are small enough. In this section, we investigate the effect of sinusoidal input currents on a range from 0.05 to 0.5 $\mu A/cm^2$ (higher than the one used in [18, 19]) on SC's firing frequency preference and how this firing frequency preference is related to the subthreshold resonance frequency with non-linear 7D SC models (equation 2.1 and 2.2). In order to study the effects of subthreshold resonance on the properties in firing rate, we began with the case where SC exhibits

only subthreshold oscillations to find the subthreshold resonance. This SC model with channel noise (noise strength D = 10^{-6}) exhibits subthreshold oscillations for I_{app} = -2.72 $\mu A/cm^2$ (figure 3.2A) and action potentials for higher value of I_{app}. Thus we set the control level when I_{app} = -2.72 $\mu A/cm^2$. First, we studied the intrinsic properties of cells (without any synaptic inputs) such as the frequency of subthreshold oscillations and subthreshold resonance frequency. For finding subthreshold resonance frequency, we use the sinusoidal input current with A_{in} = 0.01 $\mu A/cm^2$ on SC. The numerical simulations show that the power spectrum density (PSD) of subthreshold oscillations at the control level exhibits peak at 10 Hz (figure 3.2B) and subthreshold resonance frequency at 10 Hz in impedance curve (figure 3.2C). This implies that the frequency of subthreshold oscillations coincides with subthreshold resonance frequency in this model, which is in agreement with previous experimental results[16, 17]. Next, we examined SC's firing frequency preference with the amplitude (A_{in}=0.05 $\mu A/cm^2$ but still small) of injected sinusoidal current input. When the SC receives this small-amplitude sinusoidal input currents, we measure both average firing frequency and signal gain of the corresponding voltage traces in terms of input frequency f. As expected, for constant values of A_{in}, both signal gain and firing frequency curves are qualitatively similar since signal gain is proportional to A_{in}. Therefore those exhibit a single peak at 10 Hz (figure 3.2C) and the shape of these graphs are the same. The corresponding voltage trace at the peak (input frequency f=10 Hz) in average firing frequency is shown in figure 3.2D. In these simulations, the input frequency varied from 0 to 50 Hz but for higher frequency values, the corresponding voltage traces to sinusoidal current inputs shows only subthreshold oscillations (data not shown).

When the SC receives small-amplitude sinusoidal current inputs, it is reasonable to exhibit a peak in average firing rate with respect to input frequency at subthreshold resonance frequency since sinusoidal current input at the subthreshold resonance

frequency will be more likely to generate an action potential at local maximum of subthreshold oscillations. In other words, when the input frequency (f) is the subthreshold resonance frequency, SC responded most to sinusoidal current inputs at this frequency due to subthreshold resonance properties of SC. These numerical results are related to Richardson et al [18] and to the fact that subthreshold resonant properties of a SC are communicated to the supra-threshold activity and reflect in SC's firing frequency properties [17].

3.3.2 For large value of A_{in}, this model shows multiple peaks in the supra-threshold resonance profile

In this section, we examine supra-threshold resonance properties of SCs with increasing value of A_{in}. In these simulations, we observe multiple peaks in the supra-threshold resonance profile; i.e., the supra-threshold resonance properties can not be predicted by subthreshold resonance. Rather, they depend on the amplitude of the injected sinusoidal currents. Increasing the value of A_{in} results not only in an increasing firing rate but also in exhibiting multiple firing frequency preference in supra-threshold resonance. When SC receives strong sinusoidal input currents ($A_{in} = 0.2\ \mu A/cm^2$), three preferred frequencies have been observed in average firing rate curve (Figure 3.3A): f= 8, 16, and 21 Hz. The average firing frequency is 8 Hz, 8 Hz and 7 Hz respectively (figure 3.3B, C and D). Note that the firing rate at the first peak is in 1-1 correspondence with corresponding input frequency and the second peak-frequency is twice the first peak-frequency, but the corresponding firing frequency at those peaks is the same. Furthermore, we found a relation between input frequency and output firing frequency in average firing rate curve (Figure 3.3A): the firing frequency of corresponding voltage traces is in 1-1 (input frequency f–output firing rate) correspondence with input frequency f until it reaches first peak-frequency ($f =$

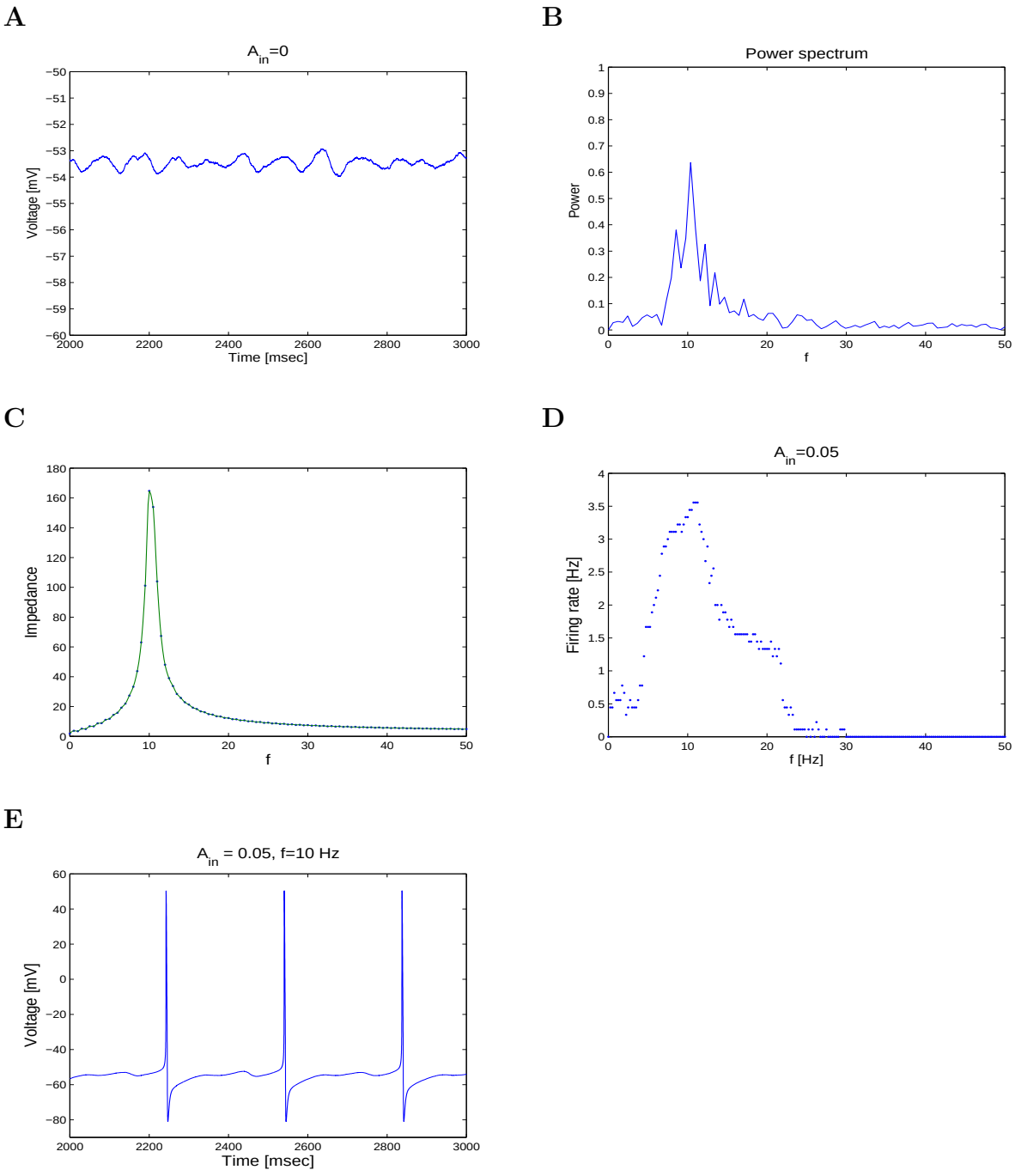

Figure 3.2 The effect of weak sinusoidal current inputs on the relationship between sub- and supra-threshold resonance using 7D SC model. A: voltage trace without sinusoidal input. B: the power spectrum density of A. C: impedance curve. SC model shows a peak at 10 Hz in impedance curve. This implies that SC has subthreshold resonance frequency at 10 Hz and response best to sinusoidal input with 10 Hz. D: input frequency versus firing rate. E: voltage trace with firing rate = 3.5 Hz when f=10 Hz.

8). But the output firing rate with respect to f decrease after the first peak-frequency and then starts increasing at $f = 10$ Hz with 2-1 correspondence with f until it reaches the second peak-frequency ($f = 16$). The average firing rate decreases and then starts increasing at $f = 15$ Hz with 3-1 correspondence with f until at the third peak-frequency $f = 21$ Hz. The corresponding voltage traces at those three peaks in Figure 3.3A are shown in figure 3.3B, C, and D. These voltage traces show two type of neural oscillations: mixed mode oscillations (at the second and third peak) and only action potentials (at the first peak). We will discuss these different type of oscillations and how these oscillations affect the average firing rate in section 3.4.2 (firing rate density).

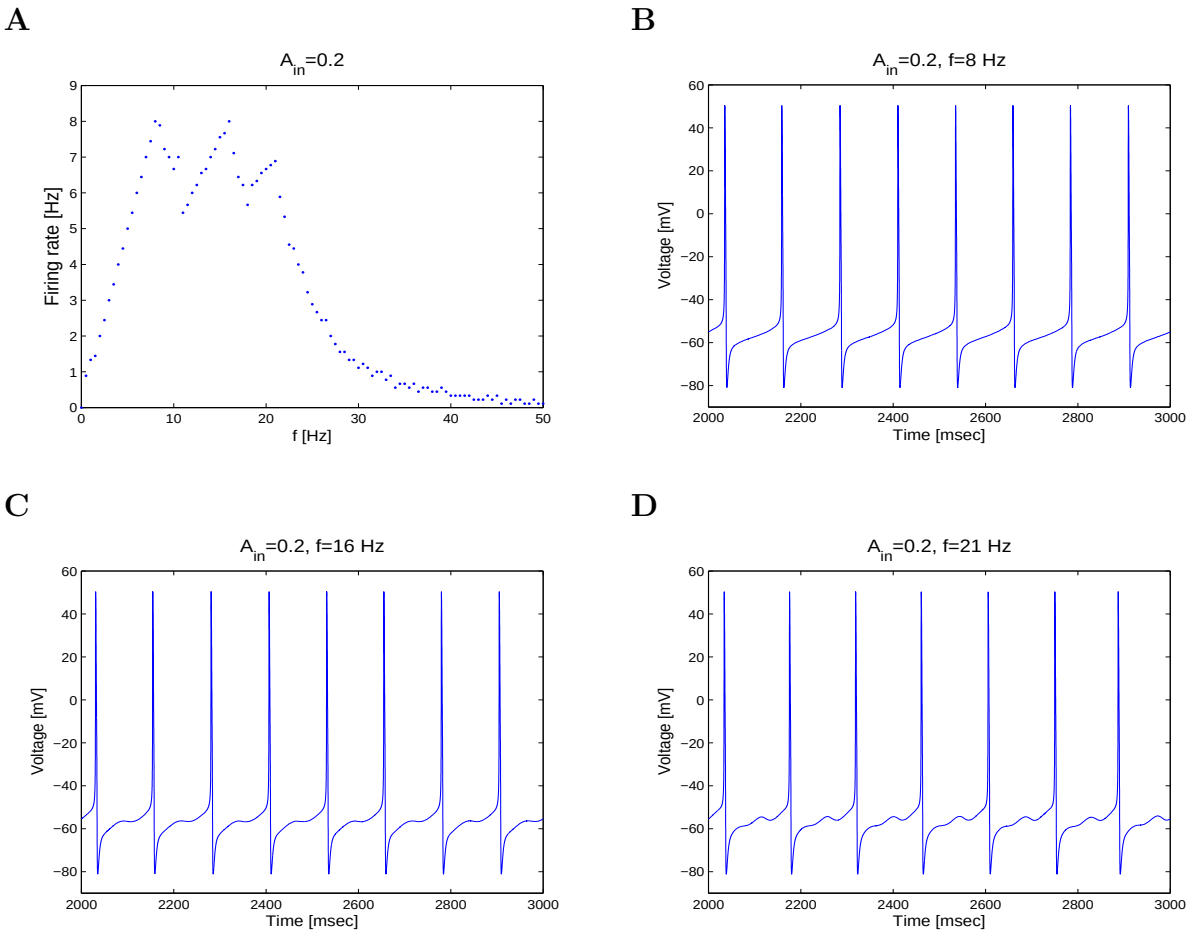

Figure 3.3 7D SC model. The effect of large value of A_{in} on firing rate. A: the firing rate in terms of input frequency using 7D SC model with A_{in} =0.2 $\mu A/cm^2$. The supra-threshold resonance frequencies are f = 8, 16, and 21 Hz. B, C, and D: voltage traces at supra-threshold resonance frequencies.

3.4 The effect of current-based input on frequency preference of stellate cell with 3D model

It has been proposed that the reduced 3D SC model captures the dynamic mechanism for generation of subthreshold oscillations in SCs [11] and the synchronization properties in networks using the full 7D SC model [15]. In this section, we investigate the firing frequency preference of SC using reduced 3D SC model. The goal of this section is that the reduced 3D SC model is appropriate to capture supra-threshold resonance properties which we observed in 7D SC model and understand the evolution of dynamical system underlying existence of multiple firing frequency preference in supra-threshold regime using phase-space analysis. We use the same parameters as in 7D SC model.

3.4.1 Supra-threshold resonance properties of SCs using 3D stellate cell model

We set the control level for which this model exhibits only subthreshold oscillations at I_{app} = -2.6 $\mu A/cm^2$ and use the same amplitude of sinusoidal inputs as used in full 7D SC model (see section 2.1). Figure 3.4 illustrates the relationship between subthreshold resonance (Figure 3.4C) and supra-threshold resonance (Figure 3.4D). Our numerical results show that subthreshold resonance properties are communicated to supra-threshold regime when SC receives weak sinusoidal current inputs with A_{in} = 0.05 $\mu A/cm^2$. This model shows a single peak in both sub- and supra-threshold resonance frequency at 10 Hz (Figure 3.4C and D). In addition, the frequency of subthreshold oscillations (Figure 3.4B) coincides with the subthreshold resonance frequency (Figure 3.4C). Furthermore, increasing A_{in} causes multiple preferred firing frequencies to emerge in the supra-threshold activity. More specifically, for $A_{in} = 0.2$,

this model shows three peaks in the average firing rate curve (Figure 3.5A). Three peaks occurred at $f = 7.25$, 14.5, and 19 Hz. The average firing frequencies at the first and second peak are 7.25 Hz but the average firing rate at the third peak is 6.3 Hz (lower than the other ones). Figure 3.5B,C and D show corresponding voltage traces at three peak-frequencies. Note that the firing rate at the first peak is in 1-1 correspondence with input frequency f and the second peak-frequency is twice the first peak-frequency. This model also captures the relationship between input frequency f and output firing rate as shown in 7D SC model: 1-1 correspondence with f until at the first peak-frequency ($f = 7.25$) , 2-1 correspondence with f until at the second peak-frequency ($f = 14.5$) and 3-1 correspondence with f until at the third peak-frequency ($f = 19$). These results are analogous to the results in the 7D SC model. Using the 3D SC model provided an accurate enough picture of the model's dynamics (or the sub- and supra-threshold resonance properties).

3.4.2 Firing rate density: comparison to average firing rate curve

In previous sections, we explained supra-threshold resonance properties of SCs using the calculation of average firing rate with respect to input frequency. However, depending on the model parameters and the input frequency, high-amplitude oscillatory input current induces regular (Figure 3.6C f=7 and 10 Hz) and irregular firing frequency (Figure 3.6c $f = 8$ and 9 Hz) in voltage response. Due to this irregular firing rate, it can be questioned that the calculation of average firing rate is enough to explain firing frequency preference on supra-threshold regime of SCs. In this section, we investigate how this irregular firing rate affects the average firing rate of corresponding voltage traces to sinusoidal current inputs. Here, we introduce the firing rate density to verify that the calculation of average firing rate is enough to explain supra-threshold resonance properties of SCs. The firing rate density is the

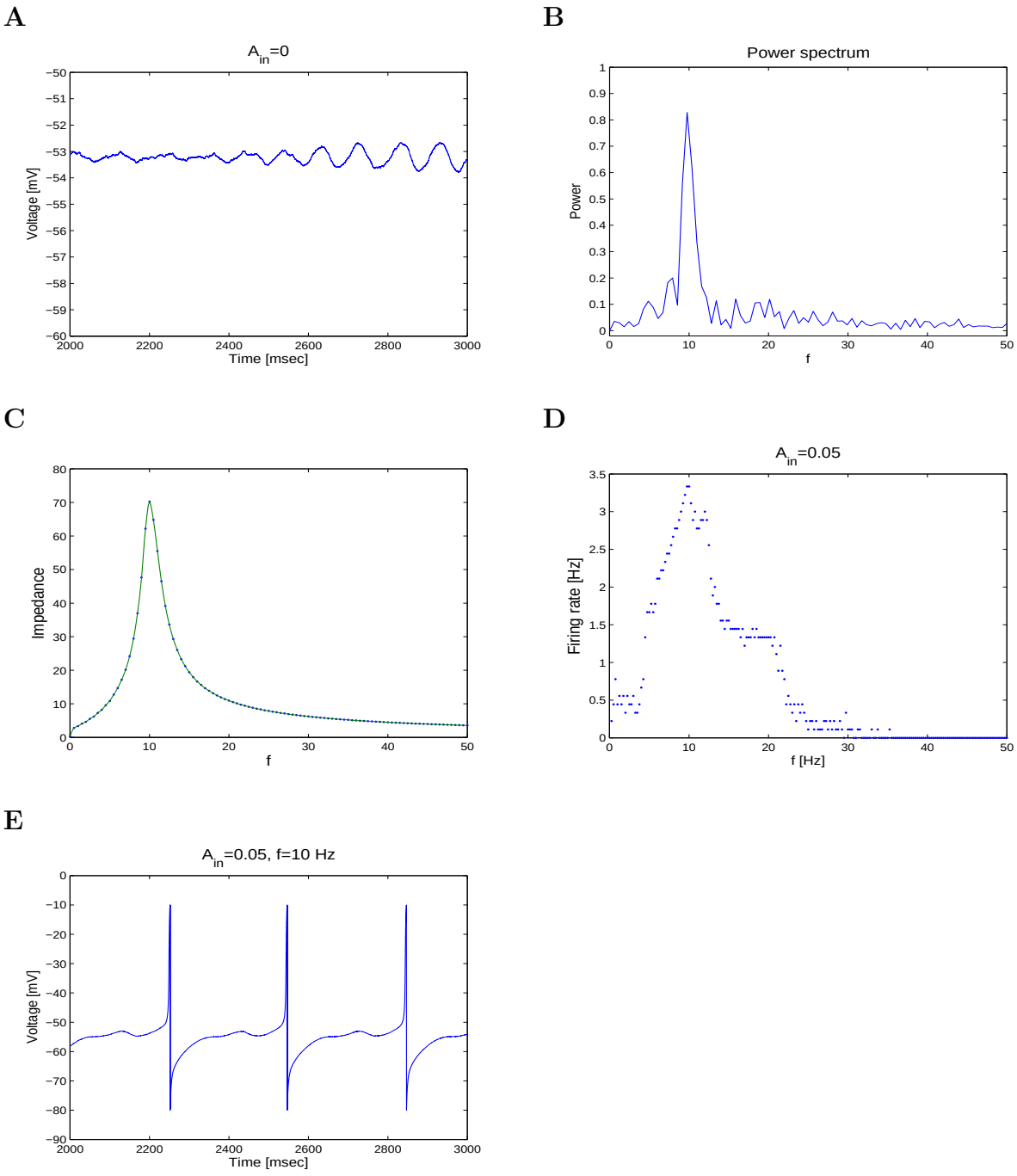

Figure 3.4 The effect of weak sinusoidal input on the relationship between sub- and supra-threshold resonance using the 3D SC model. A: voltage trace without sinusoidal input. B: the power spectrum density of A. C: Impedance curve (A_{in} = 0.005 $\mu A/cm^2$) which shows subthreshold resonance frequency is at 10 Hz. D: the average firing rate with respect to input frequency f (A_{in} = 0.05 $\mu A/cm^2$). There exists a peak at 10 Hz which indicates supra-threshold resonance frequency is 10 Hz. E: voltage trace with firing rate = 3.5 Hz for f=10 Hz.

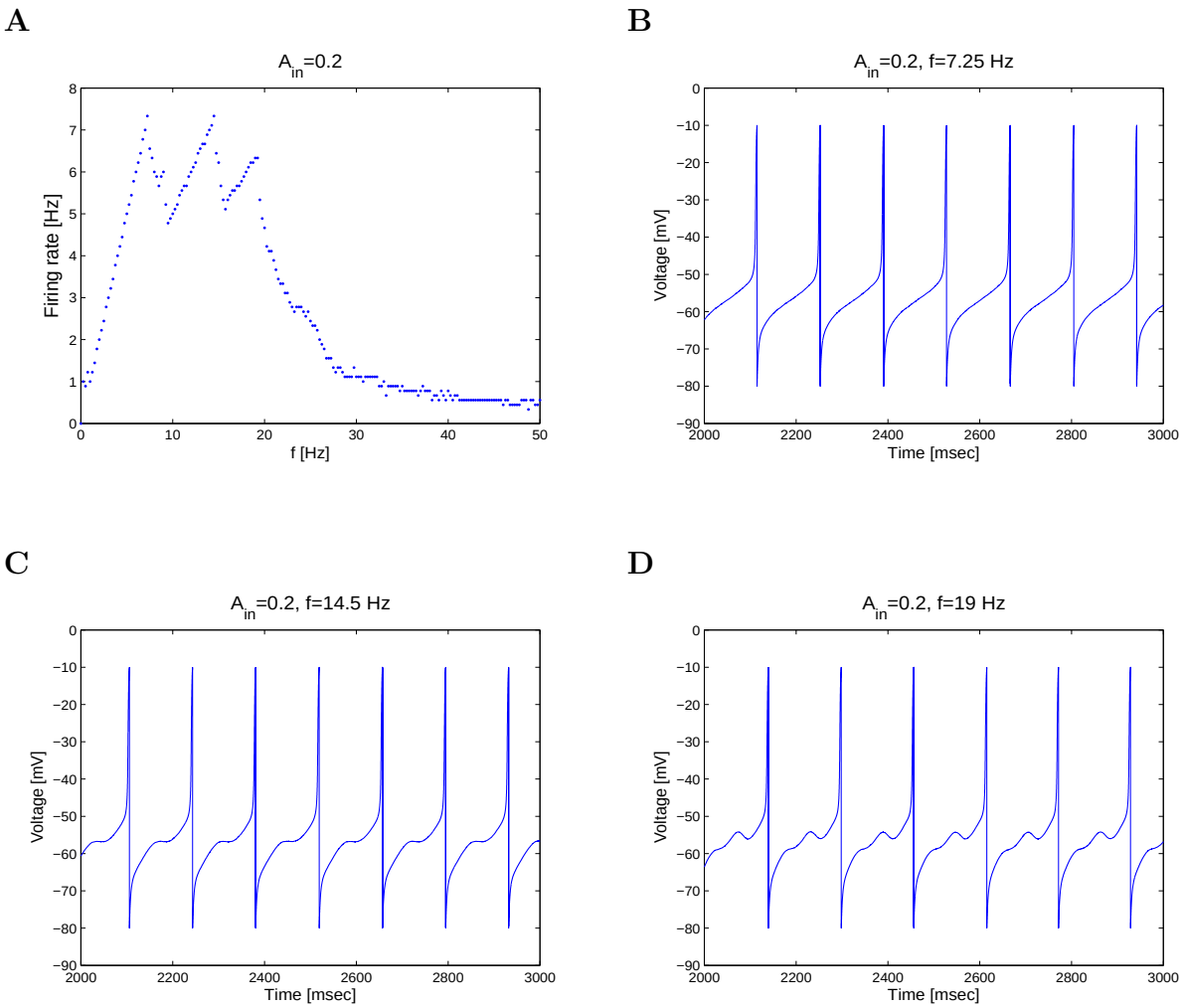

Figure 3.5 The effect of large value of A_{in} (=0.2 $\mu A/cm^2$) on firing rate using the 3D SC model. A: the average firing rate with respect to input frequency f. The supra-threshold resonance frequencies are shown at $f = 7.25$, 14.5, and 19 Hz. B, C and D: voltage traces at each peak-frequency f.

histogram (colorbar) of reciprocal form of interspike intervals (ISIs) over certain time duration (15 s). In Figure 3.6B, the color code is as follows: blue color means zero density (no action potentials) and red color indicates high density of ISIs.

We present both the average firing curve and firing rate density curve which are the function of input frequency in Figure 3.6. In this figure, we compare the average firing rate graph to the firing rate density graphs (Figure 3.6A and B). When the input frequency f increases from 0 to 7 Hz, this 3D model shows one type of ISI (regular firing rate). However, this model displays two ISIs (irregular firing rate) when input frequency $f = 8$ and 9 Hz. The corresponding voltage trances and histogram of these voltage traces are shown in Figure 3.6C left and right panel respectively. For f= 7 Hz, the voltage trace and those histogram display a constant ISI, 142 ms (firing frequency = 1000/142 = 7 Hz) and the length of ISI is 60 (Figure 3.6C right). For $f = 8$ Hz, the voltage traces show two ISIs, called the short ISI (142 ms, firing frequency = 7 Hz) and long ISI (217 ms, firing frequency = 4.6 Hz). In this case, the length of the short ISI is larger than the length of the short ISI. Therefore, when we take average all ISIs over time duration 15 *sec*, the average firing rate is 6.2798 Hz which is below the average firing rate at $f = 7$ Hz. For $f = 9$ Hz, the model shows two ISIs (short ISI = 139 ms, firing frequency = 7.2 Hz and long ISI = 192 ms, firing frequency = 5.2 Hz). The length of two ISIs are equal to each other (27). Therefore, when we take average all ISIs over the time duration, the average firing rate is 6.2073 which is below the average firing rate at $f = 8$ Hz. However, From $f = 10$ to second-peak frequency in Figure 3.6A and B, the voltage traces show one ISI (regular firing rate).

The firing rate density graph tells the mechanism underlying the existence of peak-frequency in supra-threshold activity of SCs. The irregular firing rate is a transition between two regular patterns. Once the firing frequency decrease from the maximum firing frequency with respect to input frequency, SCs display both

short and long interspike intervals. As input frequency increase, the length of short ISIs decreases but the length length of ISIs increases until SC show regular pattern in firing frequency. Therefore the average firing rate curve is enough to capture peak-frequency in supra-threshold resonance but it does not capture irregular pattern in firing frequency. From now on, we will use the firing rate density curve instead of using the average firing rate curve.

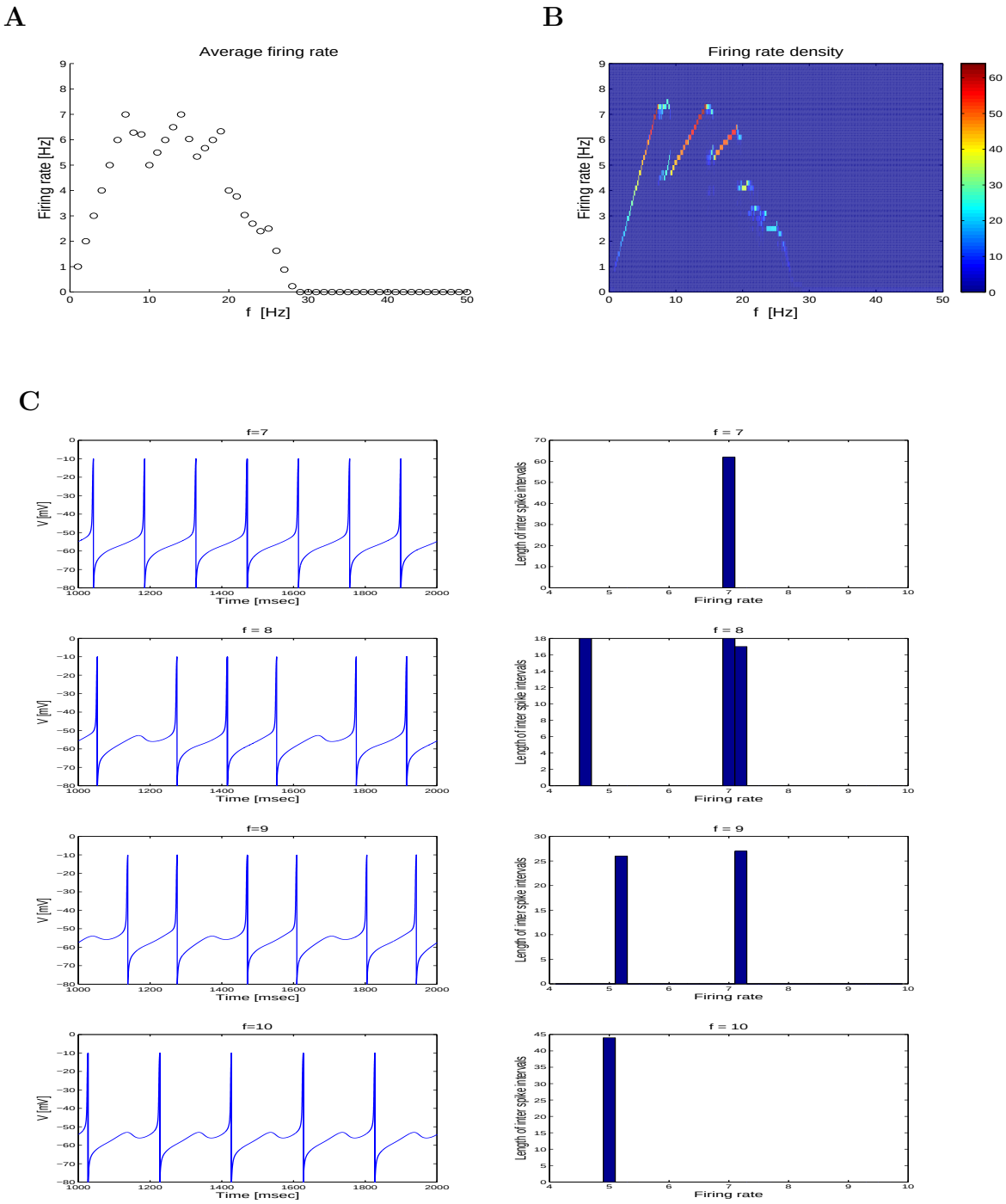

Figure 3.6 Averaged firing rate vs. firing rate density with A_{in} =0.2 using 3D SC model. (A): average firing rate with respect to input frequency. (B) : firing rate density with respect to input frequency. The colorbar indicates the length of interspike intervals. Firing density graph still exhibits multiple peaks in supra-threshold activity. (C) : voltage traces (left) and firing rate distribution (right) for f= 7, 8, 9 and 10 Hz. Average firing rate at f = 7, 8, 9 and 10 Hz is 6.9930, 6.2798, 6.2073, and 5 Hz, respectively.

3.4.3 The effect of A_{in} on both firing rate and signal gain

We have checked that supra-threshold resonance property depended on the amplitude A_{in} of sinusoidal input current in section 3.4.1. Subthreshold resonance property are communicated to supra-threshold activity in SC for small A_{in} while this communication is disconnected for higher value of A_{in}. In this section, we investigate the effect of A_{in} on both firing rate and signal gain by systemically increasing A_{in}. We use A_{in}, ranging from 0 to 0.5 with step size 0.01 $\mu A/cm^2$ and input frequency f is varied from 0 to 100 Hz.

Figure 3.7 shows the image of firing rate (Figure 3.7A) and signal gain (Figure 3.7B) : colorbar indicates firing rate and signal gain respectively (horizontal-direction is input frequency and vertical-direction is A_{in}). For each A_{in}, we calculated firing rate and signal gain as a function of input frequency f. These images show that increasing A_{in} not only increases firing rate but also generates multiple peak-frequencies in supra-threshold resonance. For small amount of sinusoidal input current, supra-threshold resonance frequency is seen at 10 Hz (subthreshold resonance frequency) but multiple peaks are seen for higher value of A_{in}. Increasing A_{in} also induces a shift of supra-threshold resonance frequencies to slightly higher frequency. However, the images show different results in both firing rate and signal gain. The signal gain decreases with increasing A_{in} (Figure 3.7B) while the firing rate increases with increasing A_{in} (Figure 3.7A).

Figure 3.8 shows firing rate and signal gain with respect to input frequency with various value of A_{in} (cutoff horizontal direction of both the image of firing rate and signal gain with various value of A_{in} in figure 3.7). In this figure, we see how firing rate and signal gain changes by increasing A_{in}. A single peak is seen at $f = 10$ Hz for $A_{in} = 0.05$, but two peak-frequencies are seen for $A_{in} = 0.1$ and these peak-frequencies show 1-1 (input frequency - output firing frequency) correspondence with input frequency

at the first peak, 2-1 correspondence with input frequency at the second peak and 3-1 correspondence at the third peak. And then three peak-frequencies are seen at A_{in} = 0.2 and 0.3. However, the signal gain decreases with increasing A_{in}. This imposed that the signal gain is not proportional to the strength of sinusoidal input currents. As seen in Figure 3.7B and Figure 3.8B, SC receives most signal when it receives weak sinusoidal input currents.

From this section, we understand the effect of A_{in} on both average firing rate and signal gain: (1) The maximal firing rate depends on the amplitude of sinusoidal current inputs and (2) this SC model is best responded to small amplitude of sinusoidal current where subthreshold resonance properties are communicated to supra-threshold activity of SCs. Furthermore, for A_{in} = 0.5 $\mu A/cm^2$, the SC model exhibits four peak-frequencies in supra-threshold resonance. This implies that the SC model will show multiple peaks (more than 3 peaks) in supra-threshold resonance for higher enough value of A_{in}.

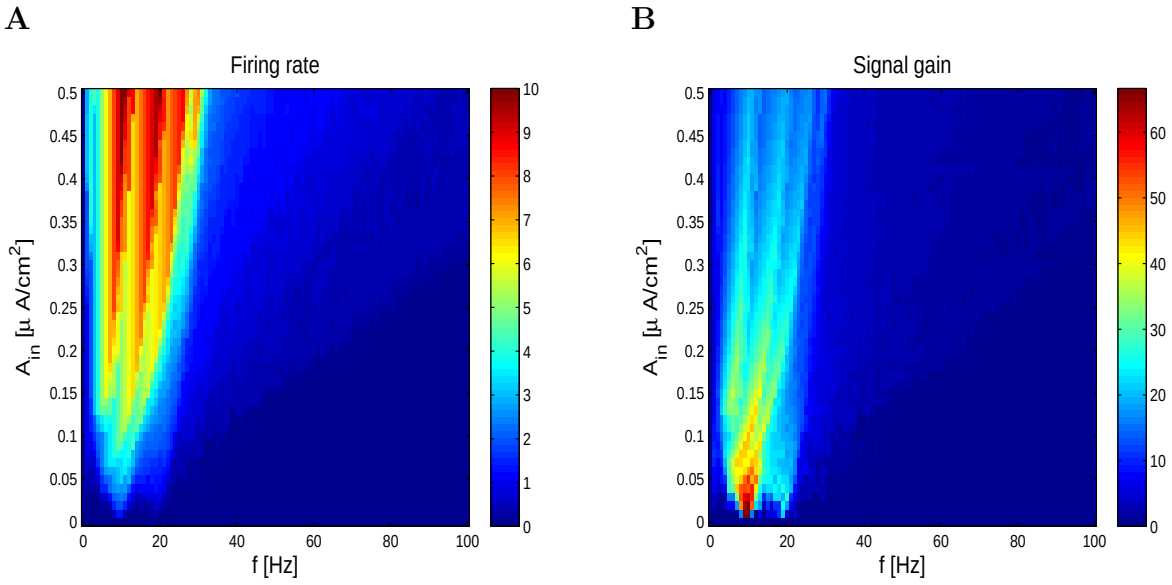

Figure 3.7 Firing rate and signal gain images with systemically increasing A_{in} using the 3D SC model (horizontal-direction is input frequency and vertical-direction is the amplitude of sinusoidal input currents, A_{in}). A shows image of average firing rate. The colorbar indicates firing rate. For small value of A_{in}, a single peak is seen at 10 Hz while multiple peaks are exhibited and shifted to higher frequency for large value of A_{in}. B shows the image of signal gain. For large value of A_{in}, SCs get less signal gain compared to lower one.

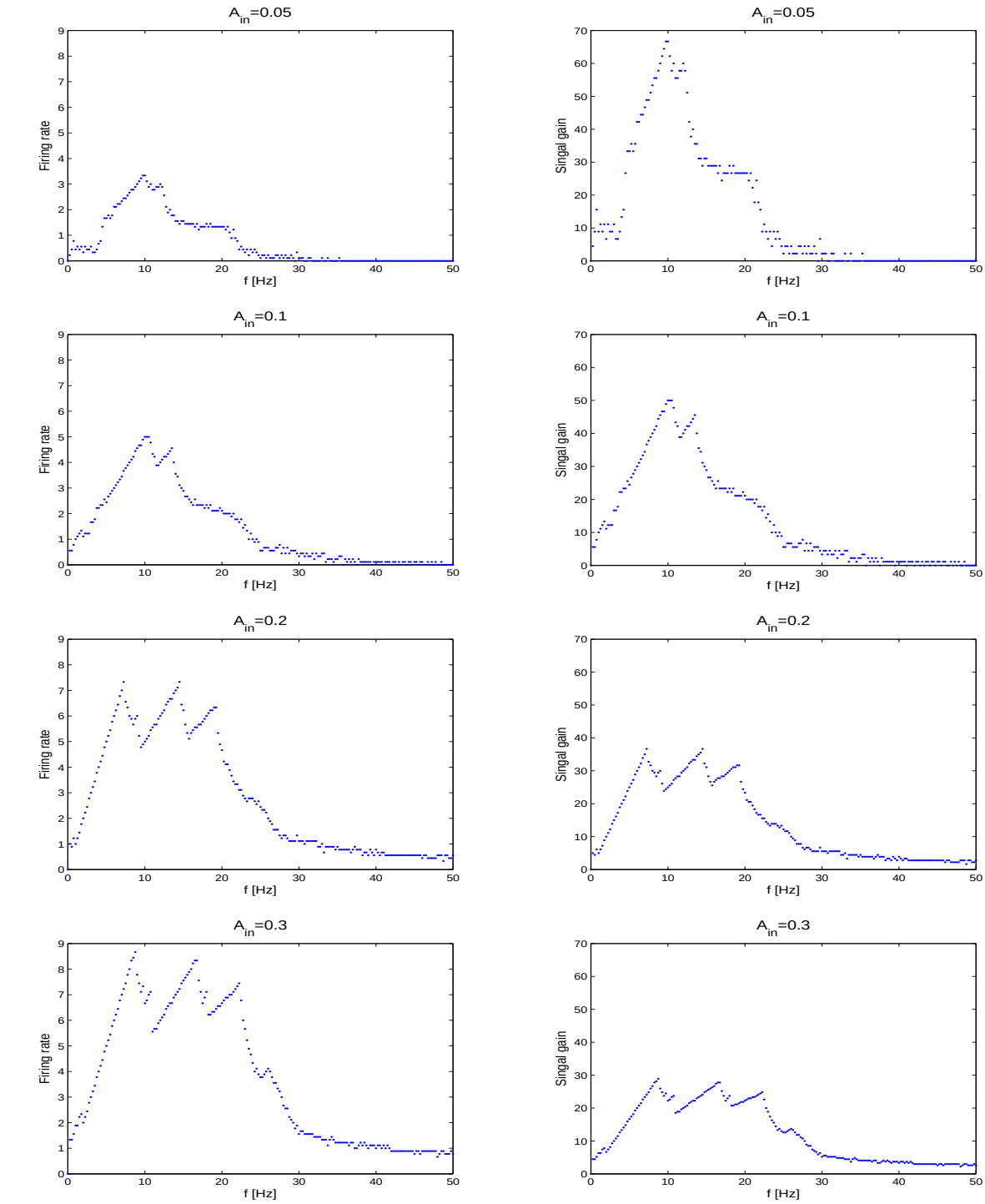

Figure 3.8 Cutoff of the images in Figure 3.7. Firing rate (A) and signal gain (B) for various A_{in}. Increasing A_{in} induces different results in both firing rate and signal gain: increasing A_{in} results in increasing firing rate but decreasing signal gain.

3.4.4 The effect of G_h and G_p

The subthreshold oscillations in SCs are generated by the interaction between a persistent sodium current (I_p) and a hyperpolarized activated h-current (I_h) [7, 11]. In this section, we investigate how both currents affect firing frequency preference in SCs by changing the maximal conductance both currents. In the simulations, we changed the maximal conductance G_p and G_h for I_p and I_h respectively and then adapted I_{app} to bring the mean value of voltage to near threshold. And then we plotted peak-frequency in terms of G_h and G_p (Figure 3.9A and 3.10A respectively). Here, we used small-amplitude sinusoidal input currents ($A_{in} = 0.05\ \mu A/cm^2$) at which the supra-threshold resonance properties are communicated with the subthreshold resonance properties. We have checked that the peak-frequencies (multiple peaks) do not change for higher value of A_{in} (data not shown).

As G_h increases, the peak-frequency does not change until $G_h = 1.55$ but is starts decreasing slightly after that value of G_h (Figure 3.9). This implies that cell's firing frequency preference can be affected by G_h or the activation of I_h. However, G_p shows oppose result. As G_p increases, the peak-frequency "almost" does not changes until $G_h = 0.58$ but it starts increasing after that value of G_h (Figure 3.10).

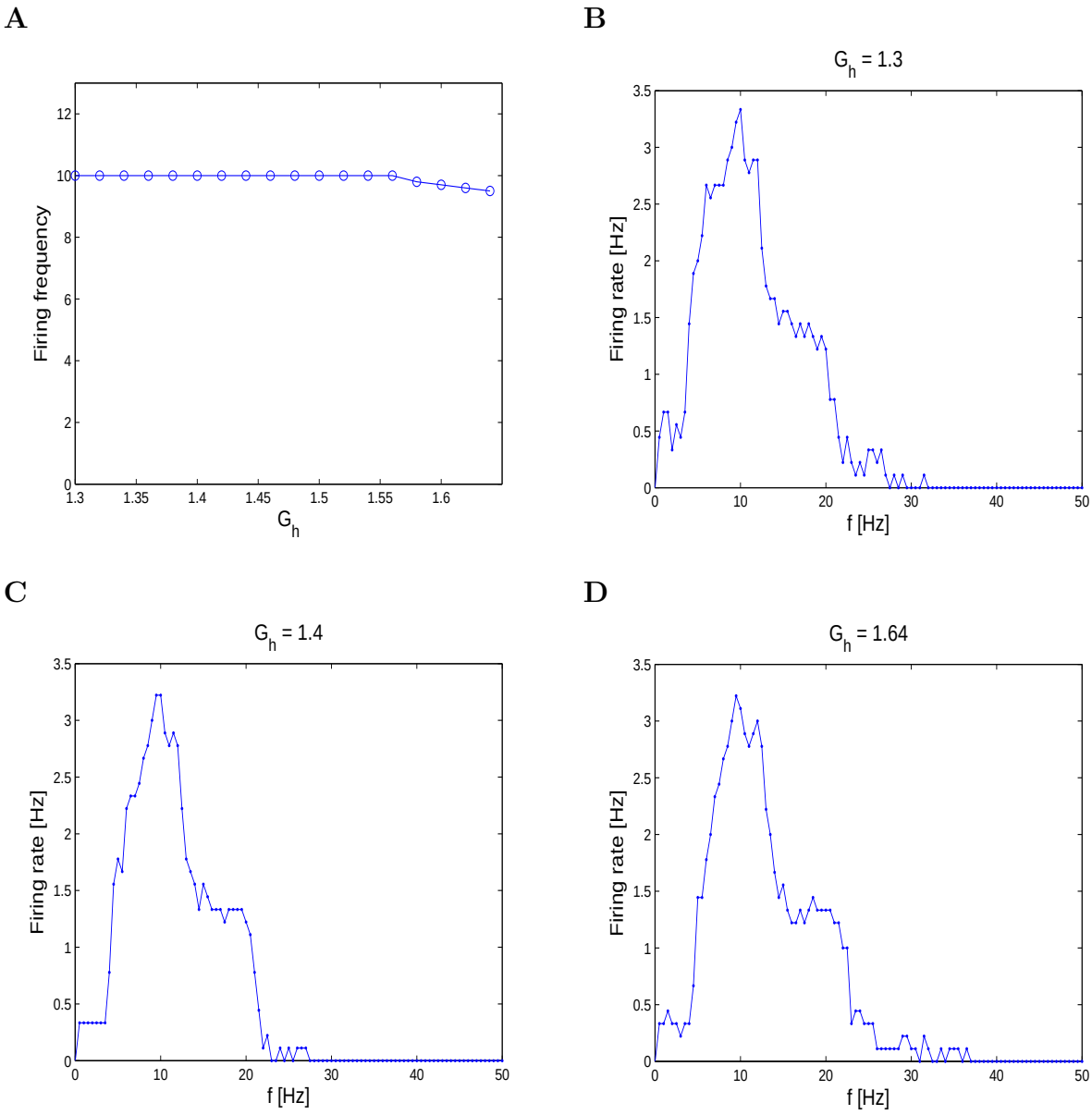

Figure 3.9 3D SC model, $G_p = 0.5$ and $A_{in} = 0.05\ \mu A/cm^2$. A: peak-frequency in terms of G_h. B, C and D are the firing frequency curve as a function of input frequency ($G_h = 1.3$, 1.4 and 1.64).

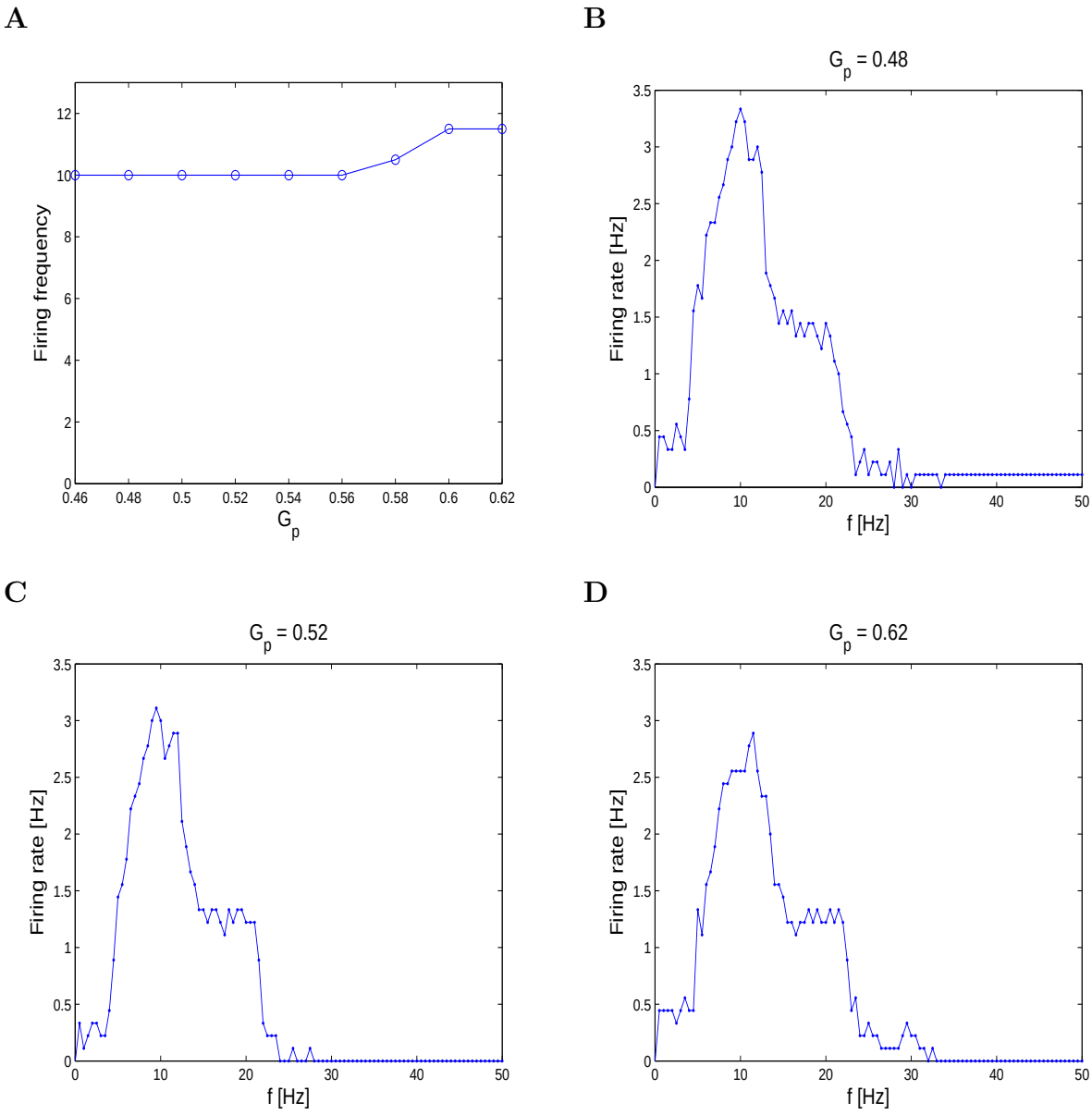

Figure 3.10 3D SC model, $G_h = 1.5$ and $A_{in} = 0.05\ \mu A/cm^2$. A: peak-frequency in terms of G_p. B, C and D are the firing frequency curve as a function of input frequency ($G_p = 0.48$, 0.52 and 0.62 respectively).

3.5 The effect of conductance-based input on frequency preference of stellate cell with 3D model

In Section 3.4, we investigated the firing frequency preference properties of neurons receiving sinusoidal current inputs. It has been suggested that these play a predictive role in the oscillatory properties of networks in which these neurons are embedded [18, 19]. However, synaptically connected neurons receive conductance rather than current inputs. Therefore, we investigate the firing frequency preference properties of neurons receiving conductance-based oscillatory inputs. One of our main findings is a prominent peak in the firing frequency response to oscillatory conductance-based inputs at high frequencies which is not observed for current-based inputs.

3.5.1 Excitatory conductance input induces hyper-excitability in the firing frequency

It has been argued that SCs have intrinsic subthreshold oscillations and firing frequency in theta frequency band [17]. And recent experiment and modeling studies show that SCs have intrinsic dynamic properties that endow them with ability to display hyper-excitability above some threshold value in the presence of recurrent excitation [39]. In this section, we study the effect of oscillatory conductance input on the firing frequency properties of SC. Here, we look at excitatory case. We add synaptic terms (equation 3.2) to equation 2.5. The current-balance equation for conductance-based input is given by

$$C\frac{dV}{dt} = I_{app} - G_p p_\infty(V)(V - E_{Na}) - I_L - I_h - I_{syn} \tag{3.7}$$

where

$$I_{syn}(t) = G_{e,in}\frac{1}{2}(1 + \sin(\omega t))(V - E_e) \quad with \quad \omega = \frac{2\pi f}{1000} \tag{3.8}$$

we used the excitatory reversal potential, $E_e = 0\ mV$ and varied the maximal synaptic conductance, $G_{e,in}$.

Figure 3.11 shows firing frequency of SC in terms of input frequency when SC receives excitatory synaptic input. Figure 3.11(A) left panel shows average firing rate density curve in terms of f for $G_{e,in} = 0.02$ and right panel is signal gain density curve. SC shows multiple peaks in supra-threshold resonance and prominent peak is in theta frequency band. Figure 3.11(B) left panel is the firing rate density and right panel shows signal gain density curve for $G_{e,in}$=0.1. For this maximal synaptic conductance, prominent peak in both firing rate and signal gain is in gamma frequency band. Note that when the maximal synaptic conductance increases, the firing frequency increase but signal gain does not "almost" change at the prominent peak.

In order to study how the maximal synaptic conductance ($G_{e,in}$) affects on SC's firing frequency preference, we increased $G_{e,in}$ systemically and measured both firing rate and signal gain with respect to input frequency f. Figure 3.12 shows the images of firing rate and signal (horizontal-axis indicates input frequency and vertical-axis is the maximal synaptic conductance, $G_{e,in}$) when SC receives excitatory synaptic input. The colorbar indicates average firing rate (figure 3.12A) and signal gain (figure 3.12B). The image of firing rate only shows there are multiple peaks in supra-threshold resonance but the image of signal gain tells us how the prominent frequency evolved by increasing the maximal synaptic conductance values. As seen in Figure 3.11, the signal gain at the prominent peak does not change but the prominent peak is gradually shifted from theta frequency band to gamma frequency band. This result is consistent to previous study [39] and shows that SCs have intrinsic properties that endow them to display hyper-excitability in the presence of excitatory conductance-based input.

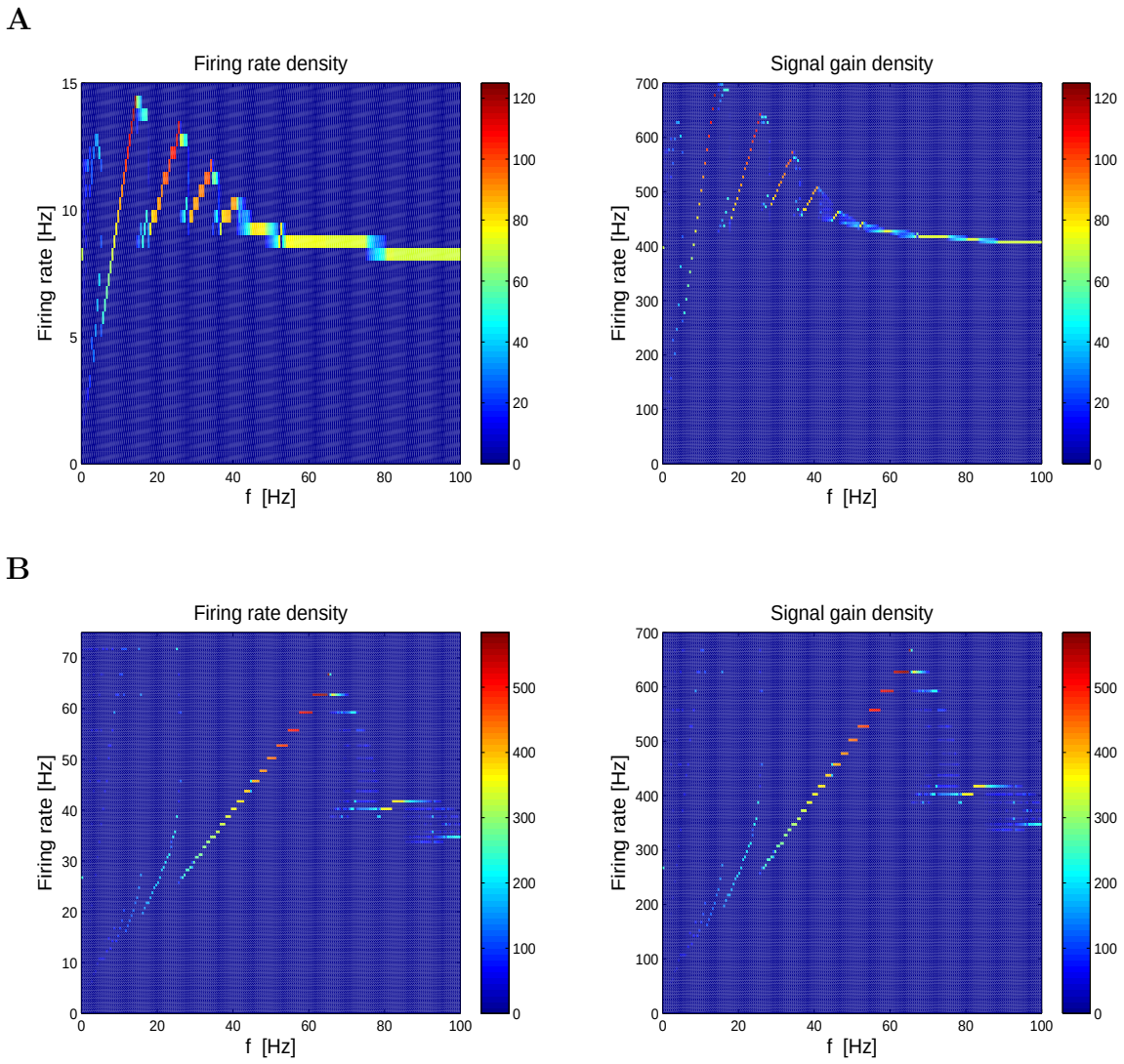

Figure 3.11 Firing frequency properties of SC which receives excitatory synaptic input using the 3D SC model. (A) left panel shows the firing rate density curve in terms of f with $G_{e,in} = 0.02$ and right panel is signal gain. SC shows multiple peaks but prominent peak is in theta frequency band. (B) left panel is the firing rate density curve and right panel shows signal gain in terms of f with $G_{e,in}$=0.1. For this maximal synaptic conductance, prominent peak in both firing rate and signal gain is in gamma frequency band. Note that when the maximal synaptic conductance increases, average firing rate increase but signal gain does not "almost" change at prominent peak.

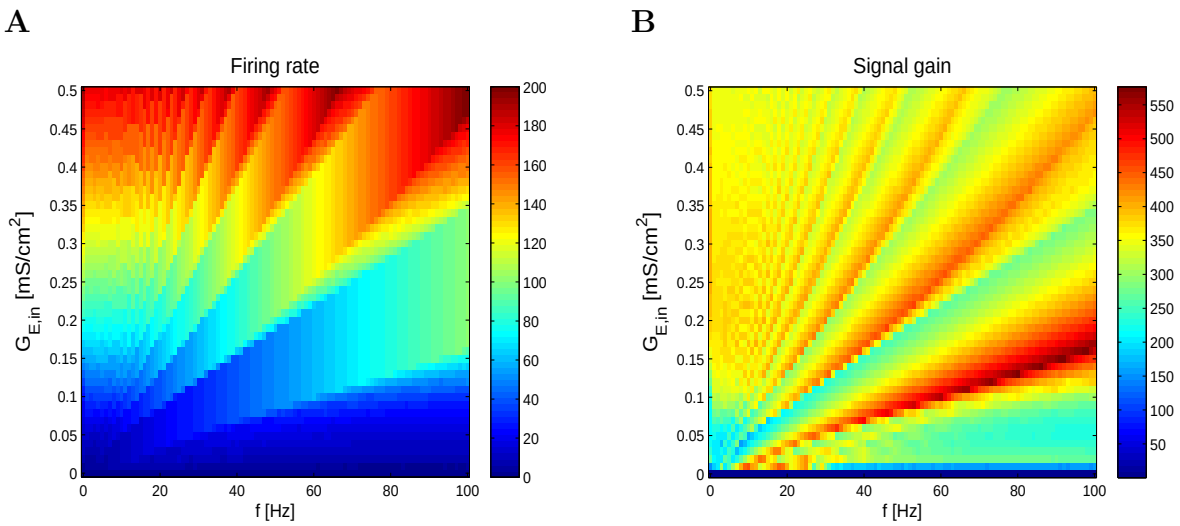

Figure 3.12 The effect of excitatory synaptic conductance on SC's firing frequency preference withI_{app} = -2.6 $\mu A/cm^2$. Figure (A) and (B) are the images of firing rate and signal gain, respectively: x-axis indicates input frequency f and y-axis is the maximal synaptic conductance, $G_{e,in}$. Color bar indicates average firing rate (A) and signal gain (B). Note that hyper-excitability is easily observed in signal gain. When $G_{e,in}$ increases, the prominent peak is shifted to high frequency.

3.5.2 SC exhibits multiple peaks in firing frequency preference when SC receives inhibitory conductance-based input

Here, we study the effect of inhibitory synaptic on SC's firing frequency preference. We use inhibitory conductance-based input such as:

$$I_{syn}(t) = G_{e,in}\frac{1}{2}(1+\sin(\omega t))(V - E_i) \quad with \quad \omega = \frac{2\pi f}{1000} \tag{3.9}$$

where the reversal potential, E_i = -75 mV and the maximal synaptic conductance, $G_{i,in}$ is non negative constant.

Figure 3.13 shows the firing rate density with various $G_{i,in}$. We have checked that for $G_{i,in} = 0.001$, supra-threshold resonance frequency is near subthreshold resonance frequency and increasing the value of $G_{i,in}$ induces multiple peaks in supra-threshold resonance. These results are similar to the effect of current-based input case: three frequencies preference are shown in supra-threshold resonance. However the corresponding firing rate at the second peak is getting less than the firing rate at the first one with increasing $G_{i,in}$ and small increasing $G_{i,in}$ induces abrupt increase in firing frequency of SC. The difference between current- and inhibitory conductance-based inputs is the firing rate of corresponding voltage traces at each peak in firing rate density. The firing rate at the first peak-frequency is getting a prominent peak comparing to the others. For $G_{i,in} = 0.05$, corresponding firing rates at the first and second peaks are "almost" same. However, for $G_{i.in} = 0.1$ or higher value, the firing rate at the first peak-frequency becomes a prominent peak and the firing rates at the second and third peak-frequencies are getting less than the first one.

Figure 3.14 shows the image of firing rate and signal gain with various $G_{i,in}$. The horizontal- and vertical-direction indicate input frequency f and the maximal synaptic conductance $G_{i,in}$, respectively. The colorbar indicates firing rate and signal gain. These numerical results show that SC exhibits multiple firing frequencies preference in

supra-threshold regime. For small value of $G_{i,in}$, supra-threshold resonance frequency is near subthreshold resonance frequency but SC shows multiple firing frequencies preference with small increasing $G_{i,in}$. Small change of $G_{i,in}$ induces abrupt change in the existence of peak-frequency. These results are similar to current-based input case. Another similarity is shown in figure 3.14B. SC receives most signal at low level of $G_{i,in}$. For higher value of $G_{i,in}$, SC get less signal gain compared to lower one.

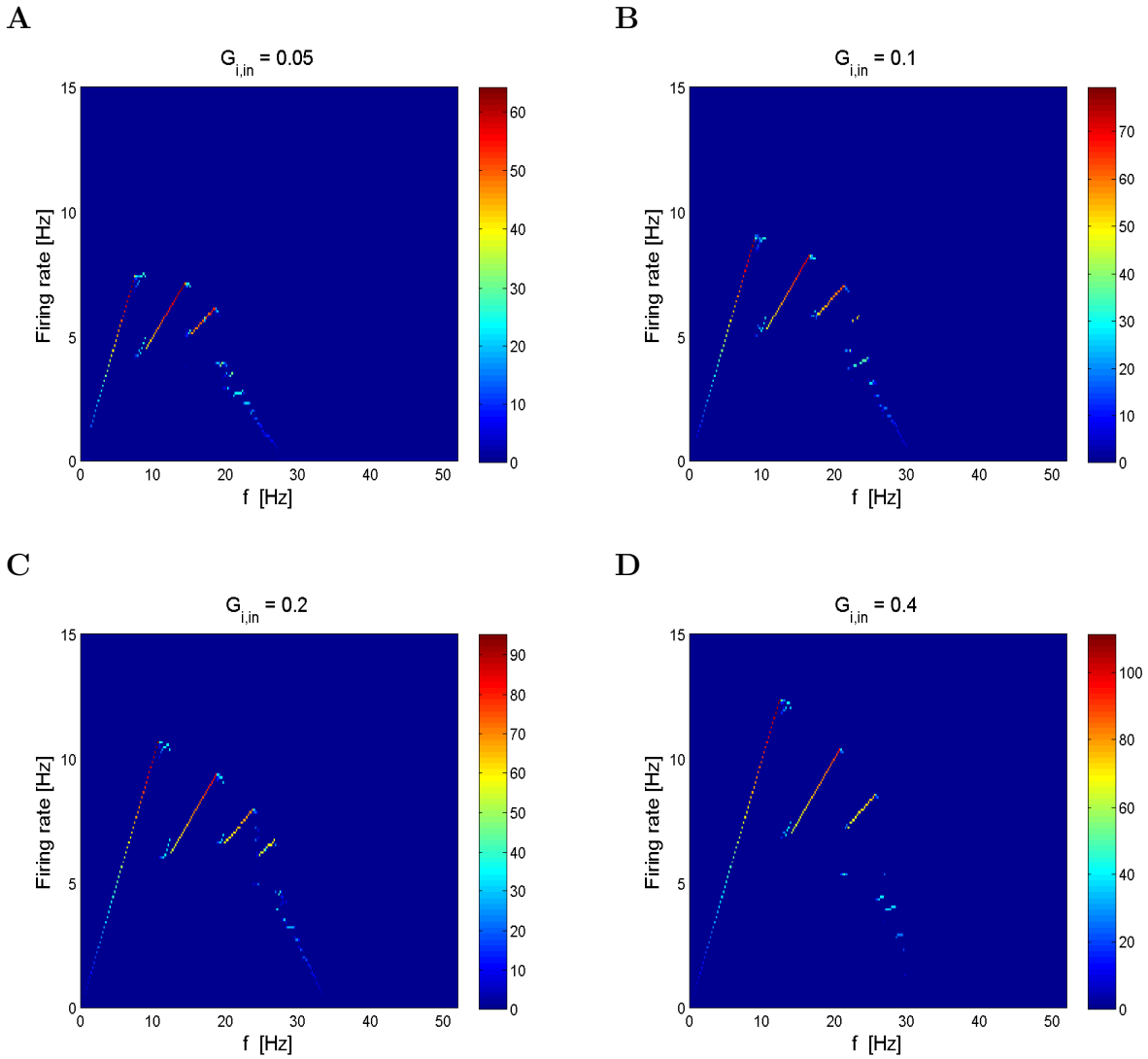

Figure 3.13 The effect of inhibitory conductance input on SC's firing frequency properties using 3D SC model with various maximal synaptic conductance (A,B,C,D are for $G_{i,in} = 0.05$, 0.1, 0.2 and 0.4 respectively). Firing rate density curve shows multiple peaks in supra-threshold resonance. These results are similar to the effect of current-based inputs at higher value of A_{in}. Small change of $G_{i,in}$ makes abrupt change of the existence of peak-frequency in supra-threshold resonance.

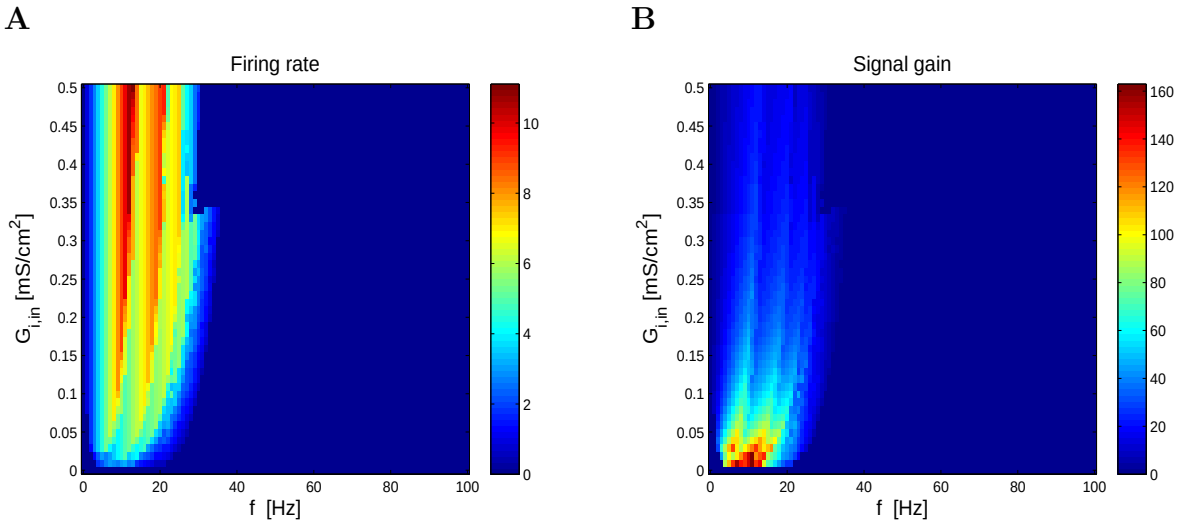

Figure 3.14 3D SC model. The effect of inhibitory synaptic on SC's firing frequency preference with I_{app} = -2.6 $\mu A/cm^2$. Figure (A) and (B) are the images of firing rate and signal gain, respectively: x-axis indicates input frequency f and y-axis is the maximal synaptic conductance, $G_{e,in}$. Color bar indicates average firing rate (A) and signal gain (B). SC exhibits multiple firing frequencies preference in supra-threshold regime. And SC receives most signal at low value of $G_{i,in}$. These results are similar to the effect of current-based input case.

3.6 The effect of current-based input on frequency preference of stellate cell with linear model

It has been argued that the simple linear model can reproduce both resonant and nonresonant subthreshold dynamics [16, 18, 25, 40] and explain the relationship between sub- and supra-threshold resonance [18, 19]. Here, we investigate sub- and supra-threshold resonance with linear version of SC model (described in chapter 2: equation 2.11–2.13). In particular, we are interested in under what condition linear model can reproduce non-linear behaviors in supra-threshold activity: supra-threshold resonance can be predicted by subthreshold resonance property with weak sinusoidal current inputs and linear model can exhibit multiple peaks in supra-threshold resonance with higher value of A_{in}.

For a minimal description of spike generation, we need to be equipped with a firing threshold and a voltage reset. Here, we introduce two parameters describing spike generation: voltage threshold V_{th} and voltage reset V_{reset}. Whenever $V(t)$ reaches V_{th} from below, a spike is generated, and $V(t)$ resets to V_{reset}. We first show that the linear SC model is not appropriate to explain supra-threshold resonance properties which observed in nonlinear model. Then we show that supra-threshold resonance properties in the linear model depends on V_{th} and V_{reset}. Note that we use artificial V reset value as V = -70 mV to see an action potential. Once the voltage reset to the artificial reset value, the voltage move to the reset value V_{reset} in next time step. And then the voltage follows the linear system (equation 2.11–2.13).

3.6.1 The firing frequency preference on supra-threshold regime of SCs

Here, we use I_{app} = -2.68 $\mu A/cm^2$ where the fixed point (V^*, r_f^*, r_s^*) is stable spiral and inject sinusoidal current inputs. Increasing amplitude (A_{in}) of sinusoidal input currents results in increasing firing rate. The linear model shows a single peak for

$A_{in} = 0.12\ \mu A/cm^2$ but this model shows different results from nonlinear model in supra-threshold resonance for higher value of A_{in}.

Figure 3.15 shows how the subthreshold resonance properties are related to supra-threshold activity of SC with various A_{in}. Figure 3.15A is the impedance curve which shows that this linear model exhibits a single peak at input frequency $f =$ 10 Hz. Here, we use $A_{in} = 0.01\ \mu A/cm^2$ and use the impedance-like function (see section 3.2.1) for impedance curve. Figure 3.15B–D are the firing rate density curve with $A_{in} = 0.12$, 0.17 and 0.3 respectively. For $A_{in} = 0.12$ (Figure 3.15B), The firing rate density curve shows a single peak at $f = 10$ Hz with firing frequency = 4.8 Hz. For A_{in} =0.17, the output firing frequency is in 1-1 correspondence with input frequency f when the output firing rate increases with respect to input frequency (Figure 3.15C). However, for higher value of A_{in} ($A_{in} = 0.3$), the linear model shows two interspike intervals at low frequencies ($f = 4$–12 Hz) and 1-1 correspondence with input frequency at higher frequency ($f = 21$).

Our results demonstrating supra-threshold properties are consistent with the results in nonlinear case for small value of A_{in}: subthreshold resonance properties are communicated to supra-threshold activity of SC. However the linearized SC model shows different results in the existence of peak-frequency in supra-threshold resonance for higher values of A_{in}. Therefore we need to understand how the linearized model differs from nonlinear model during high-amplitude of sinusoidal current inputs. In contrast to nonlinear model, the linearized model exhibits bursting at low frequencies when SC receives high-amplitude sinusoidal input currents. Figure 3.16 shows the corresponding voltage traces to sinusoidal current inputs with $A_{in} = 0.3\ \mu A/cm^2$. We plotted the sinusoidal input currents (red color) with voltage traces (blue color) on the same window to see how high-amplitude sinusoidal input currents generate bursting in voltage traces. The linear model exhibits bursting in the voltage traces at $f = 3$ –

9 Hz and regular patterns in firing frequency at $f = 10 - 12$ Hz. As f increases, the inter-burst interspike intervals decrease until the voltage trace shows regular pattern in firing frequency. From these figures, we can understand how this linear model differs from nonlinear model. This bursting at low frequency in the linear model is not observed in the nonlinear model: corresponding voltage traces show two interspike intervals not bursting in nonlinear model. We will discuss further about different mechanisms of linear and nonlinear models using phase-space analysis (in section 3.8). And we have checked that SC receives most signal at the peak-frequencies, which is in contrast to nonlinear case.

In this section, we compared supra-threshold activity of SC using the linearized model to the nonlinear case. Here, we found that there are two evidences which support that the linearized model is not appropriate to capture supra-threshold resonance properties in nonlinear model. The first evidence is that the corresponding voltage traces display bursting at low frequencies when SC receives high-amplitude sinusoidal input currents. The second evidence is that SC receives "almost" same signal at peak-frequencies when the amplitude of sinusoidal input currents increases systemically (data not shown).

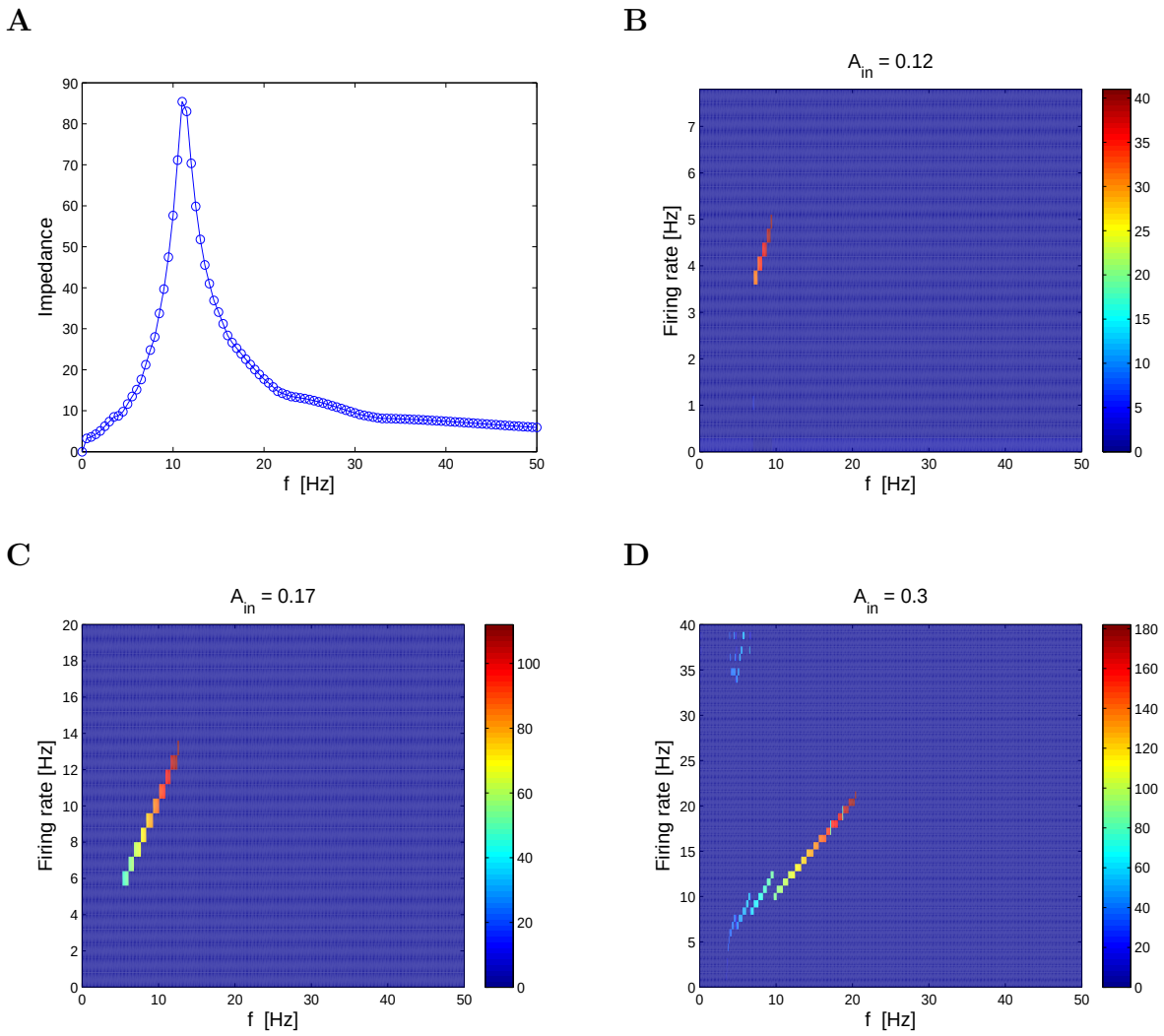

Figure 3.15 A: Impedance graphs (subthreshold resonance frequency is at 10 Hz. B, C, D : firing rate vs. f with A_{in} = 0.12, 0.17 and 0.3 respectively. We used V_{th} = -50 and V_{reset} = -56. Firing rate shows 1-1 correspondence with f for $A_{in} > 0.14$. For $A_{in} = 0.3$, the linear model displays bursting in voltage trace at low frequency.

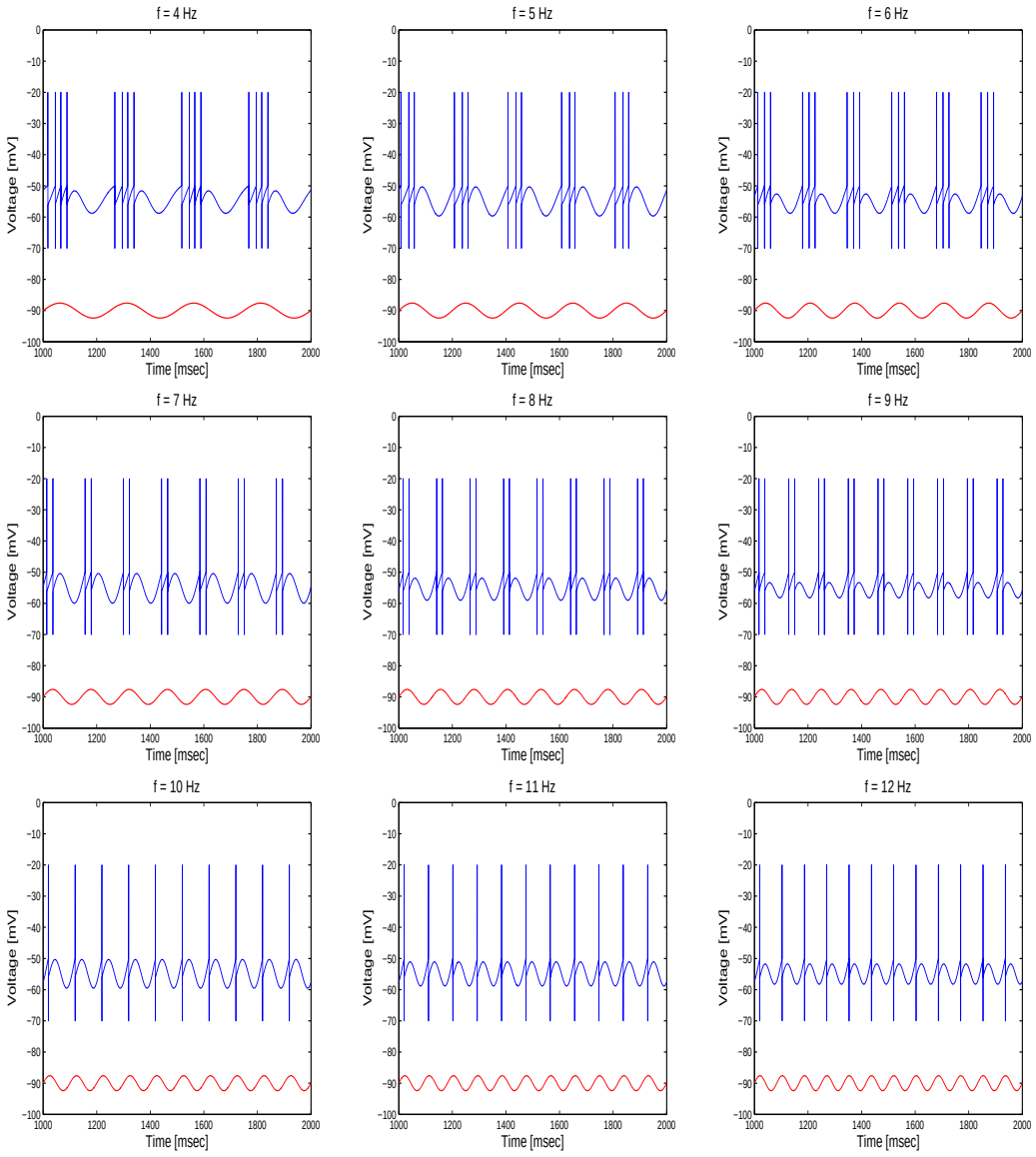

Figure 3.16 Corresponding voltage traces to sinusoidal current with various input frequency (f= 4, 5, 6, 7, 8, 9, 10 and 11 Hz) and A_{in} = 0.3 $\mu A/cm^2$ using the linear model. We use V_{th} = -50 mV and V_{reset} = -56 mV. When the linear model receives strong sinusoidal current input, it exhibits bursting at lower frequency. And then it shows regular firing pattern from f = 10 Hz. This is in contrast to the results in nonlinear model.

3.6.2 The Effect of V_{th} and V_{reset} in linear model

In this section, we investigate how V_{th} and V_{reset} value affect firing frequency in the linear model. We first fixed V_{th} = -50 mV and varied V_{reset} from -60 to -54 mV for the effect of V_{reset} on the firing frequency of SCs. And then we fixed V_{reset} and varied V_{th} for the effect of V_{th} on the firing frequency of SCs. In our simulations, we found that the effects of both V_{reset} and V_{th} on firing frequency are the same such as expanding or shrinking the voltage range of values in the subthreshold regime of SCs. Furthermore, in the numerical simulations, we found that the structure of firing frequency is changed by changing those values: increasing the voltage range of values in the subthreshold regime (increasing V_{th} or decreasing V_{reset}) results in decreasing intra-burst interspike interval. In addition, for small-amplitude sinusoidal inputs, both V_{th} and V_{reset} does not change firing frequency qualitatively.

Figure 3.17 shows how V_{reset} affects firing frequency in the linear model. Here, we use A_{in} = 0.3 $\mu A/cm^2$ and use V_{th} = -50 mV. As V_{reset} increases to positive direction, the intra-burst interspike interval decreases. This is also observed in decreasing V_{th} (data not shown). When V_{th} decreases to more negative with fixed V_{reset} value, the intra-burst interspike interval decreases. These phenomena are due to the voltage range of values in the subthreshold regime; both increasing V_{th} to positive and decreasing V_{reset} to negative direction affect increasing this voltage range. This implies that if the voltage range of values in the subthreshold regime extend, then voltage can spend more time in those regime until it reaches voltage threshold. We will discuss about the mechanism how bursting is generated and how the size of subthreshold regime affects increasing or decreasing the intra-burst interspike interval in section 3.8.

From these results, we conclude that both V_{th} and V_{reset} change the structure of firing frequency in the linear model. This suggests that supra-threshold resonance can

not be predicted by linear model since the firing frequency preference is not unique, depended on both V_{th} and V_{reset}. However, the subthreshold resonance properties are still communicated to the supra-threshold resonance in the regime of A_{in} where supra-threshold resonance frequency is near subthreshold resonance frequency.

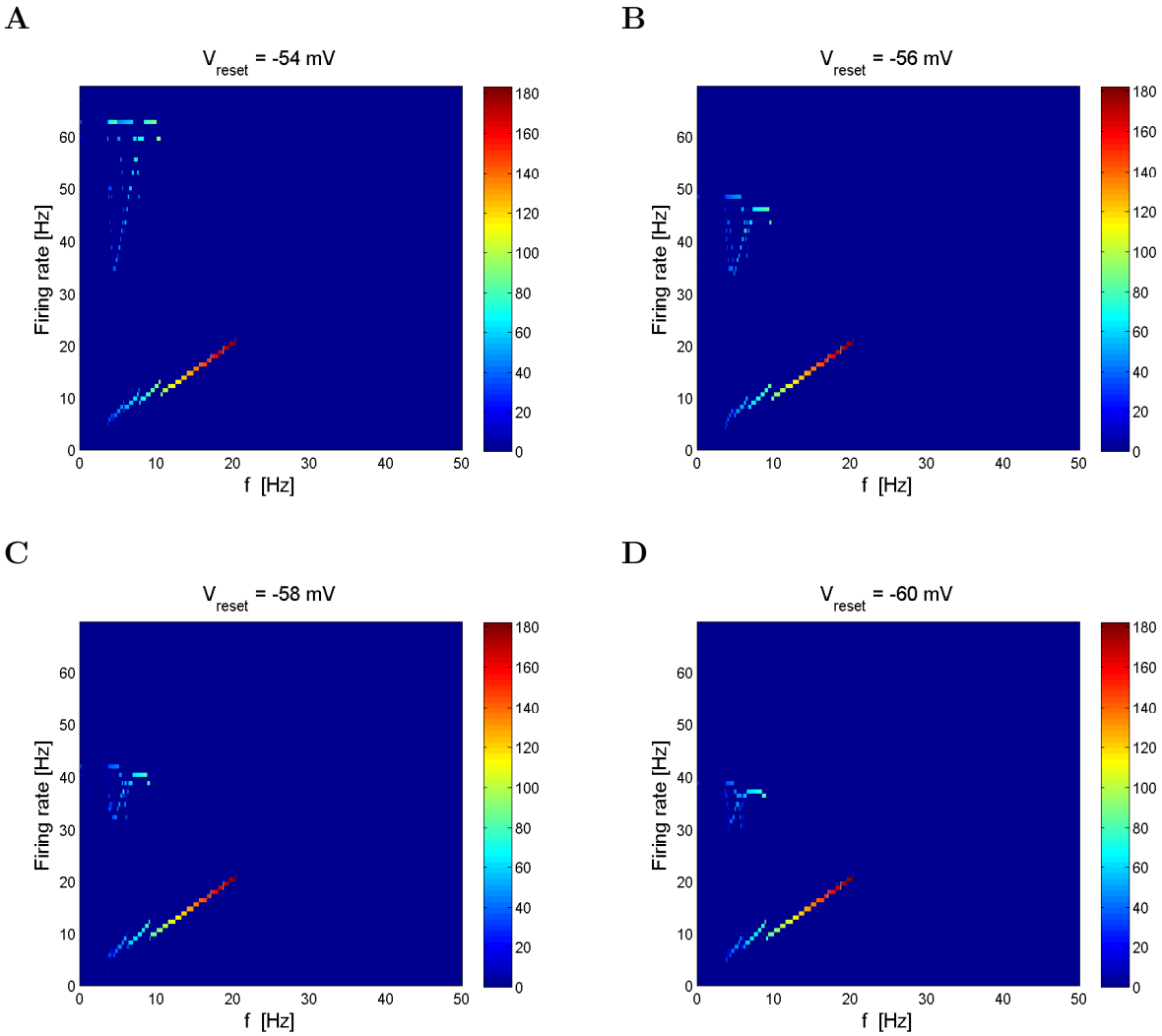

Figure 3.17 The effect of V_{reset} on firing frequency preference (fixed V_{th} = -50 mV). A, B, C, and D are the firing rate density curve with various V_{reset} and A_{in} = 0.3 $\mu A/cm^2$. Increasing V_{reset} to positive direction results in decreasing intra-burst interspike interval.

3.7 Phase-space analysis: background

A useful tool for the qualitative understanding of the dynamics of the reduced 3D SC model is phase-space analysis. In this section, we study dynamic behavior of reduced 3D SC model [11] such as the role of I_{app} current and r_s, slow component of I_h in dynamical system. Important components of the phase-space are the nullclines and trajectories. The nullclines are the result of setting the right hand side of equation (2.5)–(2.7) equal to zero. The trajectories join the point (V, r_f, r_s) for different values of t, that is, as t increases, the trajectories moves marking the evolution of the dynamical system. Since this model is three-dimensional, the nullclines are two-dimensional. The r_f and r_s nullclines are given by $r_{f,\infty}(V)$ and $r_{s,\infty}(V)$ respectively. The V-nullcline is given by

$$N(V, r_s) = \frac{I_{app} - G_L(V - E_L) - G_p p_\infty (V - E_{Na})}{G_h c_f (V - E_h)} - \frac{c_s}{c_f} r_s \tag{3.10}$$

where $c_f = 0.65$ and $c_s = 0.35$.

The system (equation 2.5 – 2.7) is fast-slow with V evolving on the fast time scale and both r_f and r_s evolving on a slow time scale. Trajectories evolve on a combination of both time scales: Fast along horizontal directions and slow on small neighborhoods of the V-nullcline.

In Figure 3.18A we show the projection of the $V-$ and r_f-nullclines onto the (V, r_f)-plane for various value of r_s. The r_f-nullcline is independent of r_s so its projection is a single curve. The V-nullcline $N(V, r_s)$ is a decreasing function of r_s for all V. We plotted three curves corresponding to representative values of r_s which increase from top to bottom. As r_s increases, the maximum of the V-nullcline decreases; i.e., the curve of knees joining the maxima of the curves $N(V, r_s)$ is a decreasing function of r_s. The fixed-points (V^*, r_f^*, r_s^*) of system are the result of the intersection of the three nullclines. For $r_s = 0$ there are two fixed-points, located

in the left and right branches of the V-nullcline respectively. Figure 3.16B is the projection of the $V-$ and r_f-nullclines onto the (V, r_f)-plane for various value of I_{app} with r_s=0. When I_{app} increases, the V-nullcline moves down (the maximum of the V-nullicline decreases). Thus the curve of knees joining the maxima of the curves is a decreasing function of I_{app}.

Figure 3.19 shows the dynamic of SC on (V, r_f)-plane for different value of r_s when I_{app} = -3.0. For $r_s = 0$, the trajectory moves fast to V-nullcline and converge to fixed point (stable node). Increasing r_s cause to move down V-nullcline. For r_s = 0.019, the trajectory first approaches to V-nullcline and spirals down to a fixed point (stable spiral). For $r_s = 0.02$, the V-nullcline moves down slightly and the fixed point is place on the knee of V-nullcline. The trajectory moves around the knee of V-nullcline and escapes the regime without spiraling. The voltage traces for each dynamical system is shown in the third row of figure 3.19. Figure 3.19 indicates the role of r_s in SCs. This, together with the arrangement of the nullcline in the three dimensional phase space, creates mixed mode oscillations. In the absence of r_s as a dynamic variable, the V and r_f nullcline intersect at a fixed point that is a stable node, stable focus or unstable focus (Figure 3.20). Thus in the noiseless case, trajectories can either converge to a fixed point (in an oscillatory fashion or not) or spike. No mixed mode oscillations are possible. The role of r_s is to serve as a bridge between both dynamic behaviors, allowing for coexistence of subthreshold oscillations and spikes [11].

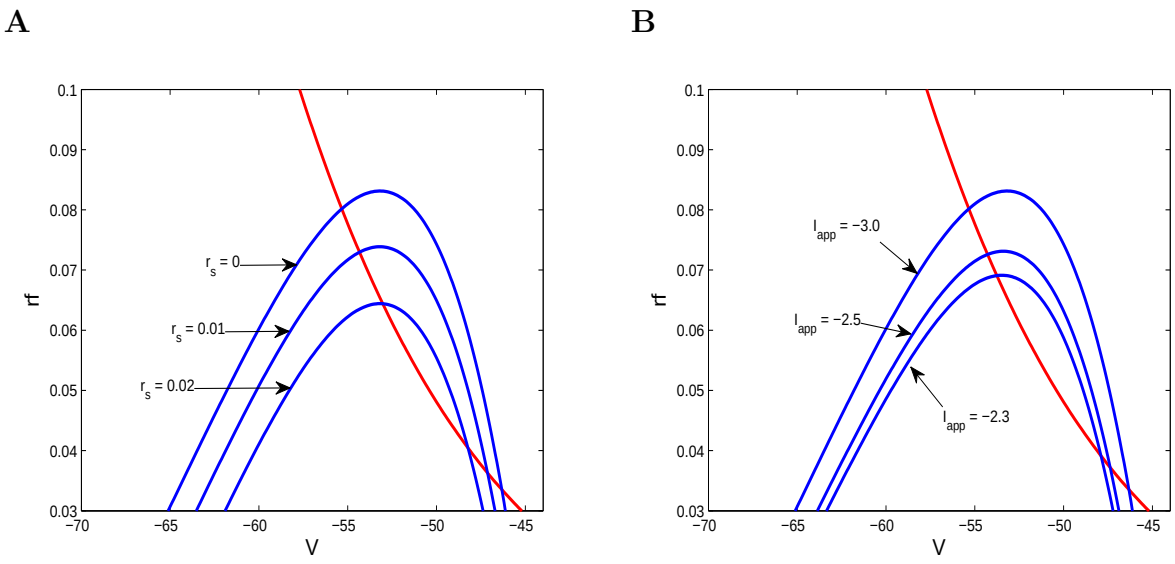

Figure 3.18 Phase-space for reduced 3D SC model. (A) is schematic diagram of the phase-space for I_{app} = -3.0. The panel show the projection of the two-dimensional V- and r_f-nullclines onto the (V, r_f)-plane. We show three representative curves corresponding to increasing values of r_s from top to bottom. These curves are the result of intersecting the V-nullcline with planes parallel to the (V, r_f)-plane for the corresponding values of r_s. (B) shows three representative curves corresponding to increasing values of I_{app} from top to bottom ($r_s = 0$). As I_{app} increases, the V-nullcline moves down similarly to the effect of resulting from increasing r_s.

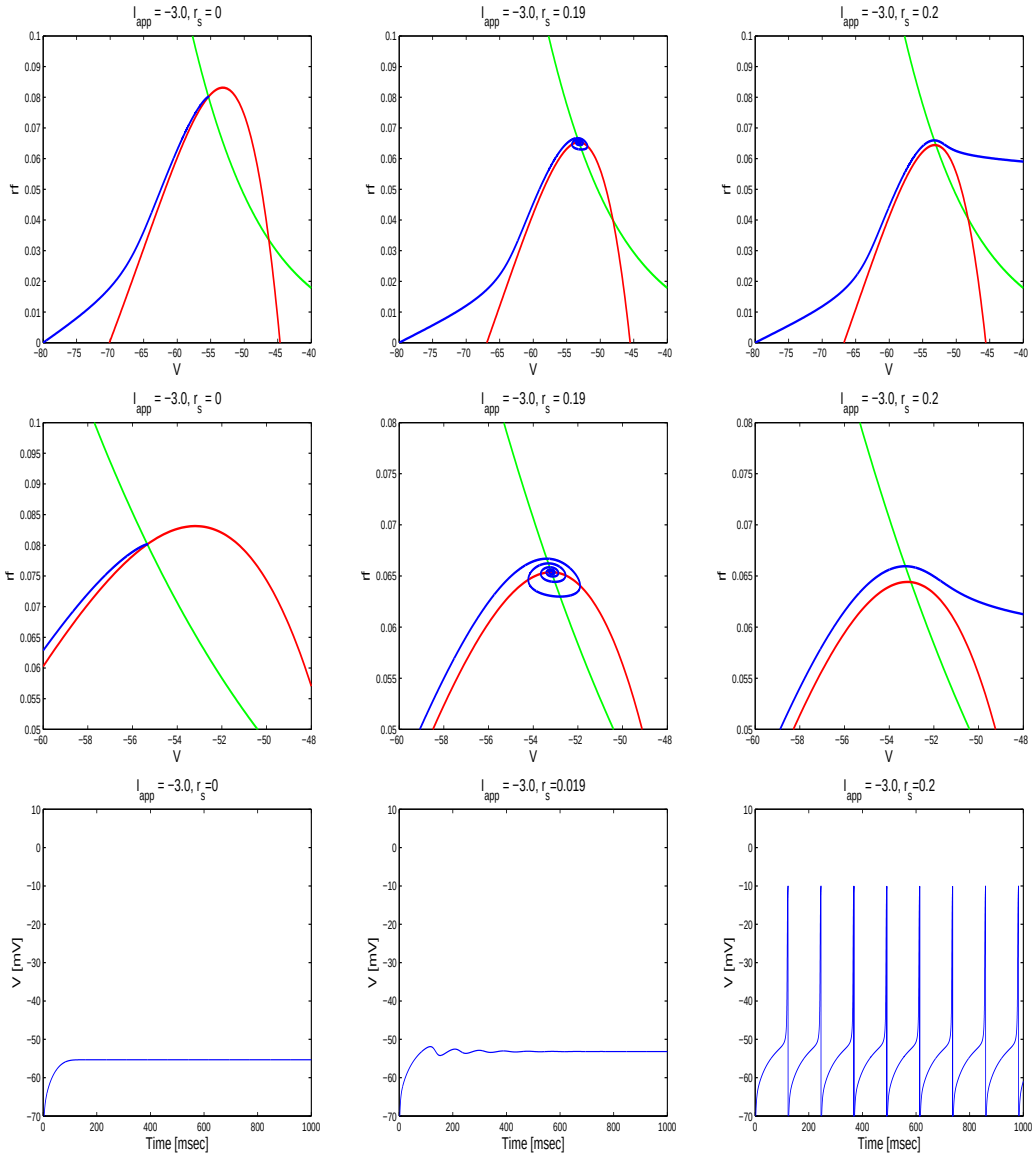

Figure 3.19 Phase-space for 3D SC model and voltage trace. Three behaviors of the system for different values of r_s. The first column shows trajectory approaches to stable node fixed point where SC is silent, that is, voltage trace shows non-oscillations. The second column illustrates that trajectory move to V-nullcline and approaches to fixed point with spiraling. The fixed point in this case is stable spiral. The third column explains the dynamics of SC when SC shows action potentials. The dynamics moves around to the knee of V-nullcline and then escape the regime without spiraling.

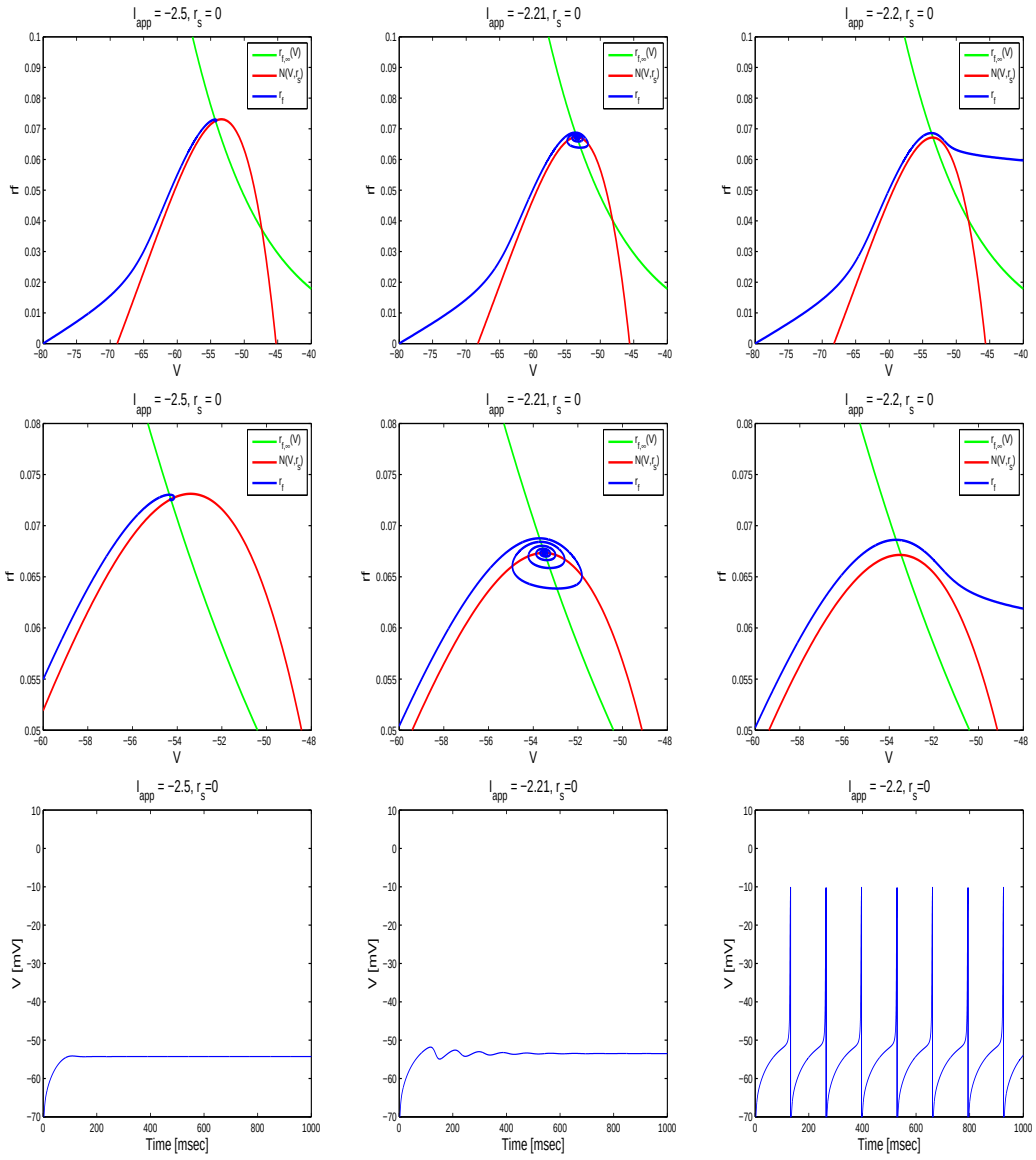

Figure 3.20 Phase-space for 2D SC model ($r_s = 0$). Three behaviors of the system for different values of I_{app}. In all three case, we consider trajectories that first approach the V-nullcline and then stay close to it, moving slowly (First column). Second column shows the trajectories first approaches to V-nullcline and spirals down to to a fixed point. The third column illustrates the trajectory moves around the knee of the V-nullcline and escapes the regime without spiraling. Note that the second row is the magnification of the first row and the third row is the voltage trace for the figures in the first row.

3.8 Dynamics mechanisms of frequency preference selection on supra-threshold activity of stellate cell

Here, we use dynamical system tools (phase space analysis) to study the mechanism of frequency preference selection in supra-threshold activity as the result of sinusoidal input currents to the reduced 3D SC model. For simplicity, we use the 2D SC model with c_f=1 and c_s=0 in equation 3.10. We first show how sinusoidal input currents change stability of fixed points in the dynamical systems. Then we show how changes to the input frequency cause changes in the SC's firing frequency (regular and irregular firing rate). Finally, we show the difference between linear and nonlinear model and how linear model displays bursting properties in supra-threshold regime when it receives high-amplitude sinusoidal input currents.

3.8.1 The structure of the phase-plane: sinusoidal current make V-nullcline moving up and down

In this section, we investigate the dynamical systems of SC with forcing term (sinusoidal input currents). The V- and r_f-nullclines for the reduced 2D SC model (c_f =1 and $c_s = 0$) with a sinusoidal current input are given by

$$N(V, r_s) = \frac{I_{app} - G_L(V - E_L) - G_p p_\infty (V - E_{Na})}{G_h(V - E_h)} + \frac{A_{in} \sin \omega t}{G_h(V - E_h)} \tag{3.11}$$

and

$$r_f(V) = r_{f,\infty}(V) \tag{3.12}$$

where

$$\omega = 2\pi f/1000$$

Equation (3.11) defines a surface parametrized by the variable t. Due to this forcing term, we can think of Equation (3.11) as a curve moving up and down as t increased.

3.8.2 Sinusoidal input currents change the stability of fixed points

Figure 3.21 shows two dimensional (V, r_f) projection of the phase-space. Time increases from A to F. The red curve is V-nullcline with sinusoidal input currents and green curve is r_f-nullcline. As t increase, the r_f-nullcline does not move but V-nullcline moves up and down. The red dot curve is the V-nullcline without sinusoidal input currents. The sinusoidal input currents ($I_n(t)$) are parametrized by time; i.e., the 2D V-nullcline changes as time evolves. More precisely, in each panel we plot the V-nullcline corresponding to $I_n(t)$ with input frequency f= 10 Hz. As time increases, sinusoidal input currents start oscillating. As a consequence of that, the V-nullcline first moves down (Figure 3.21B) and then, once $I_n(t)$ reached its maximum value and it starts decreasing, it moves back up (Figure 3.21C–F). This moving up and down of V-nullcline affects the stability of fixed points which are the intersection of V-nullcline and r_f-nullcline. Here, we use I_{app} = -2.21 $\mu A/cm^2$ where voltage traces display damped oscillations (Figure 3.20 second column). In other words, the fixed points for I_{app} = -2.21 $\mu A/cm^2$ without any forcing term are stable spiral. In Figure 3.21, if the V-nullcline (red curve) is above the V-nullcline (red dot curve, called control V-nullcline curve) without sinusoidal input currents, then the corresponding fixed points are stable node where the corresponding trajectories evolve in slow manifold and results in steady state in voltage traces (Figure 3.20 first column). However if red curve is below the control V-nullcline curve, then the corresponding fixed points are unstable where the corresponding trajectories moves along the fast direction.

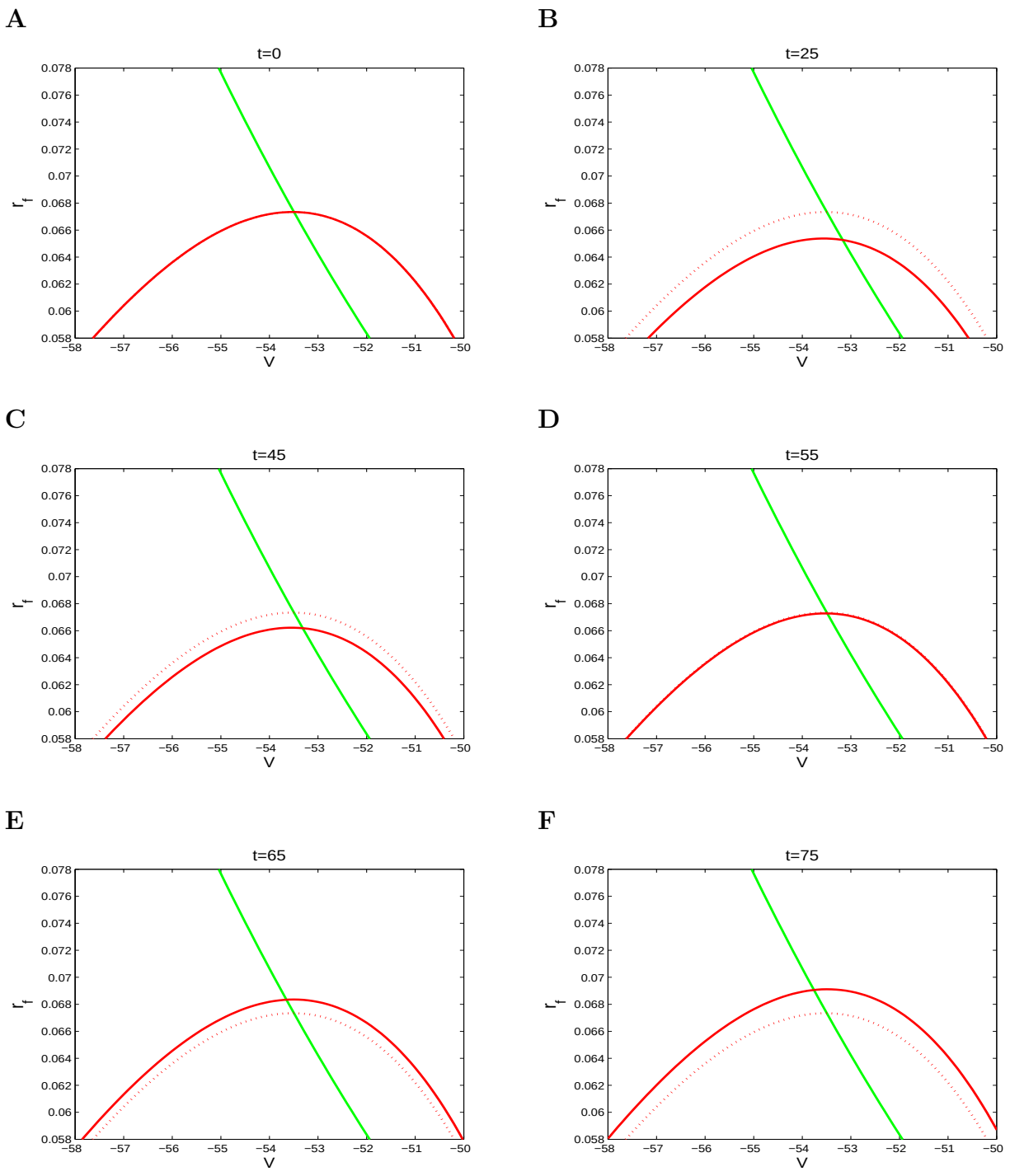

Figure 3.21 Two dimensional (V, r_f) projection of the phase-space using 2D SC model (r_s =0), Time (t) increase from A to F. As t increases, V-nullcline starts moving up and down. This movement of V-nullcline changes the stability of fixed points which are the intersection of V- and r_f-nullcline. The control V-nullcline (without sinusoidal input current) is red dot curve and V-nullcline with sinusoidal input current is red curve. r_f-nullcline does not change by increasing t and is represented by green curve.

3.8.3 The structure of the phase-plane for both regular and irregular firing rate

SC shows multiple peak-frequencies in supra-threshold resonance when it receives high-amplitude of sinusoidal input currents. In this case, we have observed that irregular firing properties of SC play an important role in the existence of multiple peak-frequencies in supra-threshold resonance. In this section, we investigate how changes to the sinusoidal input frequency cause changes in the SC's firing frequency.

Figure 3.22A shows firing rate density with respect to input frequency using 2D SC model with $A_{in} = 0.2\ \mu A/cm^2$. The multiple peak-frequencies are seen at $f = 10.5$, 20.5 and 27.5 Hz. For input frequency $f = 10.5$ Hz, the corresponding voltage traces display regular firing rate (firing frequency 10.5 Hz) (Figure 3.22B). However, for f = 13 Hz, the corresponding voltage traces show irregular firing rate (two interspike intervals). Figure 3.23A and B are the corresponding dynamics structure of phase-plane to the voltage traces in Figure 3.22B and C respectively. The trajectory is represented by blue curve. The system (3.11) – (3.12) is fast-slow with V evolving on the fast time scale and r_f evolving in a slow time scale. Trajectories evolve on a combination of both time scales: fast along horizontal directions and slow on small neighborhoods of the V-nullclines. For $f = 10.5$ Hz, only one interspike interval is shown in voltage trace. When the trajectory approaches to the subthreshold regime (-58 mV – -50 mV), the V-nullcline begins to move down and the trajectory moves fast in the direction of increasing values of V without any influence of forcing term (sinusoidal input current). As time increases, the fixed points changes from stable node to unstable in Figure 3.23A. For the detail, trajectory moves fast to fixed points (stable node) at $t = 30$ and the fixed points change to stable spiral at $t = 45$. And then the fixed points change to unstable after $t = 45$ where the trajectory moves fast horizontally and escapes the subthreshold regime, which implies that SC generates

action potentials. We have checked that when output firing rate is in one-to-one correspondence with input frequency in firing rate density graph, the trajectories move fast horizontally without influences by the forcing term (sinusoidal input currents) and voltage traces show regular firing rate. Furthermore, our numerical results show the existence of periodic solutions since there exists closed limit cycle where trajectories travels. In other words, as time increases, the trajectory moves only along this closed orbits.

For $f = 13$ Hz, two interspike intervals are shown in voltage traces (Figure 3.22C). The trajectory movement in short interspike interval is the same as the case for $f = 10.5$ Hz (regular firing rate). However, the trajectory in long interspike intervals shows different movement. If the trajectory moving almost in the horizontal direction is not fast enough as compared to the speed at which the V-nullcline moves up, then it may be caught inside it (Figure 3.23). If this occurs, then the trajectory is forced to reverse its direction (Figure 3.23 at $t = 80$ and 90 $msec$). After crossing the left branch of the V-nullcline the trajectory moves along the slow manifold (small neighborhood of the V-nullcline). As time increases, the V-nullcline moves down and the fixed points changes to unstable. Therefore the trajectory escapes the subthreshold regime firing an action potential (Figure 3.23 after $t = 100$ $msec$). Since other process in short interspike interval occur along fast directions, the cell's spiking period is determined by the time the trajectory spends in the slow manifold.

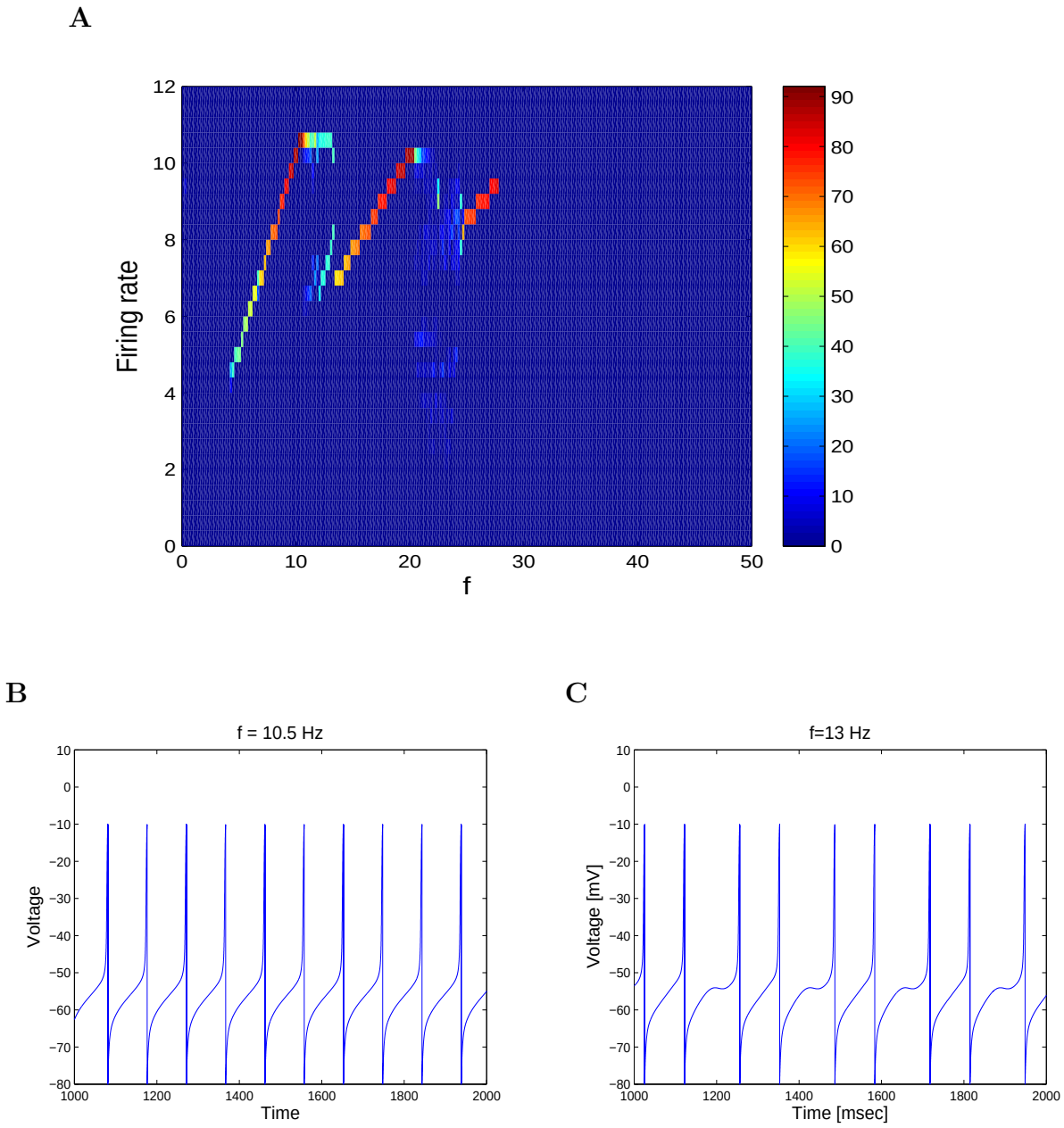

Figure 3.22 Firing rate density in terms of input frequency f with $A_{in} = 0.2$ using 2D SC model ($r_s = 0$). I_{app} = -2.21 $\mu A/cm^2$. Supra-threshold resonance frequencies are seen at $f = 10.5$, 20.5 and 27.5 Hz. B: corresponding voltage traces to sinusoidal input current f=10.5 Hz. This voltage traces show regular firing rate. C: voltage traces with $f = 13$ Hz. The voltage traces show irregular firing rate (two interspike intervals).

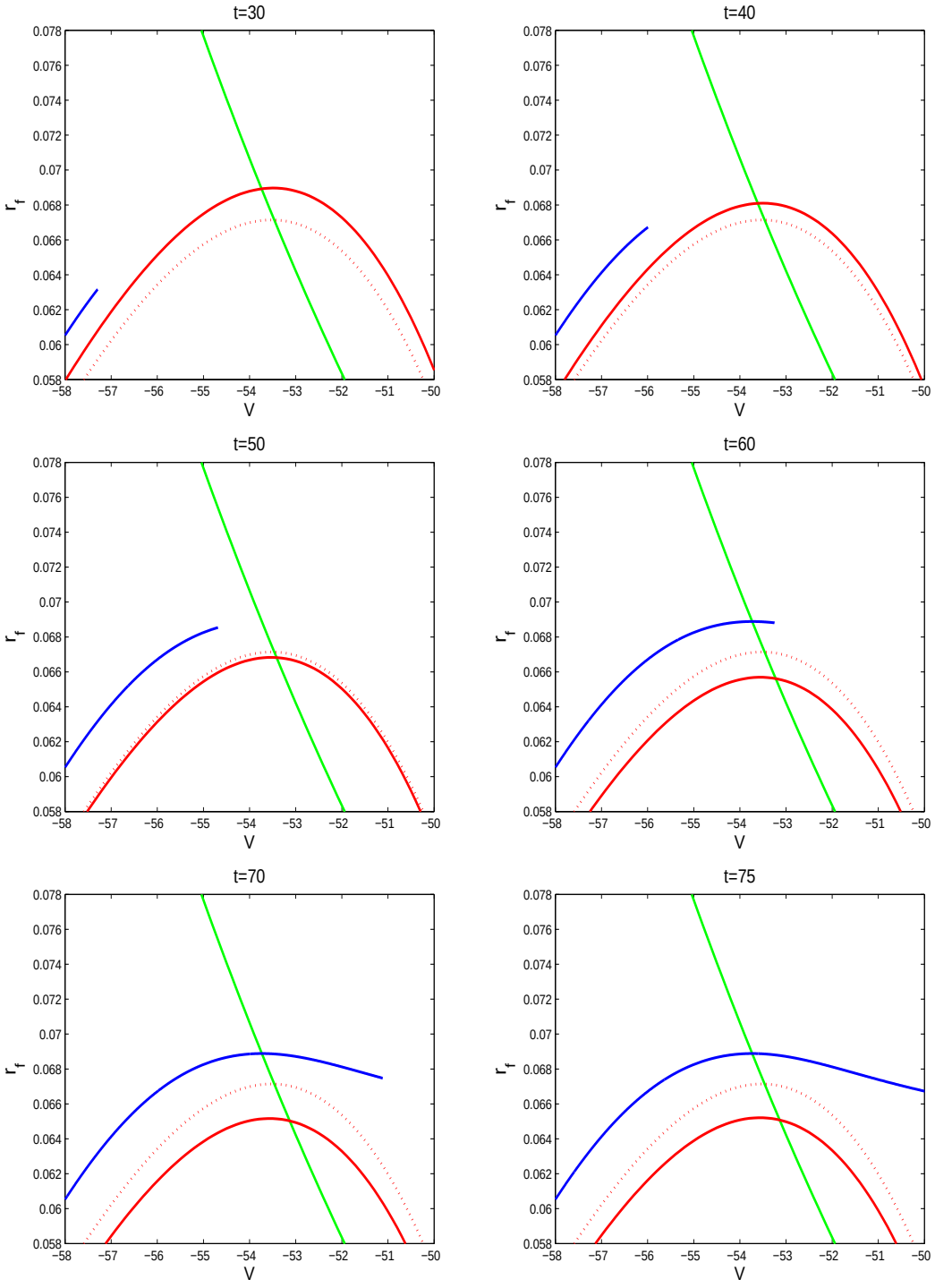

Figure 3.23 2D SC model. I_{app} = -2.21 $\mu A/cm^2$. The structure of phase-plane of voltage trace at f=10.5 Hz in figure 3.23B (with A_{in} = 0.2). The trajectory moves in time without crossing V-nullcline.

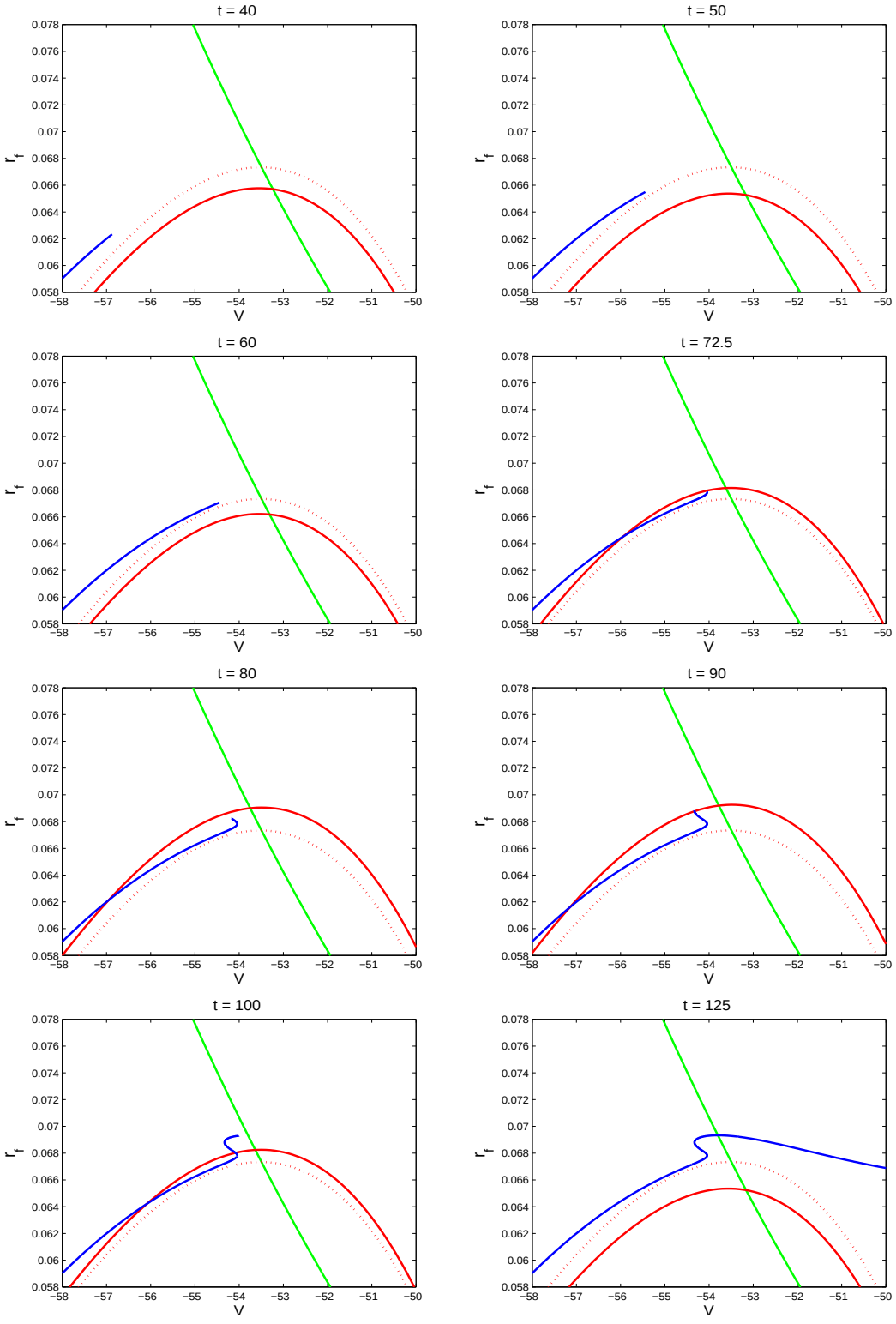

Figure 3.24 2D SC model. I_{app} = -2.21 $\mu A/cm^2$. The structure of phase-plane of voltage trace (in long interspike interval) at f=13 Hz in figure 3.23C using 2D SC model (with $A_{in} = 0.2$).

3.8.4 Preferred firing frequency depends on the reset values

In this section, we investigate the effect of r_f reset value ($r_{f,reset}$) on firing frequency using 2D SC model. Here, we choose V_{reset} = -80 mV and then change $r_{f,reset}$ to see how the changes of $r_{f,reset}$ affect preferred firing frequency in supra-threshold regime. Figure 3.25 are the firing rate density curves for various $r_{f,reset}$ values when SC receives small-amplitude sinusoidal input current ($A_{in} = 0.007\ \mu A/cm^2$). This model exhibits a single peak in firing frequency for this input current. Our numerical results show that this model shows a single preferred frequency at f = 15, 24 and 10 Hz for $r_{f,reset}$ = 0, 0.02 and 0.04 respectively. In addition, we found that the frequency preferences for various $r_{f,reset}$ values also change for high-amplitude sinusoidal input current (A_{in} = 0.07 $\mu A/cm^2$). For this case, the peak-frequencies increases as $r_{f,reset}$ increases. These numerical results show that the firing frequency preferences are dependent on the $r_{f,reset}$ value for both small- and large-amplitude of sinusoidal input currents: for small value of A_{in}, a single peak-frequency in supra-threshold regime changes irregularly by changing $r_{f,reset}$. However, for higher value of A_{in}, the peak-frequencies change regularly; i.e., these frequencies are shifted to higher frequency with increasing firing rate.

We study how the $r_{f,reset}$ value changes the firing frequency preference using phase-space analysis. Figure 3.27A, C and E are the voltage traces at peak-frequency in figure 3.25 and figure 3.27B, D and F are trajectory's movement on (V,r_f) space for figure 3.27 A, C and D respectively. As shown in the voltage traces at peak-frequency, the firing rate (interspike interval) increases (decreases) as $r_{f,reset}$ increases. When SC spikes, the trajectory moves fast to reset value and move towards the V-nullcline. For $r_{f,reset} = 0$, the trajectory start from (-80,0) and move fast towards the V-nullcline at t = 10 ms and it moves along the slow manifold (small neighborhood of the V-nullcline) at $t = 30\ ms$ (Figure 3.28). When the trajectory approaches the maxima of V-nullcline

at $t = 80\ ms$, the fixed point is stable spiral, but as time increase, the fixed point changes to unstable spiral and then it escape the subthreshold regime at $t = 130.5\ ms$. For $r_{f,reset} = 0.04$, the trajectory starts from (-80,0.04) and then move fast towards V-nullcline at $t = 5\ ms$ (Figure 3.29). When the trajectory approaches the maxima of V-nullcline at $t = 50\ ms$, the fixed point is stable spiral, but as time increases, the fixed point changes to unstable so that the trajectory escape the subthreshold regime at $t = 96.5\ ms$. Increasing $r_{f,reset}$ results in decreasing the distance which the trajectory moves from starting point (reset values) and the maxima of V-nullcline and the time the trajectory spends in the slow manifold. These results determine SC's firing frequency preferences. Thus the preferred firing frequency for different values of $r_{f,reset}$ is very different.

These geometric pictures are similar for large-amplitude sinusoidal input current (data not shown). For various values of $r_{f,reset}$, the trajectory starts from the reset values and moves fast towards V-nullcline. When the trajectory approaches the subthreshold regime, V-nullcine moves down and the trajectory moves in fast horizontal direction so that it escape fast the subthreshold regime.

Taken together, these results explain the dynamic mechanism to different peak-frequency in firing frequency for different values of $r_{f,reset}$.

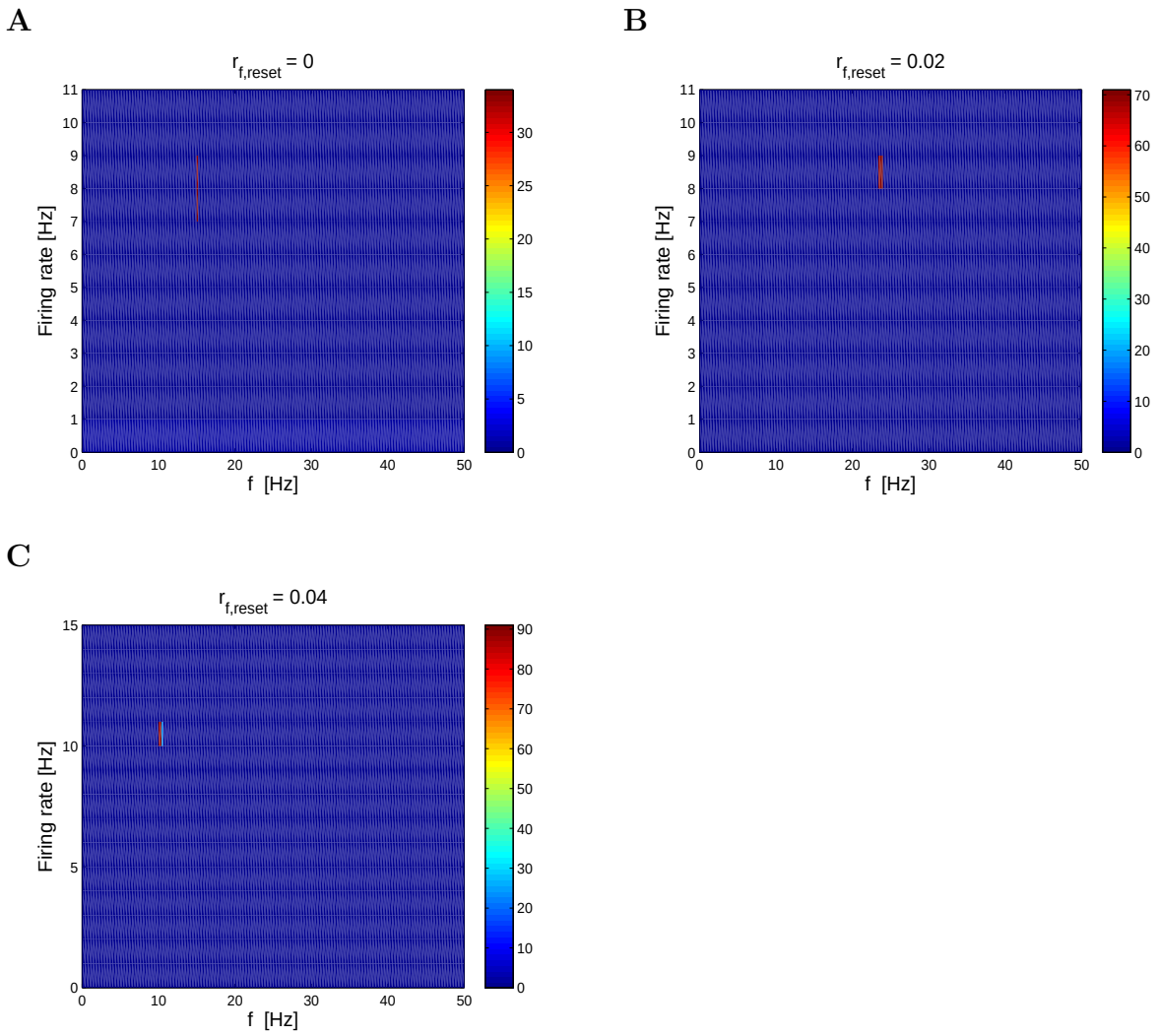

Figure 3.25 2D SC model. $A_{in} = 0.007\ \mu A/cm^2$ with various values of $r_{f,reset}$. A, B and C are firing rate density curves with $r_{f,reset} = 0$, 0.02 and 0.04 respectively.

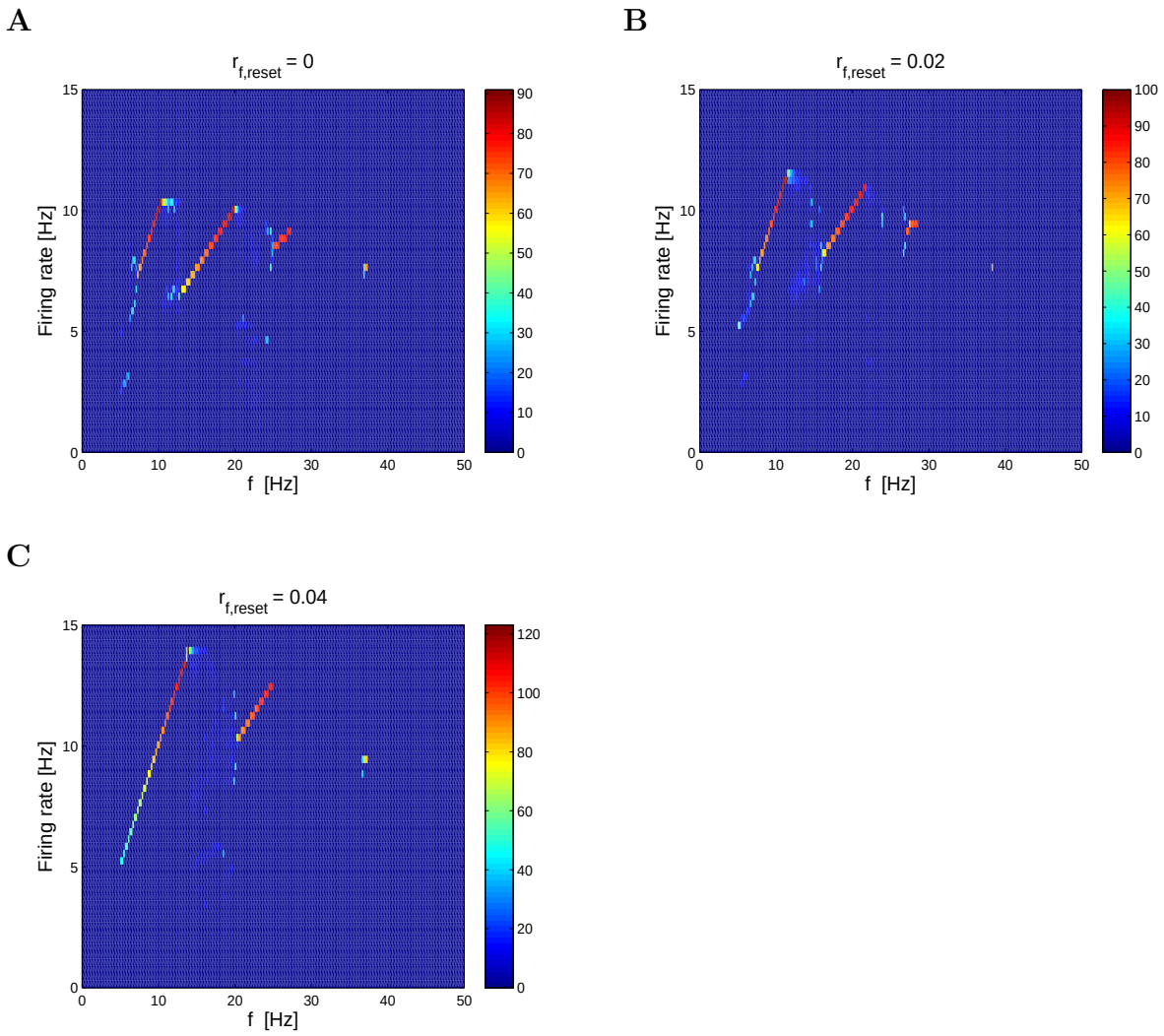

Figure 3.26 2D SC model. $A_{in} = 0.07\ \mu A/cm^2$ with various values of $r_{f,reset}$. A, B and C are firing rate density curves with $r_{f,reset} = 0$, 0.02 and 0.04 respectively.

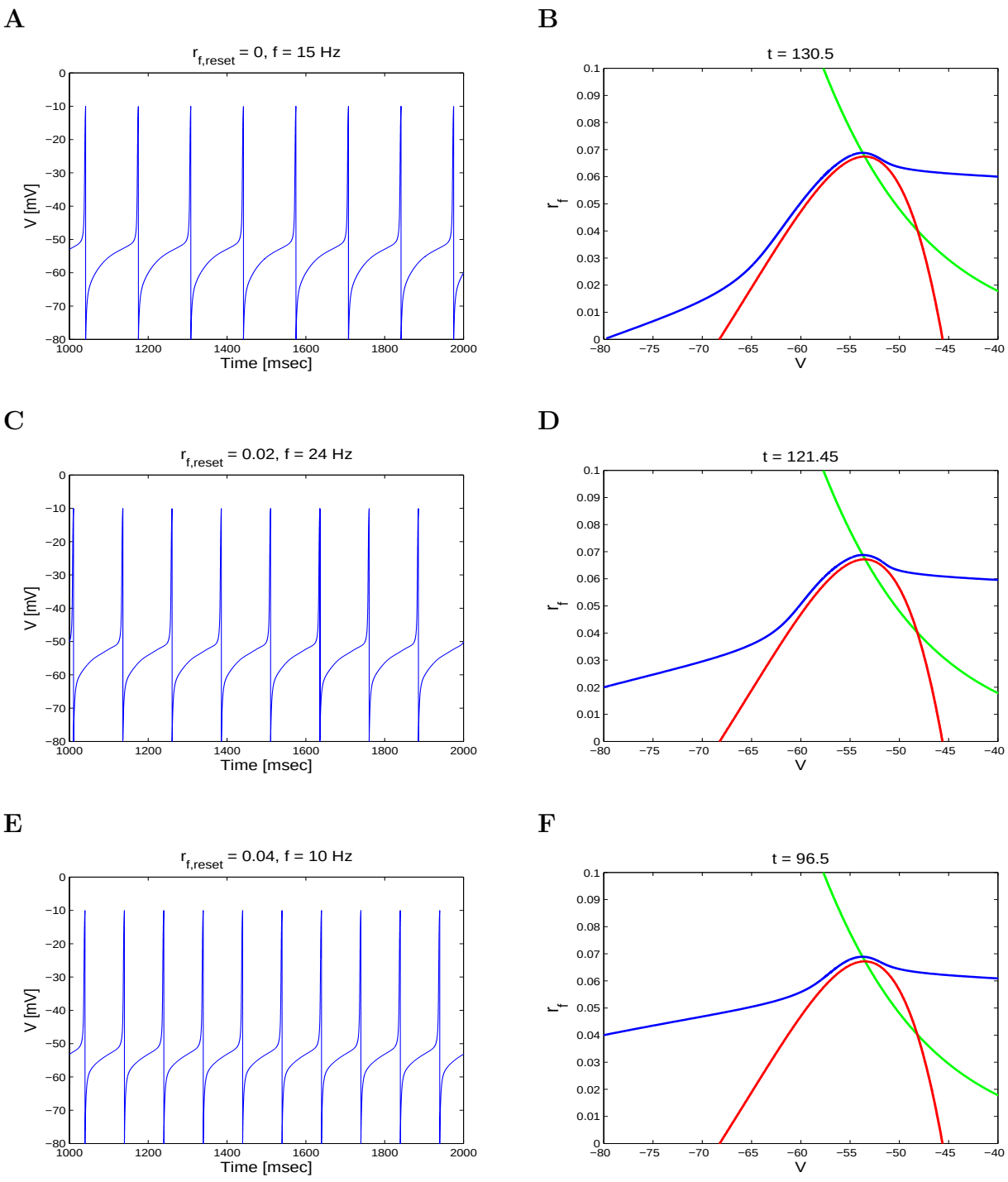

Figure 3.27 2D SC model. $A_{in} = 0.007\ \mu A/cm^2$ with various values of $r_{f,reset}$. A, C and E are the voltage traces at the peak-frequency in figure 3.25 with $r_{f,reset} =$ 0, 0.02 and 0.04 respectively. B, D and F are dynamic two-dimensional phase-space representation for A, C and E respectively.

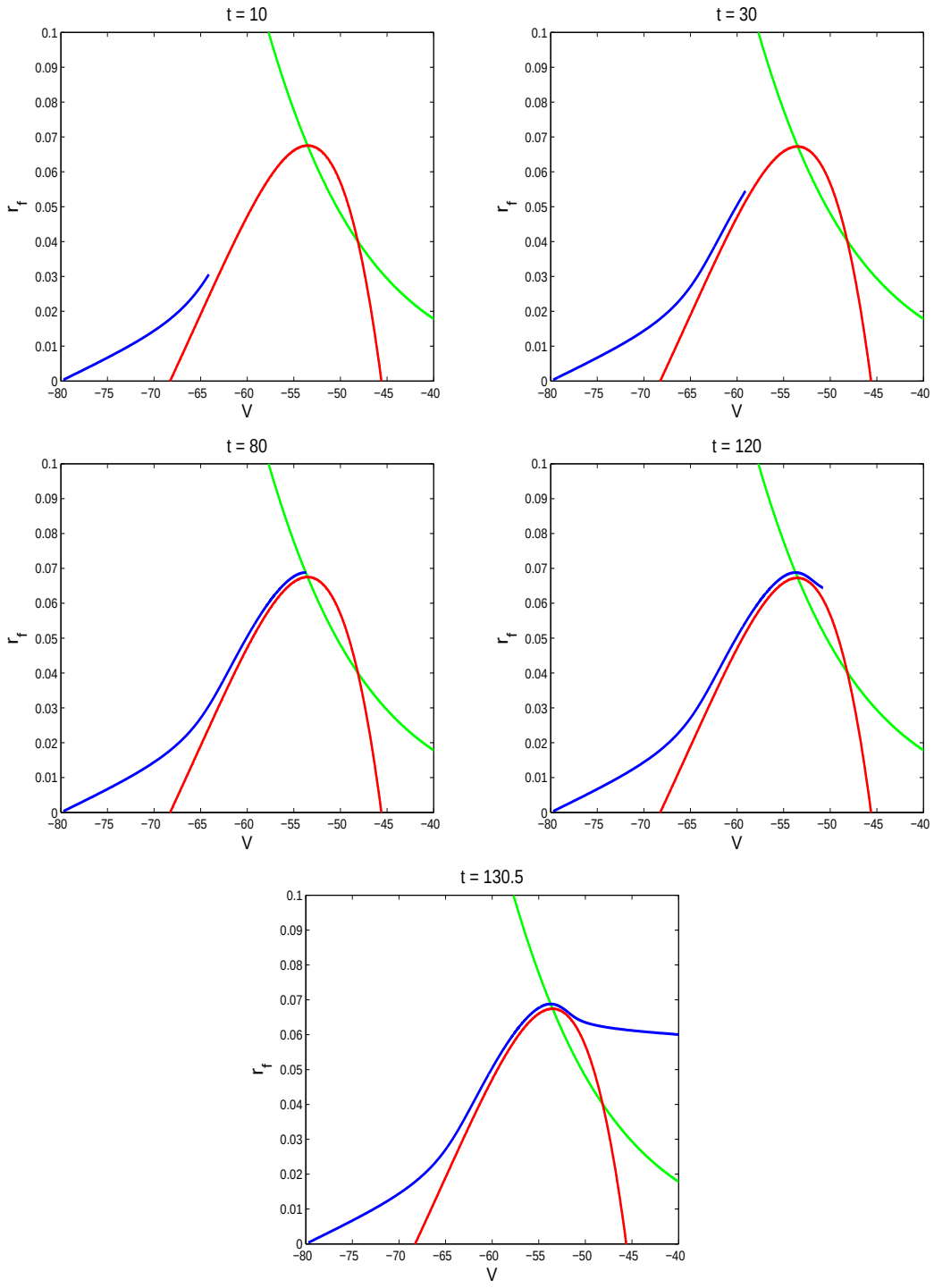

Figure 3.28 Dynamic two dimensional phase-space representation for $r_{f,reset} = 0$ and input frequency $f = 15$ Hz. $A_{in} = 0.007\ \mu A/cm^2$.

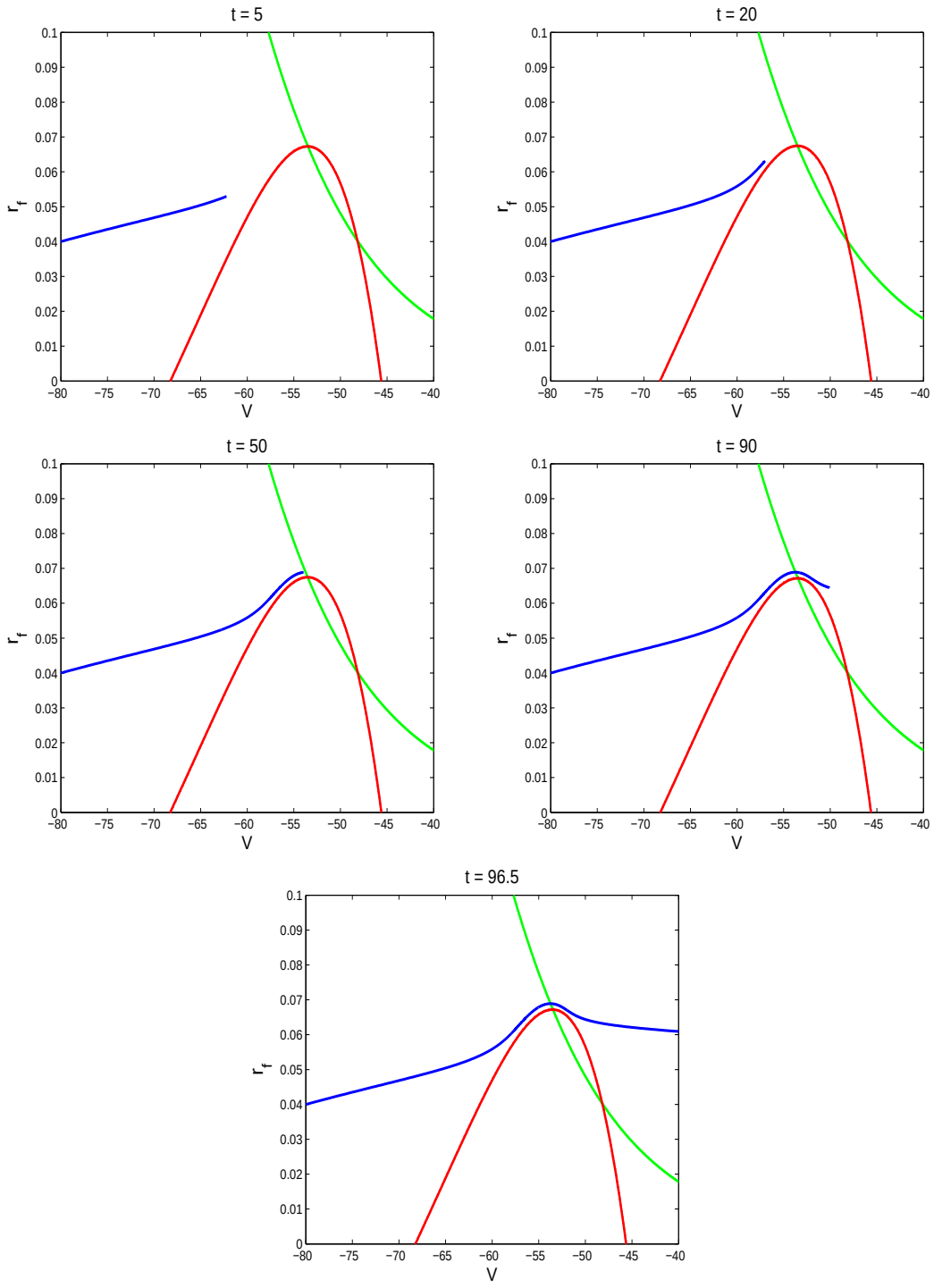

Figure 3.29 Dynamic two dimensional phase-space representation for $r_{f,reset} = 0.04$ and input frequency $f = 10$ Hz. $A_{in} = 0.007\ \mu A/cm^2$.

3.8.5 The structure of the phase-plane: Conductance-based input

In this section, we investigate the dynamical systems of SC with conductance-based oscillatory input (excitatory and inhibitory inputs). The V- and r_f-nullclines for the reduced 2D SC model (c_f =1 and $c_s = 0$) with these inputs are given by

$$N(V, r_s) = \frac{I_{app} - G_L(V - E_L) - G_p p_\infty (V - E_{Na})}{G_h(V - E_h)} - \frac{G_{e,in} S(t)(V - E_{syn})}{G_h(V - E_h)} \quad (3.13)$$

and

$$r_f(V) = r_{f,\infty}(V) \quad (3.14)$$

where

$$S(t) = \frac{1 + \sin \omega t}{2} \quad , \quad \omega = 2\pi f/1000$$

We use synaptic reversal potential, E_{syn}, such as $E_{ex} = 0\ mV$ and E_{in} = -75 mV for excitatory and inhibitory reversal potentials respectively.

Excitatory conductance inputs

In section 3.5.1, when SC receives the excitatory conductance inputs, it displays the prominent peak-frequency in high frequency (gamma frequency band) for large value of $G_{e,in}$ while it shows the prominent peak-frequency in theta frequency band for small value of $G_{e,in}$. Here, we study the dynamic structure how excitatory conductance inputs induces SC's hyper-excitability using the phase-space analysis. The 2D SC model captures the hyper-excitability for $G_{e,in} = 0.07$ where the prominent peak-frequency is $f = 49$ Hz. The corresponding voltage traces at this peak is shown in figure 3.31A. Here, we compare the case where SC displays the prominent peak-frequency at $f = 12$ Hz (in theta frequency band) with the case where SC displays the prominent peak-frequency at $f = 49$ Hz (in gamma frequency). Figure 3.30A is the

voltage trace at the prominent peak for $G_{e,in} = 0.0005\ mS/cm^2$. The prominent peak-frequency occur at $f = 12$ Hz. The trajectory's movement is shown in figure 3.30B–F. As time increases, the trajectory moves from figure 3.30B to F. When the trajectory enter the subthreshold regime, the V-nullcline starts moving down and the fixed point change from stable spiral to unstable spiral. When the trajectory approaches the knee of V-nullcline, the fixed point is unstable spiral. Thus the trajectory moves along the horizontal direction and escape the subthreshold regime firing an action potential. This dynamic structure is similar to the case when SC receives sinusoidal input currents. The different thing is the V-nullcline can not be above the control V-nullcline (red dot curve) without excitatory conductance input. For $G_{e,in} = 0.07$ mS/cm^2, the prominent peak-frequency occurs at $f = 49$ Hz. The voltage trace at $f = 49$ Hz is shown in figure 3.26A. When the trajectory approaches the subthreshold regime, the V-nullcline moves down. In this case, the trajectory moves fast along the horizontal direction and escape the subthreshold regime without any influence since the trajectory is far away from V-nullcline. This mechanism is different from the case for $G_{e,in} = 0.007$. For $G_{e,in} = 0.007$, the speed of trajectory was influenced by the fixed point since the trajectory was near V-nullcline. However, for $G_{e,in} = 0.05$, the trajectory is not influenced by the stability of fixed point. This is due to phasic-excitation since the excitatory inputs make V-nullcline moving down faster than the the speed of trajectory.

Taken together, this different mechanism explains the hyper-excitability when SC receives excitatory conductance inputs.

Inhibitory conductance inputs

We have studied the effect of inhibitory conductance-based input in section 3.5.2. The effect of inhibitory input on firing frequency is similar to the effect of

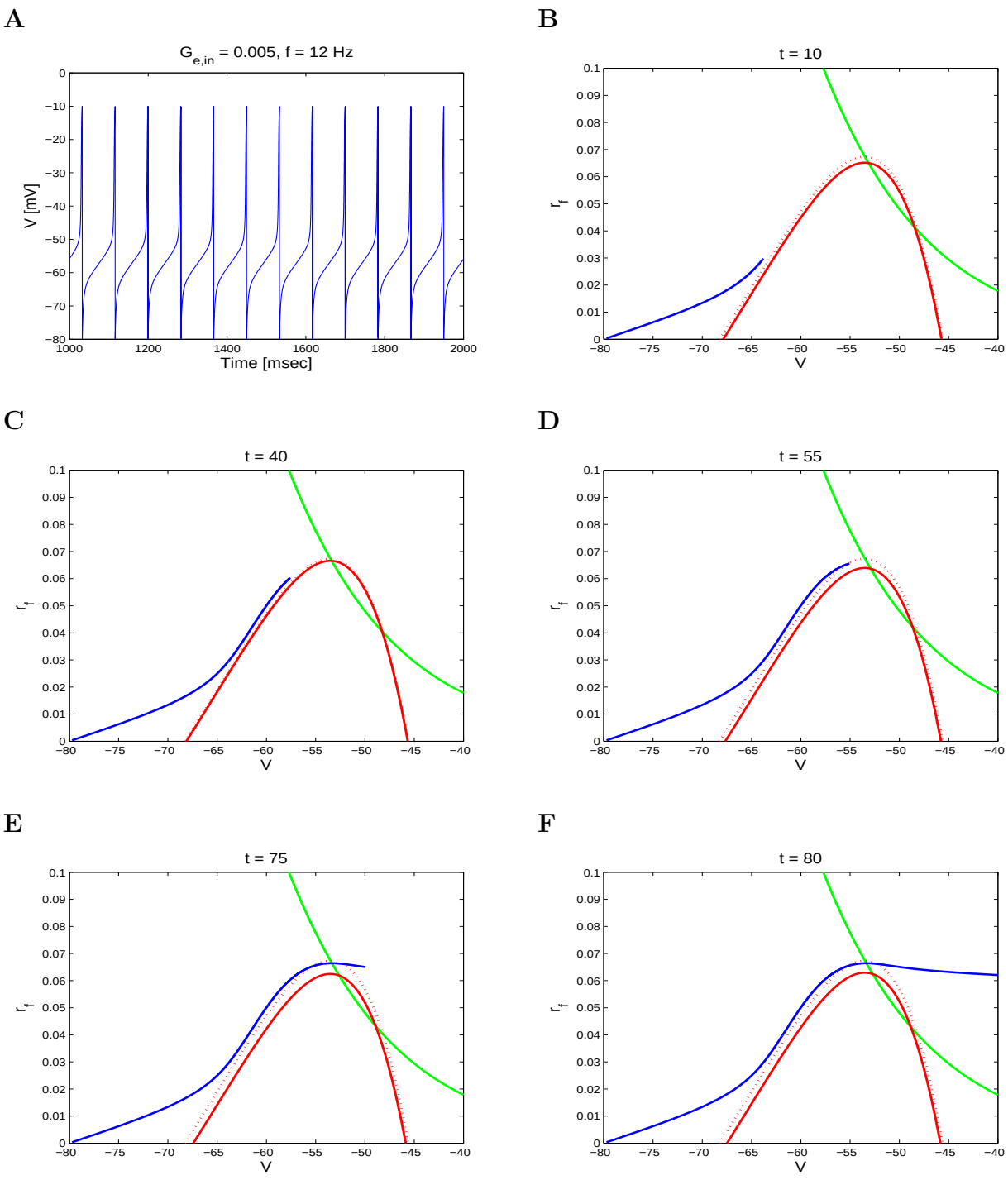

Figure 3.30 2D SC model. I_{app} = -2.21 $\mu A/cm^2$, $G_{e,in}$ = 0.005 mS/cm^2. The peak-frequency occurs at f = 12 Hz in theta frequency band. A is the voltage trace at f = 12 Hz. B, C and D are the trajectory's movement.

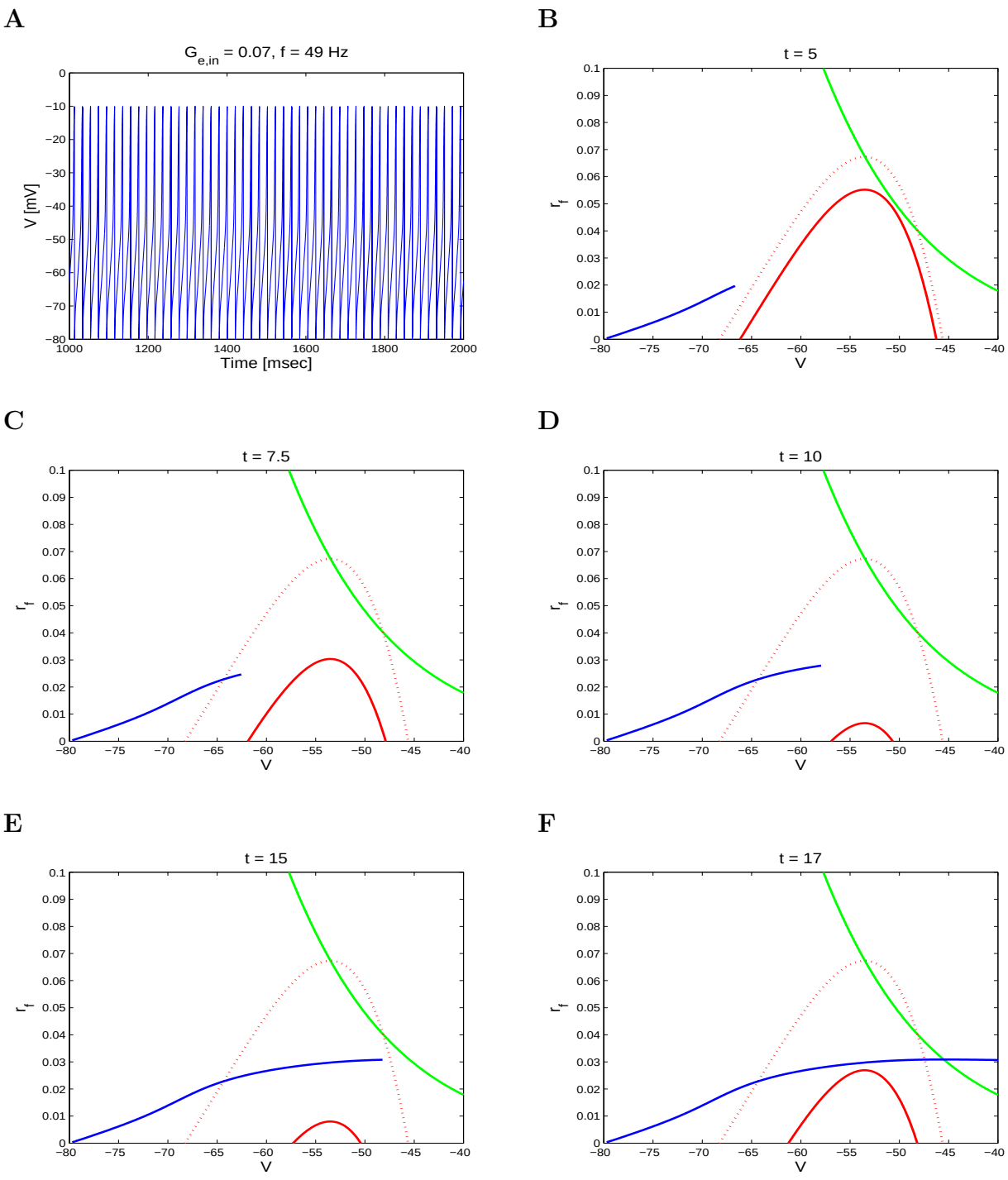

Figure 3.31 2D SC model. I_{app} = -2.21 $\mu A/cm^2$, $G_{e,in}$ = 0.07 mS/cm^2. The peak-frequency occurs at f = 49 Hz in gamma frequency band. A is the voltage trace at f = 49 Hz. B, C and D are the trajectory's movement.

sinusoidal current input. In this section, we study the dynamic structure of SC with inhibitory conductance inputs using the 2D SC model. In contrast to current input case, we found that the inhibitory conductance inputs induce abrupt increase in firing frequency due to phasic inhibition. In the simulations, we set the initial condition as the fixed point (V, r_f) = (-53.495, 0.0673) (the interaction between V- and r_f-nullcline) which is stable spiral (for I_{app} = -2.21 $\mu A/cm^2$) and then increase the maximal inhibitory conductance ($G_{i,in}$). Small increasing $G_{i,in}$ generate action potentials. This implies that the inhibitory conductance inputs induce the cell to fire.

Since this input inhibits SC, the V-nullcline is always above the control V-nullcline (red dot curve in figure 3.33 – 35). We present the dynamic structure for the voltage traces at peak-frequencies in figure 3.32A. For $G_{i,in} = 0.02$, the 2D SC model exhibits three peak-frequencies at $f = 10$, 19.5 and 23 Hz. The voltage traces at these peak-frequencies are show in Figure 3.32B, C and D. The corresponding phase-space diagrams are shown in Figure 3.33 – 35. Figure 3.33 corresponds to the traces shown in Figure 3.22B where SC displays first peak-frequency in firing frequency. Figure 3.34 and 35 corresponds to the traces shown in Figure 3.22C and D respectively. The initial points in all cases correspond to the fixed point where SC is silent. Increasing $G_{i,in}$ creates spikes, i.e., inhibition generates action potentials. This implies that the generation of spikes is not due to post inhibitory rebound. For specifically, in Figure 3.33, when the trajectory approaches fast towards the V-nullcline from the reset value (V, r_f) = (-80, 0), the V-nullcline moves up. However when the trajectory enters the subthreshold regime at $t = 50$, the V-nullcline starts moving down. Since the V-nullcline moves faster than the speed of trajectory, the trajectory moves along the horizontal direction and escape fast the subthreshold regime. In this case, the trajectory is not influenced by the stability of fixed points. However the trajectories at the second and third peak-frequencies show different movements. They are influenced

by slow manifold which affects reduce the speed of trajectory. In Figure 3.34, when the trajectory is close to the V-nullcline, the trajectory moves along the slow manifold and moves slowly. Since the V-nullcline moves fast, the trajectory moves fast along the horizontal direction and escape the subthreshold regime. In Figure 3.35, the trajectory shows different movement since the V-nullcline cross the trajectory at $t = 80\ ms$ (data not shown). Note that if the trajectory moving almost in the horizontal direction is not fast enough as compared to the speed at which the V-nullcline moves up, then it may be caught inside it. In this case, the trajectory is forced to reverse its direction and move towards the left (Figure 3.35 $t = 85\ ms$). As time increases, the V-nullcline moves down. Since the distance between the trajectory and V-nullcline is enough far away, the trajectory moves fast along the horizontal direction and escape the subthreshold regime firing an action potential (Figure 3.35 $t = 112$ to $120\ ms$).

From these figures, the phasic-inhibition generates action potentials. Whenever the trajectory is near the V-nullcline or the trajectory moving in the horizontal direction is not fast enough as compared to the speed at which the V-nullcline moves up, the trajectory moves along the slow manifold which affect the cell's spiking period.

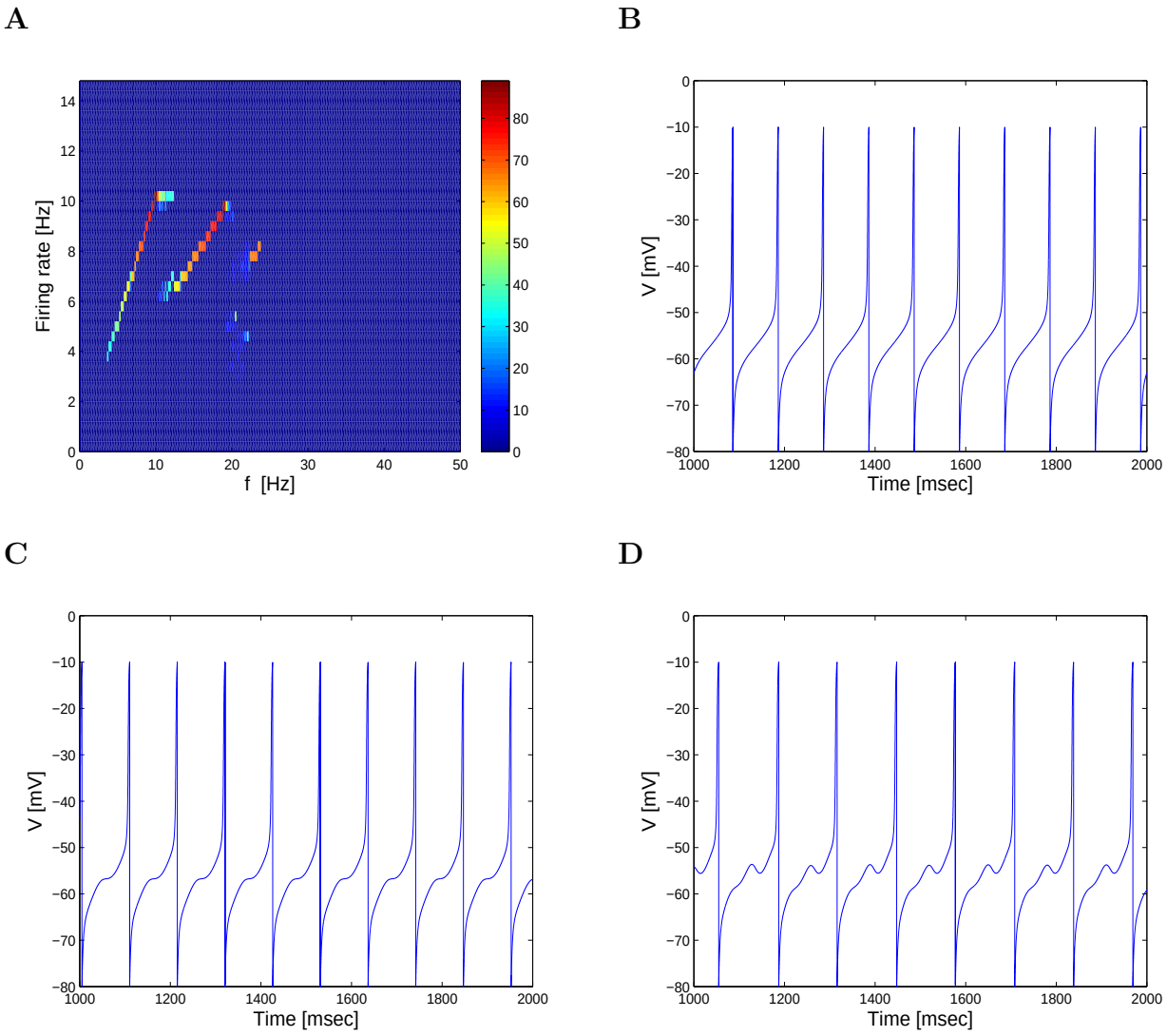

Figure 3.32 2D SC model. I_{app} = -2.21 $\mu A/cm^2$, $G_{i,in}$ = 0.05 mS/cm^2. A is the firing rate density curve. The peak-frequencies are seen at f = 10, 19.5 and 23 Hz. B, C and D are the voltage traces at f = 10, 19.5 and 23 Hz respectively.

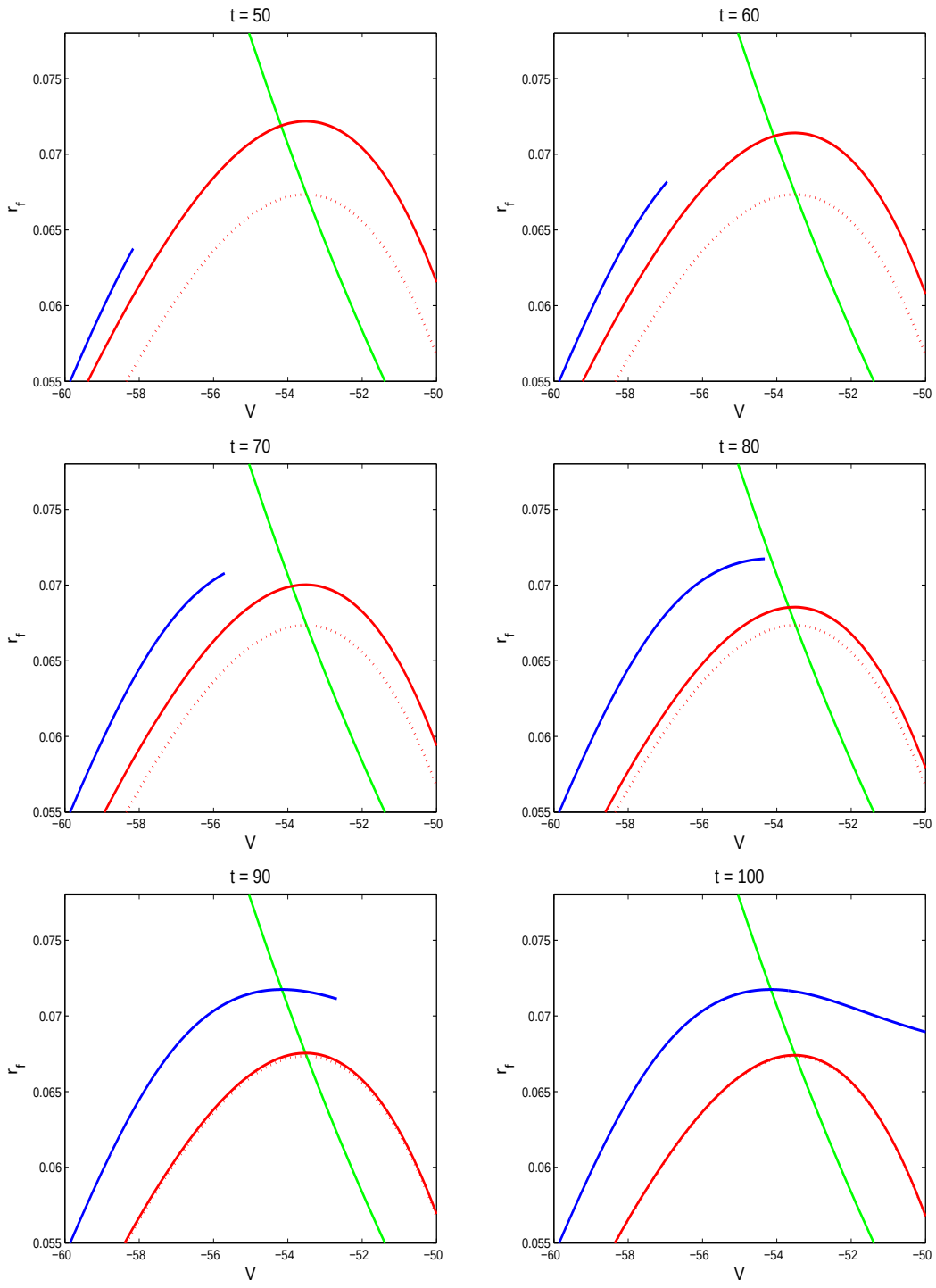

Figure 3.33 The structure of phase-plane of voltage trace at f=10.5 Hz. The trajectory moves without crossing V-nullcline.

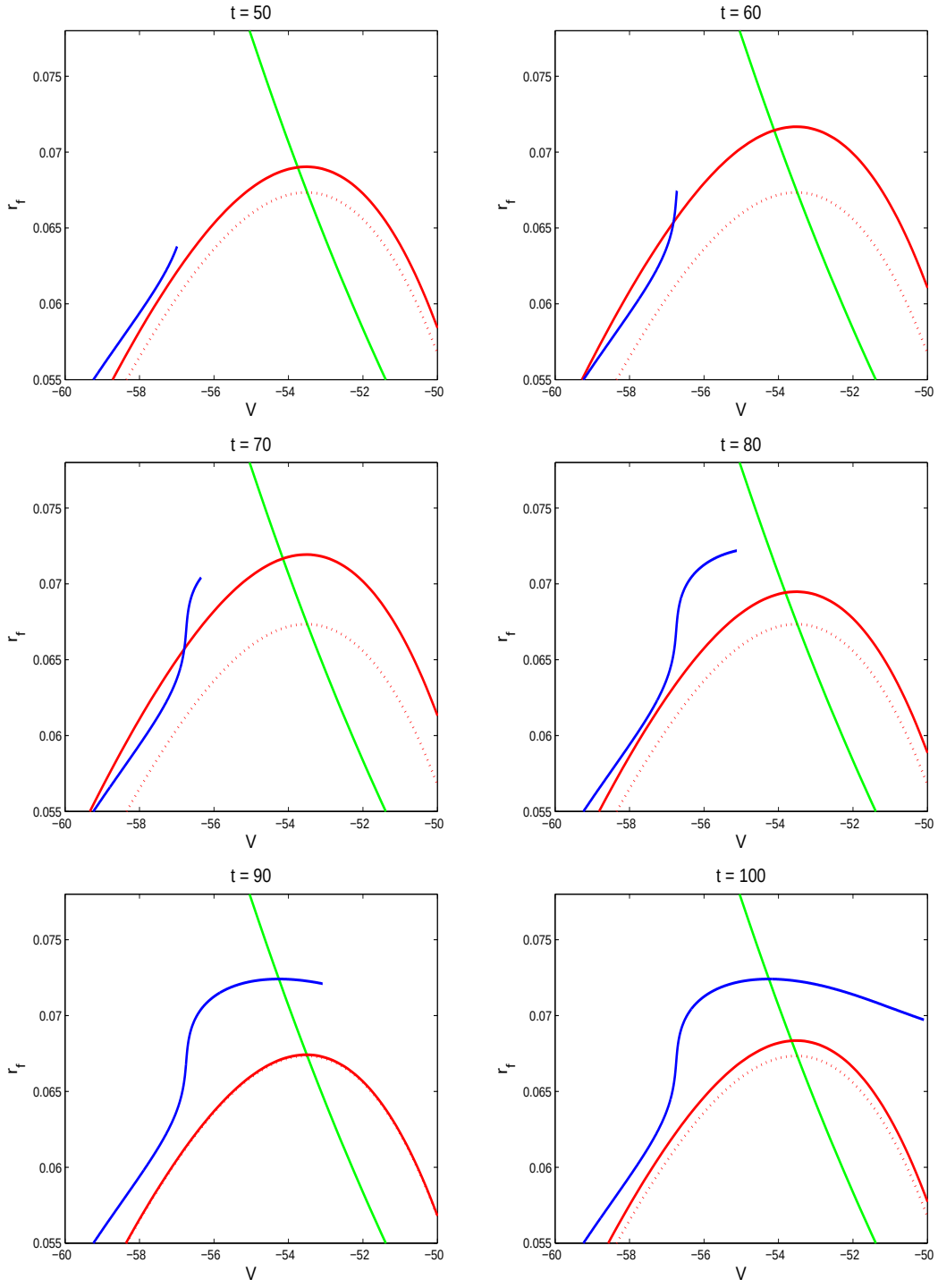

Figure 3.34 The structure of phase-plane of voltage trace at f=19.5 Hz.

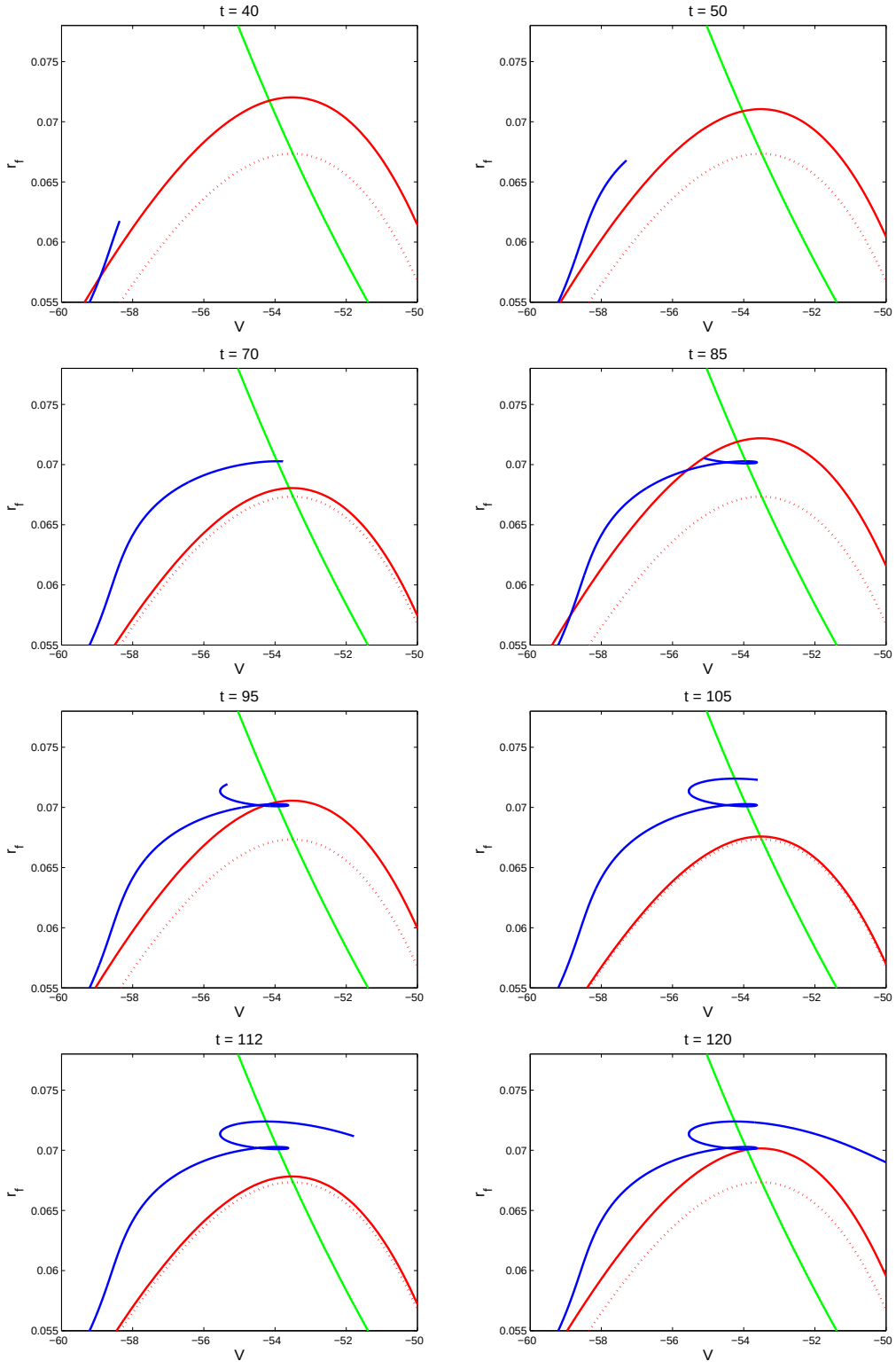

Figure 3.35 The structure of phase-plane of voltage trace at f=23 Hz.

3.8.6 The structure of the phase-plane: bursting properties in the linearized model

In section 3.6, the linearized model does not reproduce supra-threshold activity of SC in the nonlinear model when SC receives high-amplitude sinusoidal input currents. This is due to linear property of the system (Equation 2.8 – 2.10) such that the corresponding voltage traces to high-amplitude sinusoidal input currents display bursts of spikes at low frequency. In this section, we study the mechanism of the generation of bursting in the linear model. We use linearized 2D SC model with $r_s = 0$. Figure 3.36 shows the corresponding voltage traces to sinusoidal input current with $A_{in} = 0.4\ \mu A/cm^2$ and $f = 6$ Hz (voltage traces is blue and sinusoidal input current is red color). We plotted the sinusoidal input currents with voltage traces on the same window to see how high-amplitude sinusoidal input currents generate bursting in voltage traces. When sinusoidal input currents increase toward positive value, they endow corresponding voltage traces to reach voltage threshold firing an action potential. If there is no depolarized input current, the voltage is placed on reset value after spiking. However, in this case, input current is still depolarized. So the voltage traces show bursts of spikes instead of resetting the voltage.

Figure 3.37 shows two dimensional (V, r_f) projection of the phase-space using the linearized model. Time increases from A to L. The dynamic structure captures the trajectory movement from the end of the first burst of spikes and the end of the second burst of spikes (time duration is from 1070 to 1236 ms). The red line is V-nullcline with sinusoidal input currents and green line is r_f-nullcline. As t increase, the r_f-nullcline does not move but V-nullcline moves up and down. The red dot line is the V-nullcline without sinusoidal input currents. The sinusoidal input currents ($I_n(t)$) are parametrized by time t. As in nonlinear model, V-nullcline moves up and down by increasing time t. After the last spiking in first bursting, SC resets to V = -58

mV. The trajectory starts from reset value V_{reset}. As time increases, the V-nullcline first moves up and cross the trajectory at $t = 45$. And then the trajectory is forced to reverse its direction and moves towards the left (Figure 3.37C). As time increase, the V-nullcline moves down after $t = 60$ where the trajectories moves along the slow manifold (Figure 3.37D). When V-nullcline moves down, the trajectory moves in the horizontal direction so that SC generates first action potential in the bursting period (time duration is from 1070 to 1236 ms). After first action potential, the trajectory reset to V_{reset}. At the same time, V-nullcline is still moving down (Figure 3.37G) and the trajectory is in the horizontal direction. Therefore, SC displays the second spiking at $t = 122$ ms. After the second spike intra-burst, the V-nullcline is still moving down. The trajectory is still in the horizontal direction. The third spike is generated at $t = 142$ ms but the V-nullcline starts moving up (Figure 3.37J). After the third spiking, the trajectory resets and the V-nullcline does not cross the trajectory until it escapes the subthreshold regime, resulting in the generation of fourth spiking in bursting period.

These geometric pictures explain the dynamic mechanism leading to the generation of bursting in the linearized model. During bursting, the forcing term (sinusoidal input currents) does not influence the movement of trajectories. If the shape of V-nullcline is a parabolic like in nonlinear model, the trajectory spend more time in subthreshold regime along the V-nullcline. Since the shape of V-nullcline is not a parabolic but a line, the trajectory spend less time in subthreshold regime than in nonlinear case.

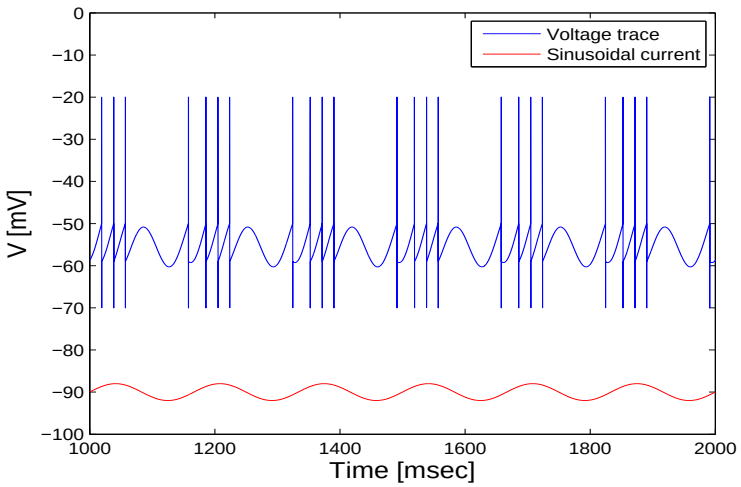

Figure 3.36 2D linear model. V_{th} = -50 mV and V_{reset} = -56 mV. The corresponding voltage traces to sinusoidal input current with A_{in} = 0.4 $\mu A/cm^2$ and f = 6 Hz using 2D linearized model (r_s=0). The voltage traces is blue and the sinusoidal input current is red color.

A

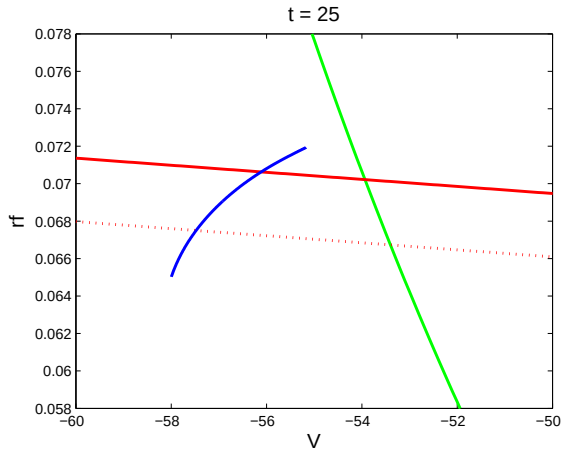
t = 25
rf
V
0.078
0.076
0.074
0.072
0.07
0.068
0.066
0.064
0.062
0.06
0.058
−60
−58
−56
−54
−52
−50

B

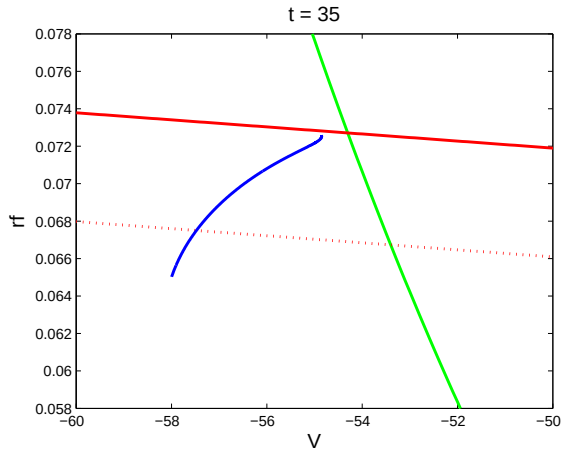
t = 35
rf
V
0.078
0.076
0.074
0.072
0.07
0.068
0.066
0.064
0.062
0.06
0.058
−60
−58
−56
−54
−52
−50

C

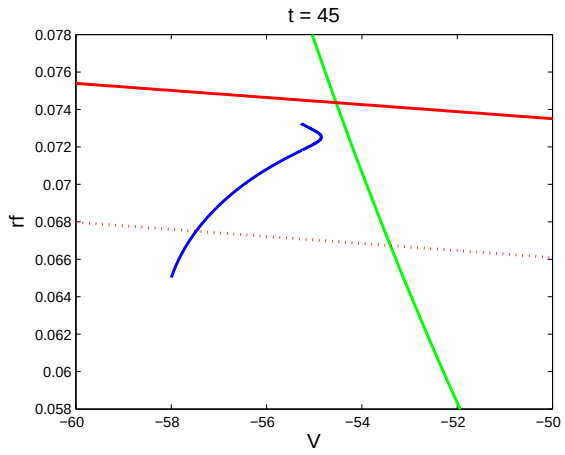
t = 45
rf
V
0.078
0.076
0.074
0.072
0.07
0.068
0.066
0.064
0.062
0.06
0.058
−60
−58
−56
−54
−52
−50

D

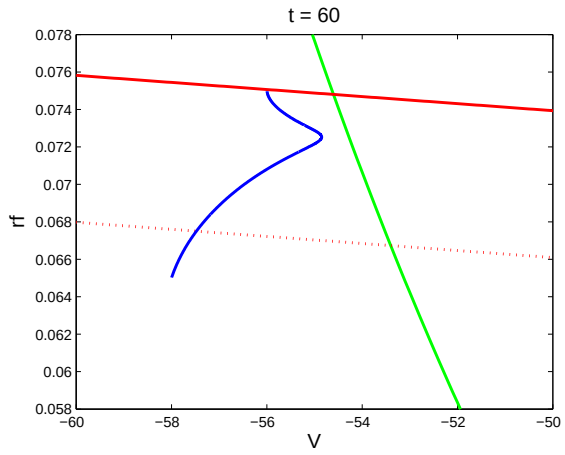
t = 60
rf
V
0.078
0.076
0.074
0.072
0.07
0.068
0.066
0.064
0.062
0.06
0.058
−60
−58
−56
−54
−52
−50

E

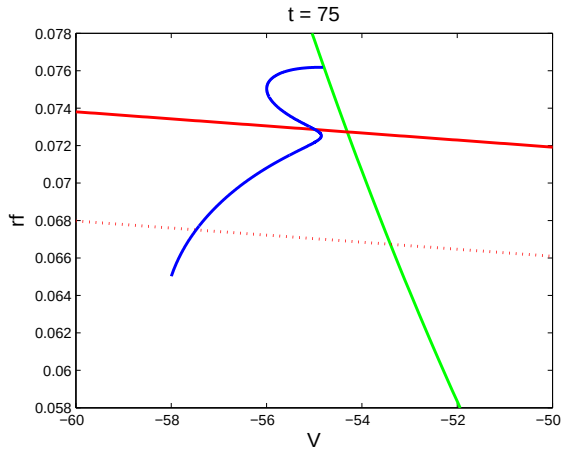
t = 75
rf
V
0.078
0.076
0.074
0.072
0.07
0.068
0.066
0.064
0.062
0.06
0.058
−60
−58
−56
−54
−52
−50

F

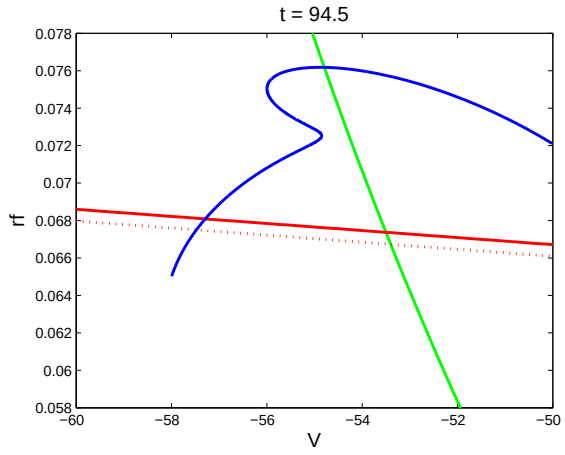
t = 94.5
rf
V
0.078
0.076
0.074
0.072
0.07
0.068
0.066
0.064
0.062
0.06
0.058
−60
−58
−56
−54
−52
−50

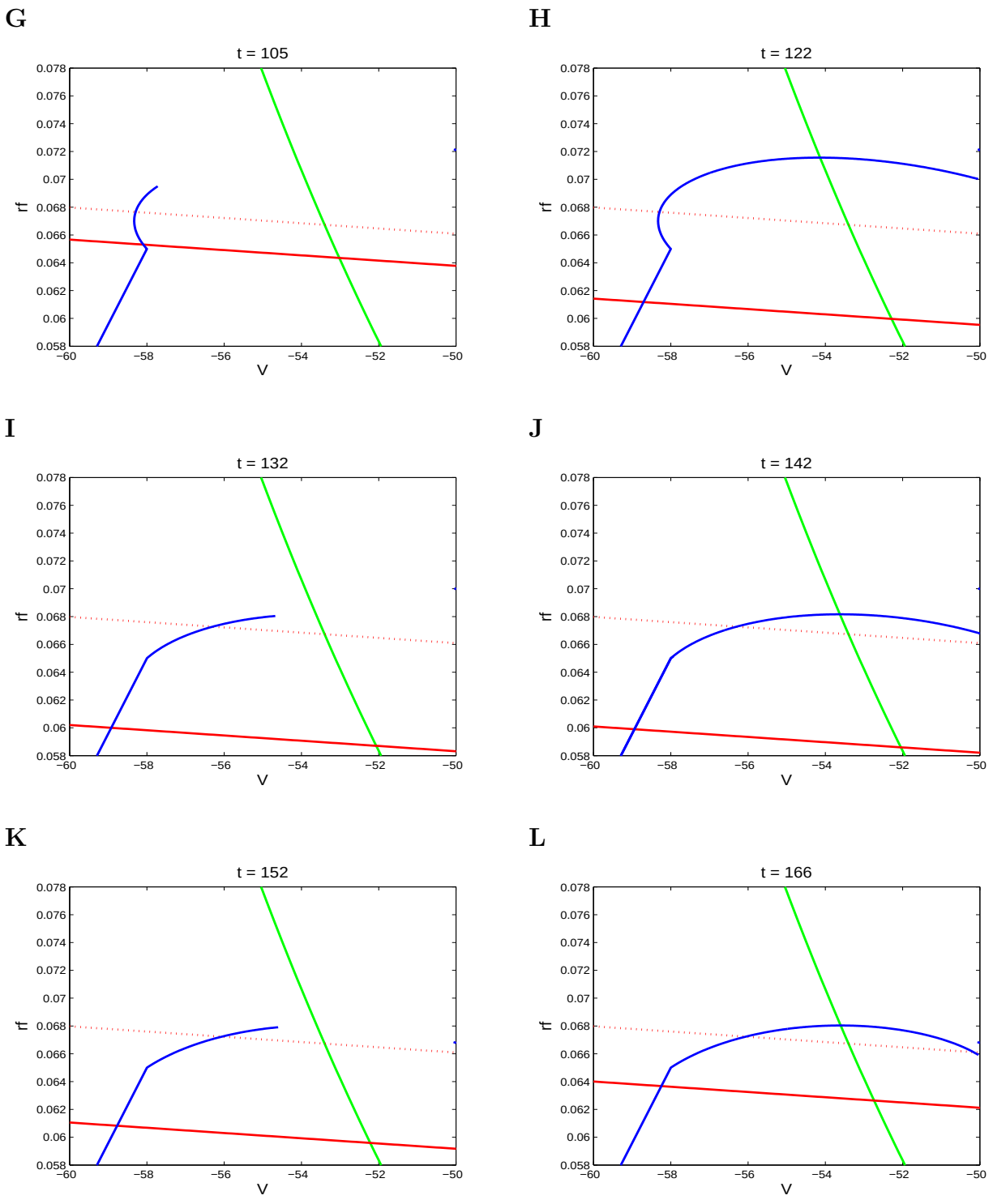

Figure 3.37 2D linear model. V_{th} = -50 mV and V_{reset} = -56 mV. The structure of phase-plane of voltage trace during bursting time duration in Figure 3.27 (with A_{in} = 0.4 and f = 6 Hz). Time increases from A to L. The trajectories move fast in horizontal direction firing action potential and V-nullcline is below the control V-nullcline (red dot line) during bursting time period.

CHAPTER 4

THE EFFECT OF *IN VIVO*-LIKE SYNAPTIC INPUTS ON STELLATE CELLS

Previous experimental work has shown that medial entorhinal cortex (MEC) layer II stellate cells (SCs) exhibit subthreshold oscillations and subthreshold resonance in the theta frequency band [16, 17, 19]. These intrinsic properties of SCs play an important role in the activity of neural networks in the entorhinal cortex and hippocampus[4]. An important question is under what conditions subthreshold oscillations on SCs can be generated at theta frequency band in the presence of *in vivo-like* Poisson-driven synaptic inputs. In a recent study, Fernandez et al. [20] have shown that amplitude of subthreshold oscillations in SCs are reduced under conductance-based synaptic inputs while these oscillations does not change under current-based synaptic inputs which were Poisson process-driven excitatory and inhibitory input. In this chapter, we investigated the mechanism underlying these phenomena in the context of the model, described in chapter 2. More specifically, we studied the effects of both conductance- and current-based synaptic inputs at various maximal synaptic conductance values on a SC model. We found that conductance-based synaptic inputs reduce subthreshold oscillations for low enough value of the maximal synaptic conductance value but amplify these oscillations at a higher range. This result is in contrast to the experimental result [20].

4.1 Background

4.1.1 Spike-Train Statistics

A spike train is a series of discrete action potentials from a neuron taken as a time series. This string of neuronal firing may be generated spontaneously or as a response to some external stimulus. The stochastic relationship between a stimulus and a response stems from the probabilities corresponding to every sequence of spikes that can be evoked by the stimulus. The probability of two spikes occurring together is not necessary to the product of the probabilities that they occur individually, because the presence of one spike may effect the occurrence of the other. If the spikes are statistically independent, the firing rate is all that is needed to the probabilities for all possible action potential sequences. A stochastic process that generates a series of action potentials is called a point process. The probability of one spike occurring at any given time could depend on the entire history of preceding spikes, so that the intervals between successive spikes are independent, the point process is called a renewal process. If there is no dependence at all on preceding spikes, so that the spikes are statistically independent, we have a Poisson process. The Poisson precess provides an extremely useful approximation of stochastic neuronal firing.

4.1.2 Poisson Process

A Poisson process is the simplest possible random process with no memory and is characterized by a single parameter, the rate of mean frequency λ. It is of great relevance to neurobiology, since a number of discrete spikes appear to follow a Poisson distribution closely [41, 42]. Let $\{N(t), t \geq 0\}$ be a sequence of spike-time (random spike times, Poisson process) with mean rate λ if:

1. Given any $t_0 < t_1 < t_2 < \cdots < t_{n-1} < t_n$, the random variables $N_{t_k} - N_{t_{k-1}}$, $k = 1, 2, \cdots, n$ are mutually independent.

2. For any $0 \leq t_{k-1} < t_k$ the average number of spikes occurring between t_{k-1} and t_k is $\lambda(t_k - t_{k-1})$.

The first condition indicates that the number of spikes occurring in one interval is independent of the number of spikes occurring in any other interval, provided they do not overlap. The second property tells us that the expected number of spikes is proportional to the rate times the duration of the interval.

It follows from these conditions that the actual number of spikes, $N(t_k) - N(t_{k-1})$, is a random variable with the Poisson probability distribution

$$Pr\{N(t_k) - N(t_{k-1}) = n\} = \frac{(\lambda(t_k - t_{k-1}))^n e^{-\lambda(t_k - t_{k-1})}}{n!} \tag{4.1}$$

with n=0, 1, 2, $\cdot$.

The parameter λ specifies the average number of events per unit time. With $t_{k-1} = t$ and $t_k = t + \Delta t$, we have for the probability that exactly k spikes occur in the interval Δt.

$$Pr\{N(t + \Delta t) - N(t) = n\} = \frac{(\lambda \Delta t)^n e^{-\lambda \Delta t}}{n!} \tag{4.2}$$

If $\lambda \Delta t \ll 1$, that is, if much less than one event is expected to occur in the interval Δt, the $e^{-\lambda \Delta t}$ term can be expanded into a Taylor series 1-$\lambda \Delta t + \frac{(\lambda \Delta t)^2}{2!}$-$\frac{(\lambda \Delta t)^3}{3!}$ + ... Therefore,

$$Pr\{N(t + \Delta t) - N(t) = 0\} = e^{-\lambda \Delta t} \approx 1 - \lambda \Delta t \tag{4.3}$$

$$Pr\{N(t + \Delta t) - N(t) = 1\} = \lambda \Delta t e^{-\lambda \Delta t} \approx \lambda \Delta t \tag{4.4}$$

4.1.3 Generating Poisson Spike Trains

There are two commonly used procedures for numerically generating Poisson spike trains The first approach is based on the approximation in equation 4.4 for the probability of a spike occurring during a short time interval. For the homogeneous Poisson process (the rate λ is constant), this expression can be rewritten as

$$P\{1 \text{ spike during } \Delta t\} = \lambda \Delta t$$

This equation can be used to generate a Poisson spike train by first subdividing time into a bunch of short intervals, each of duration Δt. Then generate a sequence of random number x_i, uniformly distributed between 0 and 1. For each interval, if $x_i \leq \lambda \Delta t$, generate a spike. Otherwise, no spike is generated.

The second approach for generating a homogeneous Poisson spike train is simply to choose inter spike intervals randomly from the exponential distribution. Each successive spike time is given by the previous spike time plus the randomly drawn inter spike interval. Now each spike is assigned a continuous time value instead of a discrete time bin. However, to do anything with the simulated spike train, it is usually much more convenient to discretely sample the spike train, which makes this approach for generating the spike times equivalent to the first approach described above. Here, we used the second approach for generating Poisson spike train.

4.2 Methods

We follow [20]. SCs received inputs consisting of combined excitatory and inhibitory Poisson-driven synaptic conductances or currents. Synaptic inputs consisted of two independent Poisson processes generating unitary synaptic events. Inhibitory and excitatory events were delivered at a frequency of 1000 and 500 Hz respectively. The frequency of excitatory and inhibitory inputs was based on the fact that spontaneous

background inhibitory frequency is greater than excitatory frequency in slices. In the presence of conductance-based synaptic inputs, subthreshold oscillations are highly attenuated or entirely eliminated. Conversely, with current-based synaptic input stellate cells retain their ability to generated subthreshold oscillation in the theta band [20]. The introduction of conductance-based synaptic inputs abolished the peak at theta frequencies in the power spectrum density (PSD) for subthreshold voltage traces. Under current-based synaptic inputs, which generated a comparable level of membrane voltage fluctuations, the PSD does not change its peak at theta frequencies.

4.2.1 Modeling Approach

We follow [20]. Synaptic protocols consisted of two independent Poisson processes generating unitary synaptic events (S_e and S_i for excitatory and inhibitory inputs respectively). These were modeled using biexponential functions of the form:

$$S(t) = e^{-t|t_{dec}} - e^{-t|t_{drise}} \tag{4.5}$$

For $GABA_A$-based inhibition, $t_{rise} = 0.5\ ms$ and $t_{dec} = 5\ ms$. For AMPA-based excitation, $t_{rise} = 0.25\ ms$ and $t_{dec} = 2.5\ ms$ [20].

The values of the reversal potentials are $E_e = 0\ mV$ and $E_i = -75\ mV$. For excitation and inhibition, individual synaptic events had the same maximal conductance.

From equation 2.1, the current-balance equation for both conductance and current-based synaptic inputs is given by

$$C\frac{dV}{dt} = I_{app} - I_{Na} - I_K - I_L - I_h - I_p - I_{syn} \tag{4.6}$$

where

$$I_{syn} = \sum_{j=1}^{N_e} H(t-t_j)G_e S_e(t_j)(V-E_e) + \sum_{k=1}^{N_i} H(t-t_k)G_i S_i(t_k)(V-E_i) \tag{4.7}$$

$$I_{syn} = \sum_{j=1}^{N_e} H(t-t_j)G_e S_e(t_j) - \sum_{k=1}^{N_i} H(t-t_k)G_i S_i(t_k) \tag{4.8}$$

G_e and G_i are maximal synaptic conductance for excitatory and inhibitory inputs respectively and t_j and t_k (j=1,...,N_e and k=1,...,N_i) are independent Poisson distributed times.

Figure 4.1 illustrates the presynaptic activity of S_e and S_i for excitatory and inhibitory activity respectively. The mean value of S_i is greater than the mean of S_e. Note that the mean value of S_e is 0.2704 and the mean value of S_i is 0.4880.

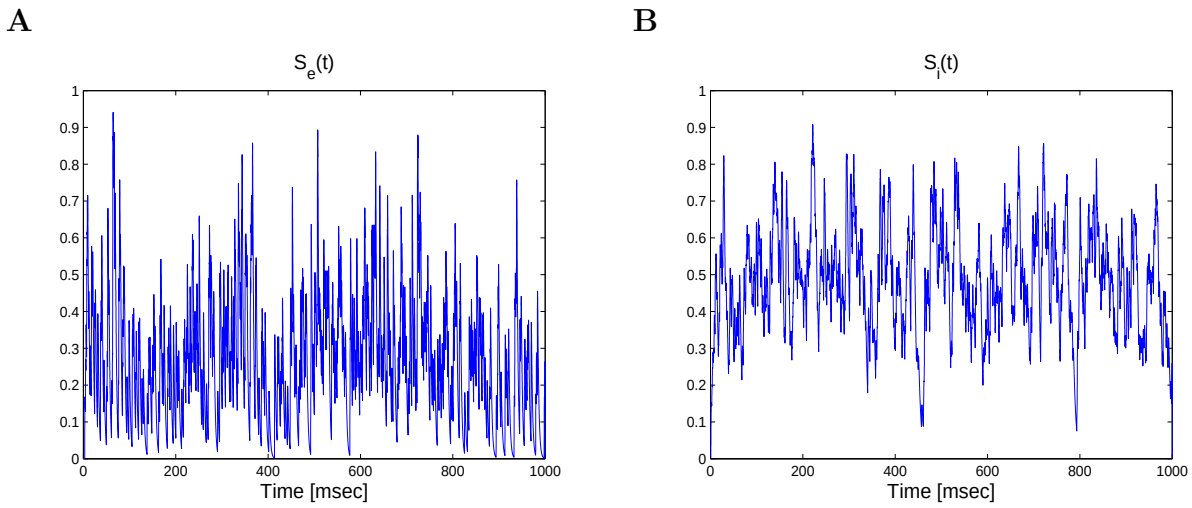

Figure 4.1 Activity of excitatory (left panel) and inhibitory (right panel) driven Poisson process. The mean value of S_i is almost double to the mean value of G_e: the mean value of S_i and S_e is 0.4880 and 0.2704 respectively.

We begin with a characterization of PSD of subthreshold oscillations in response to Poisson process driven conductance-based synaptic inputs by increasing the maximal

synaptic conductance. For the numerical analysis, we used modified euler method with time step size Δt=0.05 ms. The PSD of membrane potential has been calculated using Matlab(reference). We used the fast Fourier transform (FFT) algorithm for the calculation of the PSD.

4.3 Numerical results using 7D stellate cell model

The 7D full SC model shows subthreshold oscillation near 10 Hz and the amplitude of PSD at the peak is 0.8871 when I_{app} = -2.72 $\mu A/cm^2$. For higher value of I_{app}, this model displays action potentials. Therefore, in our work, we set the control level (synaptic inputs are blocked) when I_{app} = -2.72$\mu A/cm^2$ where the SC model displays only subthreshold oscillations. We calculated the PSD for voltage traces in response to synaptic inputs for different maximal synaptic conductance values. We compared the peak-amplitude in PSD for voltage traces. In order to capture the experimental results [20], it is important to prevent the cell from firing since synaptic inputs induces the generation of action potentials. In order to achieve that, we adapt (decrease or increase) injected current.

4.3.1 SC model captures the experimental results

Figure 4.2 shows that conductance-based synaptic inputs reduce the amplitude of subthreshold oscillations of membrane voltage while the current-based synaptic inputs does not change its peak at theta frequencies in PSD. Figure 4.2A and B show synaptic conductance- and current-based inputs respectively. Figure 4.2C shows the PSD for membrane voltage under control, conductance- and current-based synaptic inputs. We used different maximal synaptic conductance for conductance- and current-based synaptic inputs since the amount of synaptic currents should be comparable (each synaptic input has the same mean value of synaptic input). For conductance-based

synaptic input, we used $G_e = G_i = 0.05\ \mu S/cm^2$ and $G_e = G_i = 0.5\ \mu S/cm^2$ was used for current-based synaptic input. The difference between conductance- and current-based synaptic inputs is the amplitude of fluctuations in time (the mean values of each current are the same). The amplitude of conductance-based synaptic input is larger (almost 4 times) than the current-based synaptic input. But the effect of each currents is different. The conductance-based synaptic input significantly reduced the amplitude of subthreshold oscillations but current-based synaptic input does not alter the amplitude of subthreshold oscillations. These numerical results are in agreement with the experimental data [20]. Therefore we hypothesize that the amplitude difference between conductance- and current-based synaptic current plays a key role in reducing or retaining the amplitude of subthreshold oscillations.

4.3.2 The effect of maximal synaptic conductance on the stellate cell's subthreshold activity under conductance-based synaptic inputs

Passive properties of cells act as low pass filter: i.e., they reduce the amplitude and frequency preference of subthreshold oscillations. Conductance-based synaptic inputs have been shown to produce a similar effect [20, 43]. An interesting question arises under what conditions these inputs behave like a leak current on the SCs. In this section, we investigated the effect of maximal synaptic conductance on the SC subthreshold activity under conductance-based synaptic inputs. Figure 4.3 shows the PSD for SC's subthreshold oscillations in respond to conductance-based synaptic inputs at various maximal synaptic conductance values. The peak-amplitude in PSD for subthreshold oscillations for maximal synaptic conductance ranged from 0 to 0.15 $\mu S/cm^2$ is below the peak-amplitude at the control case but it starts increasing for higher values. This result is in contrast to the experimental results and suggests that

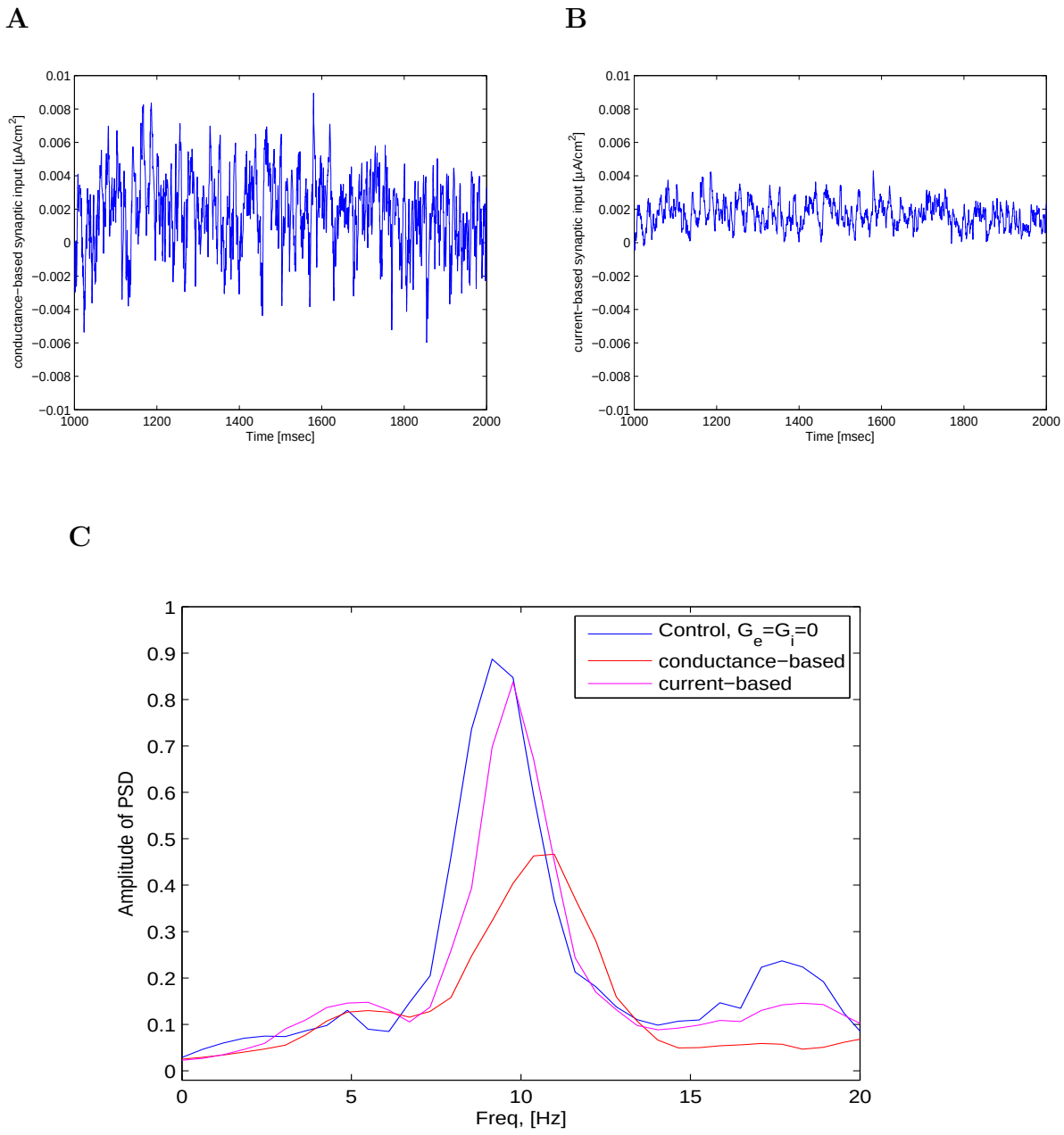

Figure 4.2 SC model captures the experimental result[20]. A and B show the conductance- and current-based synaptic inputs respectively. C shows the PSD for membrane voltage under control, conductance- and current-based synaptic inputs. We used the maximal synaptic conductance: G_e=G_i =0.05 $\mu S/cm^2$

the effect of conductance-based synaptic inputs does not behave like a leak current on SCs for higher maximal synaptic conductance values.

Figure 4.4 shows conductance-based synaptic inputs with respect to time for various maximal synaptic conductance values (G_{syn} =G_e = G_i = 0.05, 0.1, 0.15 and 0.2). Increasing G_{syn} results in increasing the fluctuations of conductance-based synaptic inputs (I_{syn}).

In order to understand why conductance-based synaptic inputs affect differently on the SC subthreshold activity with various G_{syn}, we will introduce $I_{S,L}$ which adapts leak current to include synaptic effects in next section.

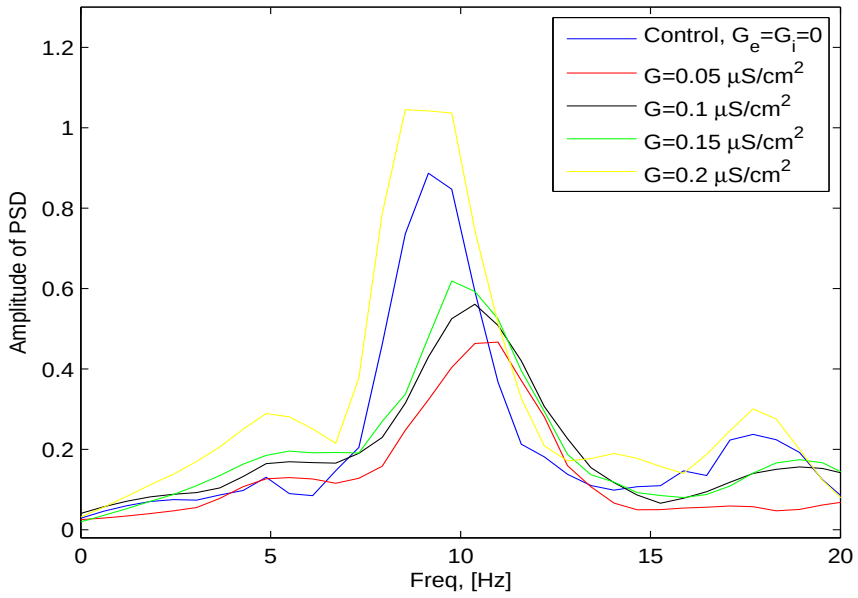

Figure 4.3 The PSD for voltage traces in response to conductance-based synaptic inputs at various maximal synaptic conductance values (G_e = G_i = 0, 0.05, 0.1, 0.15 and 0.2 $\mu S/cm^2$. The peak-amplitude in PSD for subthreshold oscillations for maximal synaptic conductance ranged from 0 to 0.15 $\mu S/cm^2$ is below the peak-amplitude at the control case but it starts increasing for higher value.

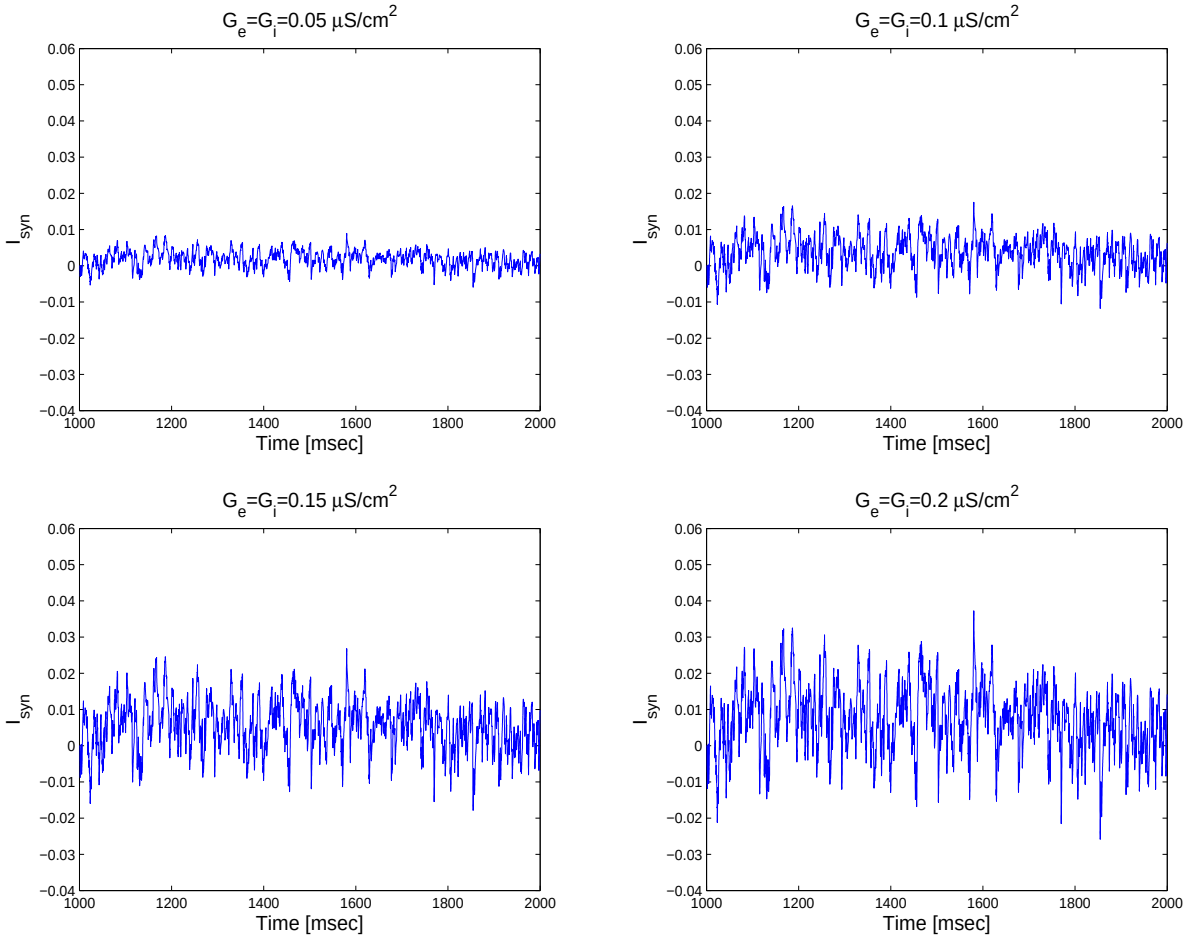

Figure 4.4 Conductance-based synaptic input (I_{syn}) with different values of maximal synaptic conductance ($G_{syn} = G_e = G_i$). Increasing G_{syn} results in amplifying fluctuations of I_{syn}.

4.3.3 Modifying synaptic current with constant value of S_e and S_i

The term I_{syn} in equation 4.6 consists of I_E and I_I, excitatory and inhibitory synaptic inputs respectively. Thus I_{syn} in equation 4.7 and 4.8 can be rewritten in the following way

$$I_{S,L} = (G_e S_e + G_i S_i)(V - \frac{G_e S_e E_e + G_i S_i E_i}{G_e S_e + G_i S_i}) \tag{4.9}$$

For constant values of S_e and S_i in equation 4.9, $I_{S,L}$ is a passive current with a similar behavior as I_L. The effective maximal conductance and reversal potential of $I_{S,L}$ are

$$G_e S_e + G_i S_i \quad and \quad \frac{G_e S_e E_e + G_i S_i E_i}{G_e S_e + G_i S_i}$$

The current-balance equation for $I_{S,L}$ is given by

$$C\frac{dV}{dt} = I_{app} - I_{Na} - I_K - I_h - I_p - I_L - I_{S,L} \tag{4.10}$$

4.3.4 The effect of maximal synaptic conductance on the stellate cell's subthreshold activity under the presence of $I_{S,L}$

Figure 4.5 shows the PSD for subthreshold oscillations in respond to $I_{S,L}$ with G_e and $G_i = 0$, 0.05, 0.1, 0.15 and 0.2. In this simulation, we observed that $I_{S,L}$ reduced the peak-amplitude in PSD by increasing G_e and G_i. For G_e=$G_i = 0.05$, $I_{S,L}$ reduce the peak-amplitude without altering peak frequency but this current not only reduce peak-amplitude in PSD for subthreshold oscillations but also alter peak frequency to higher frequency for higher value of maximal synaptic conductance. These results indicate that $I_{S,L}$ reduce subthreshold oscillations and that change the properties of subthreshold resonance. These are consistent to the previous results [20].

Figure 4.6 shows the activity of $I_{S,L}$ with respect to time for various maximal synaptic conductance values which were used in Poisson synaptic input case. These results display that increasing maximal synaptic conductance.

In Poisson-driven conductance-based synaptic input, increasing G_e and G_{in} results in increasing mean value of $I_{S,L}$. This result is different from Poisson case where increasing maximal synaptic conductance results in amplifying the fluctuations of conductance-based synaptic inputs. This implies that SC receives inhibition from $I_{S,L}$, which cause the amplitude of subthreshold oscillations to reduce.

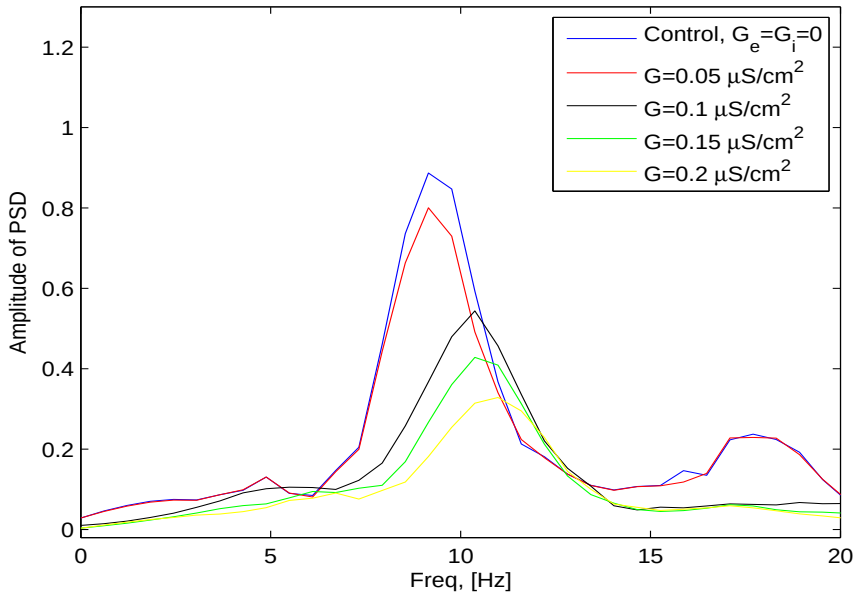

Figure 4.5 The PSD for subthreshold oscillations in respond to $I_{S,L}$ with G_e and G_i = 0, 0.05, 0.1, 0.15 and 0.2. Adapting leak current, $I_{S,L}$, reduced the peak-amplitude in PSD by increasing maximal synaptic conductance. For G_e=G_i = 0.05, $I_{S,L}$ reduce the peak-amplitude without altering peak frequency but this current not only reduce peak-amplitude in PSD for subthreshold oscillations but also alter peak frequency to higher frequency for higher value of maximal synaptic conductance.

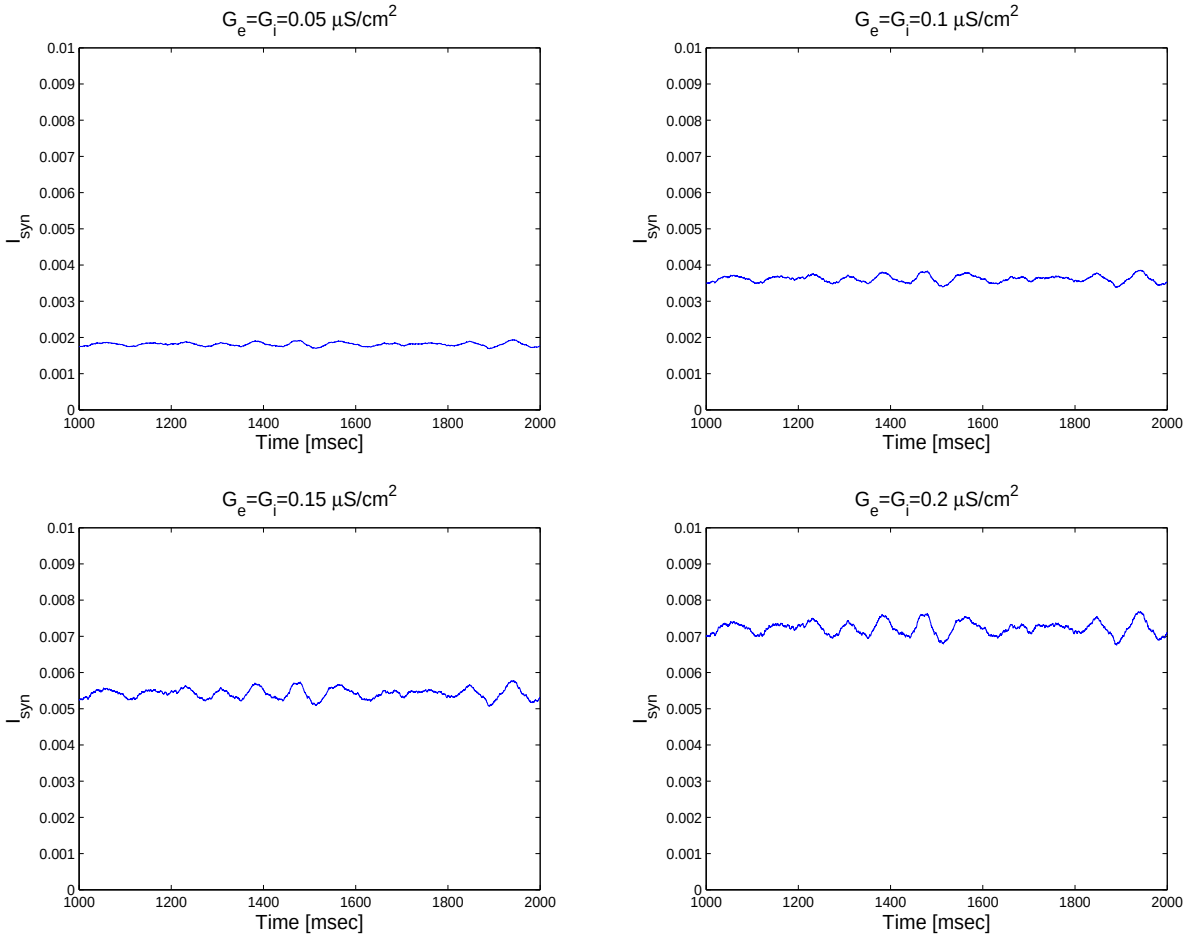

Figure 4.6 The activity of $I_{S,L}$ with respect to time for various maximal synaptic conductance values which were used in Poisson synaptic input case. These results display that increasing maximal synaptic conductance.

4.3.5 Different effects of S_e and S_i under Poisson driven conductance-based synaptic input and synaptic leak current

In previous section, we discussed the effect of presynaptic activity under both Poisson driven conductance-based synaptic inputs and $I_{S,L}$. Also we studied changes of membrane voltage responded to both synaptic inputs with various maximal synaptic conductance (0, 0.1, 0.15 and 0.2 $\mu S/cm^2$). Here, we investigate the effect of G_e and G_i on the peak-amplitude PSD for subthreshold oscillations. We varied systemically G_e and G_i in both Poisson conductance-based synaptic inputs and $I_{S,L}$ (figure 4.7). In Poisson case, the peak-amplitude in PSD first decreases but starts increasing (showing monotonic decreasing but changed the direction to monotonic increasing at some critical value ($\sim 0.5\mu S/cm^2$). Whereas, in $I_{S,L}$ case, the numerical simulations exhibits standard behavior of leak current (I_L). From these graphs, it can be thought that what biophysical parameter or mechanism produce these non-monotonic behavior in Poisson conductance-based inputs : large fluctuations of conductance-based synaptic inputs may produce non-monotonic behavior in peak-amplitude in PSD.

4.4 Numerical results using reduced 3D stellate cell model

In this section, we examined the effect of both conductance- and current-based synaptic currents (driven Poisson process) using the reduced 3D SC model [11] (described in section 2.3). We used the same parameters used in 7D SC model. The goal of this section is that the reduced 3D SC model is appropriate to reproduce the phenomena observed in 7D SC model and understand the evolution of dynamical system underlying reducing and amplifying the subthreshold oscillation under conductance-based synaptic inputs using phase-space analysis.

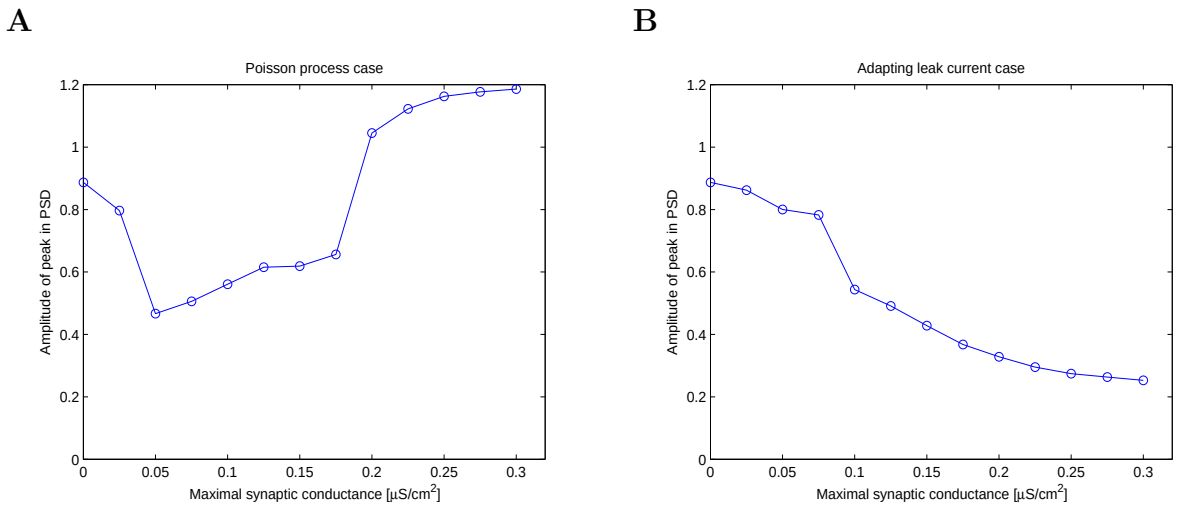

Figure 4.7 Systemically increasing maximal synaptic conductance shows different effects in both conductance-based synaptic input and $I_{S,L}$. A is the case of conductance-based synaptic input and B is the case of $I_{S,L}$ in terms of G_{syn}. For conductance-based synaptic input driven by Poisson process, the peak in PSD first decreased and then started increasing at the critical value of maximal synaptic conductance while the peak in PSD kept decreasing with increasing G_e and G_i in $I_{S,L}$ case.

4.4.1 The reduced stellate cell model captures the experimental results

We set the control level (I_{app} = -2.59 $\mu A/cm^2$, no synaptic inputs) where 3D SC model exhibits only subthreshold oscillations. For higher value of I_{app}, this model starts generating action potential. And we calculated the PSD of membrane potential under control, conductance-, and current-based synaptic current. We used the same excitatory and inhibitory synaptic protocols used in 7D SC model. We used $G_e = G_i$ = 0.05 $\mu S/cm^2$ for conductance-based synaptic inputs and $G_e = G_i$ = 0.5 $\mu S/cm^2$ for current-based synaptic inputs. In Figure 4.8 we show graphs of conductance- and current-based synaptic inputs (figure 4.8A and B, respectively) and the PSD for subthreshold oscillations in respond to no synaptic input (control), conductance-, and current-based synaptic inputs (figure 4.8C).

4.4.2 The effect of G_e and G_i on stellate cell under Poisson process and synaptic leak current

In this section, we study the effect of G_e and G_i on SC under conductance-based synaptic input and adapting leak current ($I_{S,L}$). We measured the PSD for subthreshold oscillations in respond to both conductance-based synaptic current (figure 4.8A) and adapting leak current (figure 4.8B) for $G_e = G_i$ = 0, 0.05, 0.15, and 0.2 $\mu S/cm^2$. Figure 4.9 shows the amplitude-peak of PSD for subthreshold oscillations as a function of maximal synaptic conductance. When we systemically increased the maximal synaptic conductance from 0 to 0.3, the amplitude-peak in PSD first decreased but started increasing at $G_e = G_i$ = 0.075 in conductance-based synaptic input but the peak in PSD kept decreasing in synaptic leak current. These numerical results are consitent to what we observed in 7D SC model.

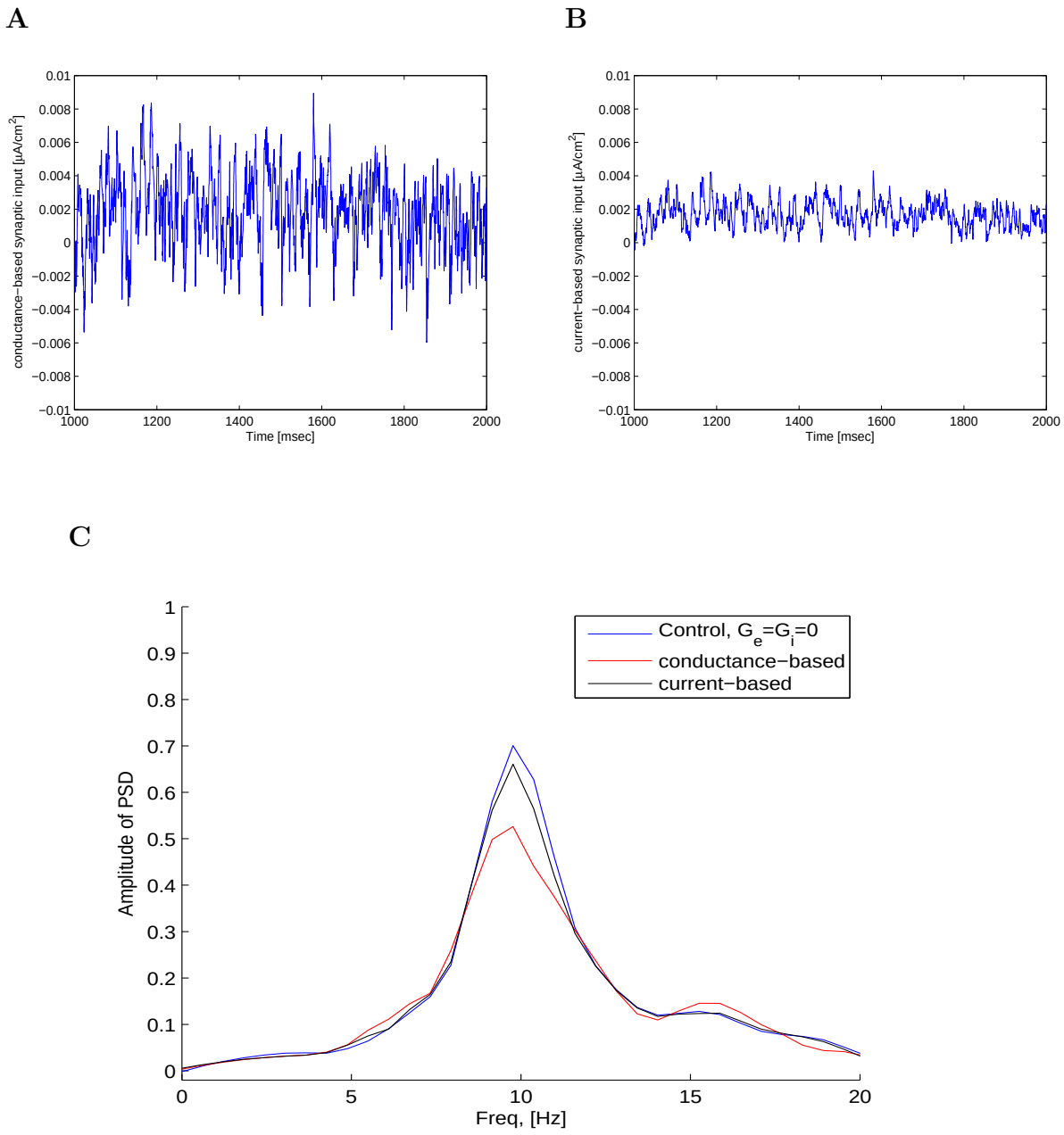

Figure 4.8 The reduced 3D SC model captures the experimental result[20]. A and B show the conductance- and current-based synaptic inputs respectively. C shows the PSD for membrane voltage under control, conductance- and current-based synaptic inputs. We used the maximal synaptic conductance: G_e=G_i =0.05 $\mu S/cm^2$.

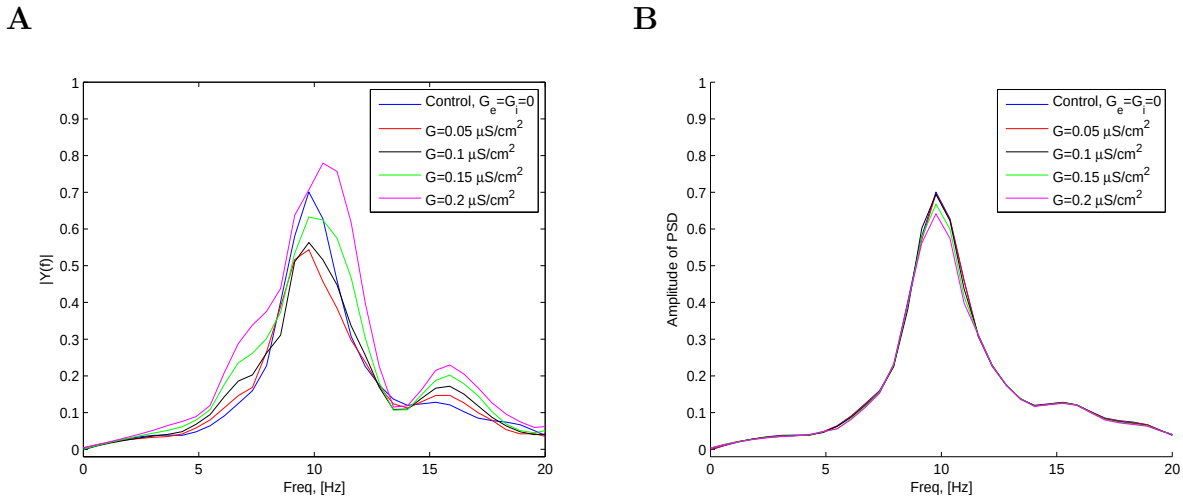

Figure 4.9 PSD in 3D SC model changed by changing G_e and G_i. Here we used $G_e = G_i = 0$, 0.05, 0.1, 0.15, and 0.2 $\mu S/cm^2$. Left panel is the PSD under conductance-based synaptic input. Right panel shows the PSD under synaptic leak current.

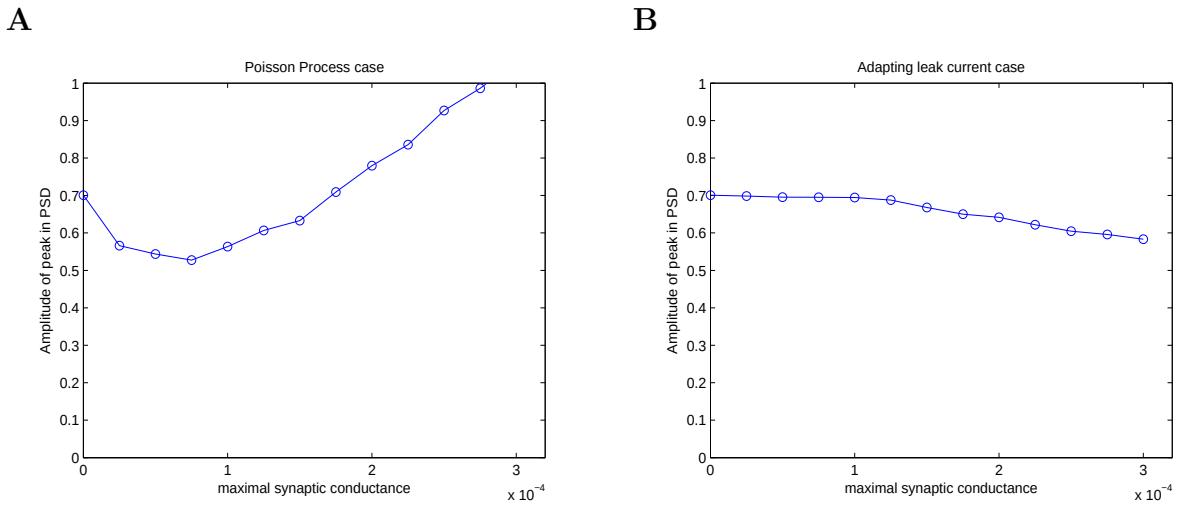

Figure 4.10 3D SC model. Systemically increasing the maximal synaptic conductance shows different effects in both conductance-based synaptic input and synaptic leak current. Figure 4.10A is the case of conductance-based synaptic input and figure 4.10B is the case of adapting leak current. For conductance-based synaptic input, the peak in PSD first decreased and then started increasing at the critical value of maximal synaptic conductance while the peak in PSD kept decreasing with increasing G_e and G_i for adapting leak current.

CHAPTER 5

CONCLUSIONS

5.1 The effects of periodic inputs on the dynamics of a medial entorhinal cortex layer II stellate cell model

Previous experimental works have shown the medial entorhinal cortex layer II stellate cells exhibit sub- and supra-threshold resonance in the theta frequency band [17, 16]. In modeling studies, the relationship between sub- and supra-threshold resonance has been studied by other authors [18, 19] using linear model. However, little attention has been addressed about the effect of both current- and conductance-based input on firing frequency preference in SCs. The results presented in this thesis contributes to understanding the biophysical mechanism: (1) under what condition subthreshold resonance properties are communicated with supra-threshold activity on SCs and this communication is disconnected. (2) How conductance-based inputs affect on SC's firing frequency preference. In this thesis, we found that subthreshold resonance properties are communicated with supra-threshold resonance on the presence of small amount of oscillatory input currents. These results are observed in SC's firing frequency preference under conductance-based synaptic inputs (both excitatory and inhibitory) with low amount of maximal synaptic conductance. However, when SC receives large amount of oscillatory current and conductance-based synaptic inputs, the communication between sub- and supra-threshold resonance properties is disconnected. In current-based oscillatory input, multiple peaks in firing rate are shown in supra-threshold resonance. Those peaks have relation in frequency such as the supra-threshold resonance frequency at the second peak is double of the first one and corresponding firing rate at both supra-threshold resonance frequencies are equivalent to each other. In excitatory

conductance-based input, SC model displays an additional peak (prominent peak) in gamma frequencies band. This results are in agreement with previous studies (SC with excitatory synaptic input displays hyper-excitability) [39]. In inhibitory conductance-based synaptic input, SC model display three preferred frequencies in supra-threshold resonance. These results are similar to the effect of oscillatory current-based input on SC's firing frequency preference. Furthermore, we found that the inhibition creates cell's spikes when the cell is silent. This is due to the phasic-inhibition.

Another contribution of this thesis is that the linearized model cannot capture the firing frequency preference at higher level of sinusoidal input current. Previous modeling studies [18, 19] have explained supra-threshold resonance using linearized models. The difficulties in linearized model in supra-threshold regime is to choose voltage threshold and neural reset mechanism. In our simulations, the linearized model displays bursting when SC receives large-amplitude of sinusoidal input current. This bursting is not observed in nonlinear model. This bursting is due to the shape of V-nullcline. And the intra-burst interspike intervals depend on both V_{th} and V_{reset}. This implies that the dynamic structure of supra-threshold activity is not unique. It can be altered by changing those values. In this thesis, we show that the linearized model is not appropriate to explain supra-threshold resonance properties in the SCs.

5.2 The effects of non-periodic inputs on the dynamics of a medial entorhinal cortex layer II stellate cell model

So far, we studied the effects of conductance- and current-based synaptic inputs on a medial entorhinal cortex layer II stellate cell's subthreshold activity. Our numerical results are in agreement with the experimental results [20] : conductance-based synaptic inputs not only reduce the amplitude-peak in PSD for corresponding subthreshold oscillations to these input but also alter subthreshold resonance properties

on the SC while current-based synaptic input retains its peak at the theta frequencies. A previous experimental study [20] has suggested that these inputs behave like a leak current. However, we found that conductance-based synaptic inputs do not always act as a leak current. These results differ from the previous study. We found maximal synaptic conductance ranges where the behavior of conductance-based synaptic inputs changes at a critical values. In this thesis, we would argue that the effect of conductance-based synaptic inputs (driven by Poisson process) is shown leaky behavior for small enough maximal synaptic conductance value (G_e and G_i) but for the higher value of G_e and G_i, those currents do not behave like a leak current. Furthermore, we studied the effect of maximal synaptic conductance on both conductance-based synaptic and adapting leak current ($I_{S,L}$). From the numerical simulations, we suggest that the fluctuations of presynaptic activity may play an important role in reducing or amplifying the amplitude of subthreshold oscillations. This suggestion can be supported by the effect of current-based synaptic inputs for large enough value of maximal synaptic conductance. Figure 5.1 shows the amplitude-peak in PSD for subthreshold oscillations as a function of maximal synaptic conductance under current-based synaptic inputs. In this simulation, we increased maximal synaptic conductance up to 5 $\mu S/cm^2$. The amplitude-peak in PSD as a function of maximal synaptic conductance behaves like a leak current in this regime.

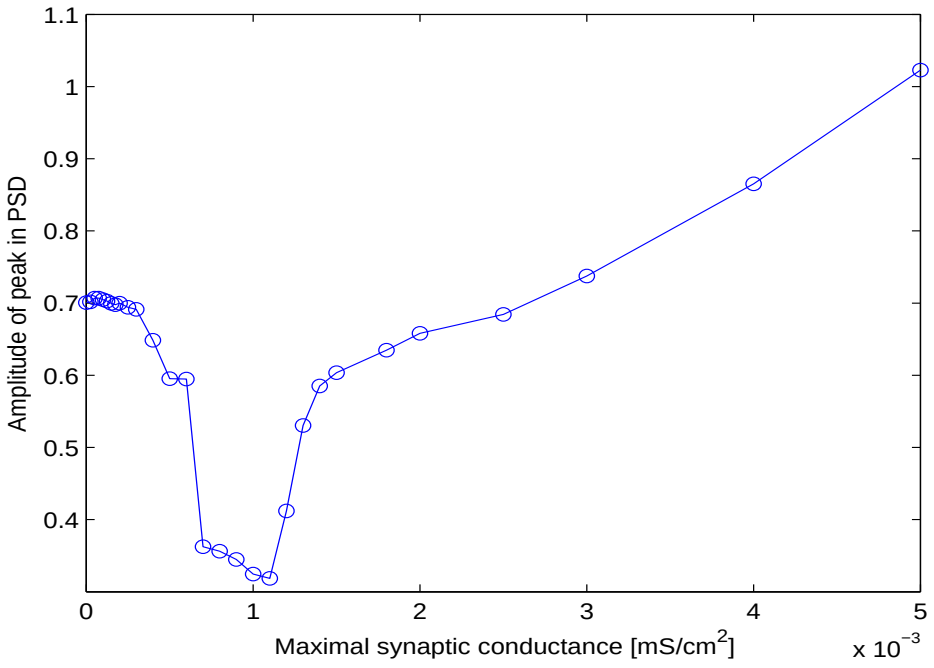

Figure 5.1 3D SC model. Systemically increasing the maximal synaptic conductance under current-based synaptic inputs shows the same non-monotonic behavior in amplitude-peak : the amplitude-peak in PSD first decreases and then starts increasing at $G_e = G_i$ =1.15 $\mu S/cm^2$.

APPENDIX A

THE DEFINITIONS OF THE FUNCTIONS DEFINING $X_\infty(V)$ AND $\tau_X(V)$

α_m(V) = -.01(V+23)/($e^{-0.1(V+23)}$-1)

β_m(V) = $4e^{-(V+48)/18}$

α_h(V) = $0.07e^{-(V+37)/20}$

β_h(V) = $1/(e^{-(0.1(V+7)}+1)$

α_n(v) = -0.01(v+27)/($e^{-0.1(V+27)}$-1)

β_n(V) = $0.125e^{-(V+37)/80}$

α_p(V) = $1/(9.15(1+e^{-(V+38)/6.5}))$

β_p(V) = $e^{-(V+38)/6.5}/(0.15(1+e^{-(V+38)/6.5}))$

$r_{f,\infty}(V) = 1/(1+e^{-(V+79.2)/9.78})$

τ_{r_f}(V) = $0.51/(e^{(V-1.7)/10}+e^{-(V+340)/52}+1)$

$r_{s,\infty}$(V) = $1/(1+e^{(V+2.83)/15.9})^{58}$

τ_{r_s}(V) = $5.6/(e^{(V-1.7)/14} + e^{-(V+260)/43}+1)$

τ_p(V) = 0.15

p_∞(V) = $1/(1+e^{-(V+38)/6.5})$

BIBLIOGRAPHY

[1] L. Katz and R. Cracco, "A review of the cerebral rhythms in the waking EEG.," *Am JEEG Technol*, vol. 11, pp. 77–100, 1971.

[2] G. Buzsaki, "Theta oscillations in the hippocampus.," *Neuron*, vol. 33, pp. 325–340, 2002.

[3] G. Buzsaki, "Theta rhythm of navigation; link between path integration and landmark navigation, episodic and semantic memory.," *Hippocampus*, 2005.

[4] G. Buzsaki, *Rhythms of the brain.* Oxford University Press, New York, 2006.

[5] C. Vanderwolf, "Hippocampal electrical activity and voluntary movement in the rat.," *EEG Clin Neurophysiol*, vol. 26, pp. 407–418, 1969.

[6] A. Alonso and E. Garica-Austt, "Neuronal sources of theta rhythm in the entorhinal cortex of the rat. II. phase relations between unit discharges and theta field potentials.," *Exp. Brain Res*, vol. 67, pp. 502–509, 1987.

[7] C. Dickson, J. Magistretti, M. Shalinsky, E. Fransen, and M. Hasselmo, "Properties and role of I_h in the pacing of subthreshold oscillation in entorhinal cortex layer II neurons.," *J. Neurophysiol*, vol. 83, pp. 2562–2579, 2000.

[8] S. Cajal, "Sobre un ganglio especial de la corteza esfeno-occipital.," *Trab. Lab. Invest. Biol. Univ. Madrid*, vol. 1, pp. 189–201, 1902.

[9] D. A. R. Insausti and W. Cowan, "The entorhinal cortex of the monkey. II. corical afferents.," *J. Comp. Neurol.*, vol. 264, pp. 356–395, 1902.

[10] W. Adey and S. Sunderland, "The entorhinal area: electrophysiological studies of its interrelations with rhinencephalic structrues and the brainstem.," *Clin. Neurophysiol*, vol. 9, pp. 309–324, 1957.

[11] H. Rotstein, T. Oppermann, J. White, and N. Kopell, "The dynamic strucutre underlying subthreshold oscillatory activity and the onset of spikes in a model of medial entorhinal cortex stellate cells.," *Journal of Computational Neuroscience*, vol. 21, pp. 271–292, 2006.

[12] A. Alonso and R. Linas., "Subthreshold Na^+-dependent theta-like rhythmicity in stellte cells of entorhinal cortex layer II.," *Nature*, vol. 342, pp. 175–177, 1989.

[13] A. Damasio, "Synchronous activation in multiple cortical regions: a mechanism for recall.," *Semin. Neurosci.*, vol. 2, pp. 287–296, 1990.

[14] A. Alonso and R. Klink., "Differential electroresponsiveness of stellate and pyramidal-like cells of medial entorhinal cortex layer II.," *J. Neurophysiol*, vol. 70, pp. 128–143, 1993.

[15] C. Acker, N. Kopell, and J.A.White, "Synchronization of strongly coupled excitatory neurons: relating network behavior to biophysics.," *Journal of Computational Neuroscience*, vol. 15, pp. 71–90, 2003.

[16] I. Erchova, S.Schreiber, U.Heinemann, and A.V.Herz, "Subthreshold resonance explains the frequency-dependent integration of periodic as well as random stimuli in the entorhinal cortex.," *J. Neurophysiol*, vol. 92, pp. 408–415, 2004.

[17] J. Haas and J. White, "Frequency selectivity of layer II stellate cells in the medial entorhinal cortex.," *J.Neurophyiol.*, vol. 88, pp. 2422–2429, 2002.

[18] M. Richardson, N. Brunel, and V. Hakim, "From subthreshold to firing-rate resonance.," *J. Neurophysiol.*, vol. 89, pp. 2538–2554, 2003.

[19] T. A. Engel, L. Schimansky-Geier, A. Herz, S. Schreiber, and I. Erchova, "Subthreshold membrane-potential resonances shape spike-train patterns in the entorhinal cortex.," *J. Neurosci*, vol. 100, pp. 1576–1589, 2008.

[20] F. Fernandez and J. White, "Artificial synaptic conductance reduce subthreshold oscillations and periodic firing in stellate cells of the entorhinal cortex.," *J. Neurosci.*, vol. 28(14), pp. 3790–3803, 2008.

[21] J. White, R. Klink, A. Alonso, and A. Kay, "Noise from voltage-gated ion channels may influence neuronal dynamics in the entorhinal cortex.," *J. Neurophysiol.*, vol. 80, pp. 262–269, 1998.

[22] E. Fransén, C. Dickson., J. M. J, and M. Hasselmo, "Ionic mechanisms in the generation of subthreshold oscillations and action potential clustering in entorhinal layer II stellate neurons.," *Hippocampus*, vol. 14, pp. 368–384, 2004.

[23] R. Fox, "Stochastic versions of the hodgkin-huxley equations.," *Biophys J.*, vol. 72, pp. 2068–2074, 1997.

[24] T. Kispersky and J. White, "Stochastic models of ion channel gating.," *Scholarpedia*, vol. 3(1):1317, 2008.

[25] E. Izhikevich, "Resonate-and-fire neurons.," *Neural Networks*, vol. 14, pp. 883–894, 2001.

[26] R. Llinas and Y. Yaron, "Oscillatory properties of guinea-pig inferior olivary neurons and their pharmacological modulation: an in vitro study.," *J. Neurophysiol*, vol. 376, pp. 163–182, 1986.

[27] R. Klink and A. Alonso, "Ionic mechanisms for the subthreshold oscillations and differential electroresponsiveness of medial entorhinal cortex layer II neurons.," *J. Neurophysiol*, vol. 77, pp. 1829–1843, 1986.

[28] B. Hutcheon and Y. Yarom, "Resonance oscillation and the intrinsic frequency preferences of neurons.," *Trends Neurosci*, vol. 23, pp. 216–222, 2000.

[29] B. Hutcheon, R. Miura, Y. Yarom, and E. Puil, "Low-threshold calcium current and resonance in thalamic neurons: a model of frequency preference.," *J. Neurophysiol*, vol. 71, pp. 583–594, 1994.

[30] I. Lampl and Y. Yarom, "Subthreshold oscillations and resonant behavior: Two manifestations of the same mechanism.," *Neuroscience*, vol. 78, pp. 325–341, 1997.

[31] E. Puil, B. Gimbarzevsky, and R. Miura, "Quantification of membrane properties of trigeminal root ganglions in guinea pigs.," *J. Neurophysiol*, vol. 55, pp. 995–1016, 1986.

[32] L. Leung and H. Yu, "Theta-frequency resonance in hippocampal CA1 neurons in vitro demonstrated by sinusoidal current injection.," *J. Neurophysiol*, vol. 79, pp. 1592–1596, 1998.

[33] V. Tohidi and F. Nadim, "Membrane resonance in bursting pacemaker neurons of an oscillatory network is correlated with network frequency.," *J. Neurosci*, vol. 29, pp. 6427–6435, 2009.

[34] B. Gimbarzevsky, R. Miura, and E. Puil, "Impedance profiles of peripheral and central neurons.," *Can J. Physiol Pharmacol*, vol. 62, pp. 460–462, 1984.

[35] S. Schreiber, I. Erchova, U. Heinemann, and A. Herz, "Subthreshold resonance explains the frequency-dependent integration of periodic as well as random stimuli in the entorhinal cortex.," *J. Neurophysiol*, vol. 92, pp. 408–415, 2004.

[36] N. Brunel, V. Hakim, and M. Richarson, "Firing-rate resonance in a generalized integrated-and-fire neuron with subthreshold resonance," *Phys. Rev.*, vol. 67: 051916, 2003.

[37] G. Falk and P. Fatt, "Linear electrical properties of striated muscle fibers observed with intracellular electrode.," *Proc Roc Lond B Biol Sci*, vol. 160, pp. 69–123, 1964.

[38] W. Gerstner, "Population dynamics of spiking neurons: fast transients, asynchronous states, and locking.," *Neural Comput*, vol. 12, pp. 43–49, 2000.

[39] T. Kispersky, J. A. White, and H. G. Rotstein, "The mechanism of abrupt transition between theta and hyper-excitable spiking activity in medial entorhinal cortex layer II stellate cells.," *PLoS One*, vol. 5:e13697, 2010.

[40] T. Verechtchaguina, I. Sokolov, and L. Schimansky-Geier, "First passage time densities in resonate-and-fire models.," *Phys Rev*, vol. 73: 031108, 2006.

[41] C. Koch, *Biophysics of Computation : information processing in single neurons.* Oxford University Press, New York, 1999.

[42] P. Dayand and L. Abbott, *Theoretical Neuroscience : computational and mathematical modeling of neural systems.* The MIT Press, Cambridge, MA, 2001.

[43] M. Maltenfort, C. Phillips, M. McCurdy, and T. Hamm, "Determination of the location and magnitude of synaptic conductance changes in spinal motoneurons by impedance measurements.," *J. Neurophysiol*, vol. 92, pp. 1400–1416, 2004.